ϕ photoproduction on the proton at $E_\gamma = 1.5 - 2.9$ GeV

Keigo Mizutani

A dissertation submitted in partial fulfillment of
the requirements for the degree of Doctor of Science
Department of Physics, Kyoto University

January, 2018

Abstract

The ϕ photoproduction is a unique tool to study the multigluon-exchange process, or Pomeron exchange process in terms of Regge theory, near the threshold. We have been investigating the reaction mechanism of the photoproduction of ϕ meson at very forward angles with LEPS spectrometer at SPring-8. In the previous 2005 LEPS measurement of the $\gamma p \to \phi p$ reaction where the energy range was from the threshold up to $E_\gamma = 2.37$ GeV, a nonmonotonic structure of the energy dependence of $(d\sigma/dt)_{t=t_{\rm min}}$ was observed at around $E_\gamma = 2.1$ GeV, which cannot be explained by the simple t-channel Pomeron$+\pi^0+\eta$ model. The origin of this nonmonotonic structure remains an open question until now. To study the nonmonotonic structure, we have extended the energy range up to $E_\gamma = 2.9$ GeV and measured the $\gamma p \to \phi p$ reaction using a linearly polarized photon beam in 2007 and 2015. The K^+K^- pair from the ϕ-meson decay was detected by the LEPS spectrometer to identify the $\gamma p \to \phi p$ reaction, and the differential cross section was extracted. Also, we have measured the spin-density matrix elements above $E_\gamma = 2.37$ GeV for the first time, and confirmed that the Pomeron-exchange process is dominant ($\sim 80\%$) at these energies. The cross sections were used to determine the Pomeron strength factor. The cross sections and spin-density matrix elements are consistently described by the t-channel Pomeron and pseudoscalar exchange model in the E_γ region above 2.37 GeV. In the lower energy region, an excess over the model prediction is observed in the energy dependence of the differential cross sections at $t = t_{\rm min}$. This observation suggests that additional processes or interference effects between Pomeron exchange and other processes appear near the threshold region.

CHAPTER

ONE

INTRODUCTION

A main physics motivation of this work is to investigate the nonmonotonic structure of forward cross sections for the $\gamma p \to \phi p$ reaction around $E_\gamma = 2.1$ GeV observed in the previous measurements of the LEPS and CLAS Collaborations. In this chapter, we describe the importance of the ϕ photoproduction as a tool to study multigluon-exchange processes and review previous measurements.

1.1 Multigluon-Exchange Process and Photoproduction of ϕ-meson

Photoproduction of the ϕ meson is a unique tool to access to multigluon-exchange processes (or a Pomeron-exchange process in terms of the Regge theory) at low energies. Figure 1.1 shows a multigluon-exchange process (a Pomeron-exchange process) of the ϕ photoproduction on the proton.

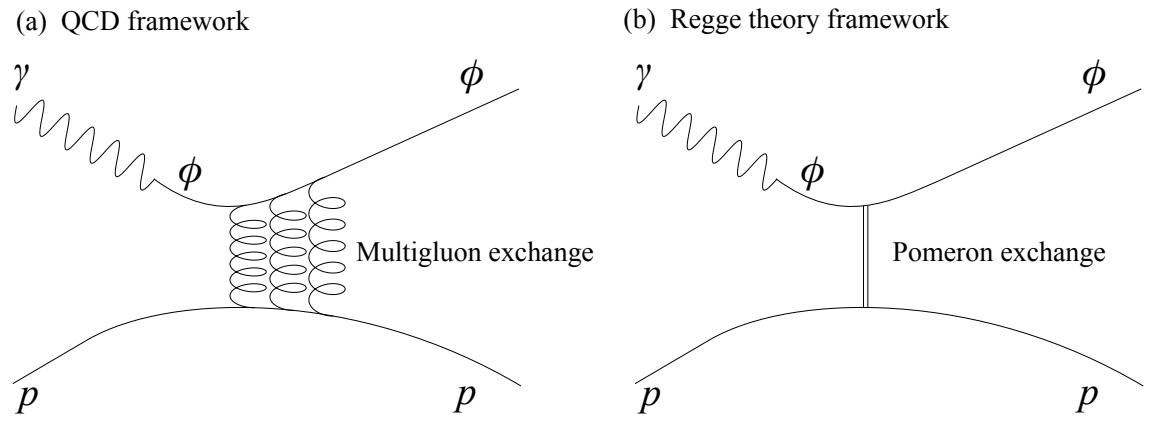

Fig. 1.1: Diagrams for photoproduction of the ϕ meson. (a) A multigluon-exchange process in the framework of QCD. (b) A Pomeron-exchange process in the framework of Regge theory.

Here, the photon and vector mesons ($\rho^0, \omega, \phi, J/\psi, ..$) share the same quantum numbers $J^{PC} = 1^{--}$, therefore the photon can convert into a vector meson (ϕ) for a short time. In other words, the photon behaves as a vector meson near hadrons [1]. This model is called the

vector meson dominance (VMD) model [2]. In this model, the amplitude of the vector meson photoproduction $\mathcal{A}_{\gamma p \to Vp}$ is related to the hadron-hadron scattering amplitude $\mathcal{A}_{V'p \to Vp}$ as follows [3]:

$$\mathcal{A}_{\gamma p \to Vp} = \sum_{V'_T} \frac{e}{\gamma_{V'}} \mathcal{A}_{V'p \to Vp}, \tag{1.1}$$

where e represents the electric charge and $\gamma_{V'}$ is the γ-V' coupling constant. V'_T indicates that the summation is only over the transversely polarized vector mesons, because a real massless photon has no longitudinal polarization.

Although the multigluon-exchange processes are universal for all the hadronic reactions due to the flavor-blindness of the gluon interactions, they are usually hidden in low-energy hadronic reactions by the large contribution from quark exchanges. This makes the study of the low-energy multigluon-exchange processes or Pomeron-exchange process difficult. The ϕ photoproduction from the proton (or the nucleus) is characteristic in that the quark exchanges are highly suppressed because the ϕ meson is almost purely an $s\bar{s}$ state and the target particle does not contain net strange quarks [Okubo-Zweig-Iizuka (OZI) rule [4, 5]].

Figure 1.2 shows energy dependences of total cross sections for the photoproductions of vector mesons (ρ, ω, ϕ, J/ψ). In the framework of the Regge theory, the slowly rising energy dependences above $\sqrt{s} = 10$ GeV are well explained by introducing a t-channel exchanged Pomeron trajectory [6, 7, 3, 8]. We dedicate the following subsection to a short review of the Regge theory and the Pomeron. In the framework of quantum chromodynamics (QCD), multigluon-exchange processes are a likely candidate of the Pomeron exchange process. At low energies $\sqrt{s} \sim 2$ GeV, the excess due to contributions of the quark exchanges are seen in the ρ^0 and ω photoproductions (Fig. 1.2), while for ϕ ($\sim s\bar{s}$) and J/ψ ($\sim c\bar{c}$) photoproductions, the data do not show clear contributions of the quark exchanges at low energies.

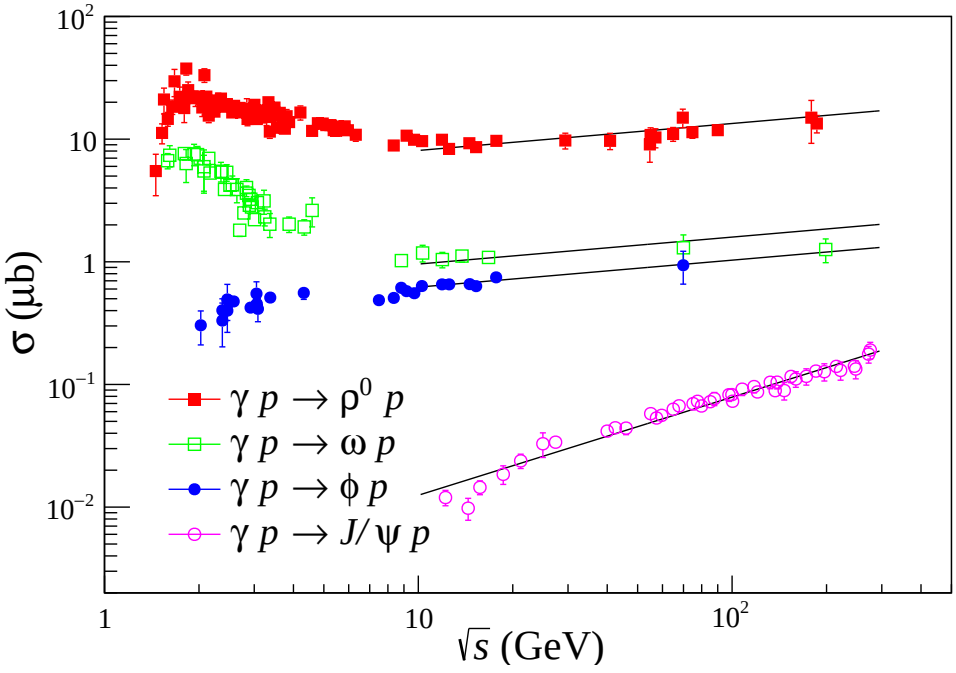

Fig. 1.2: Total production cross sections of vector mesons, together with fits of the form $\sqrt{s}^{\delta}$, where the logarithmic derivative δ is the fitting parameter [9].

1.1.1 Nonmonotonic structure of forward cross sections

The Pomeron-exchange amplitude increases monotonically with the energy [6, 7, 3, 8] (see also section 1.1.2). Therefore, the cross sections for the $\gamma p \to \phi p$ reaction at zero degrees $(d\sigma/dt)_{t=t_{\rm min}}$ [see also Eq. (1.20)] are predicted to increase monotonically with incident photon energy due to the dominance of the Pomeron-exchange process. However, a nonmonotonic structure at around $\sqrt{s} = 2.1$ GeV was first observed in 2005 by the LEPS Collaboration [10] as shown in Fig 1.3, which cannot be explained by simple t-channel π^0, η and Pomeron exchanges.

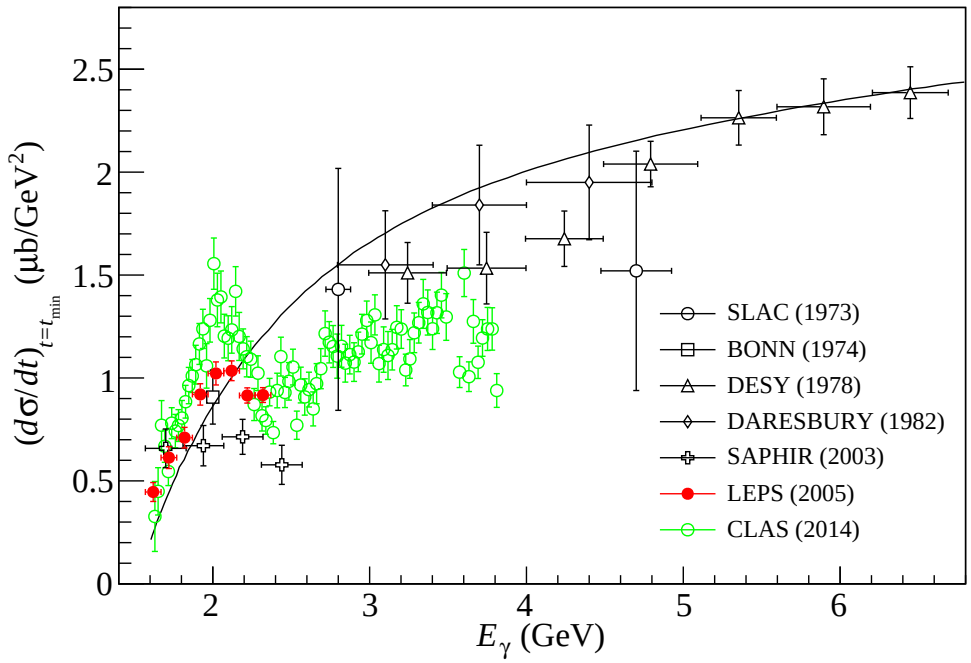

Fig. 1.3: Energy dependence of $(d\sigma/dt)_{t=t_{\rm min}}$. Data points are taken from Refs. [10, 11, 12, 13, 14, 15, 16, 17]. The solid curve represents the prediction of a model including the Pomeron, π^0 and η exchange processes [18].

The CLAS Collaboration also confirmed this nonmonotonic structure by the extrapolation of their measurements at larger angles [17, 19]. The origin of this nonmonotonic structure is still an open question. The possible explanations are summarized in the section 1.4 of this chapter.

Note that in this thesis, we use "low energy" to indicate below $E_\gamma = 2.4$ GeV if the energy is not explicitly specified, where the nonmonotonic structure exists as shown in Fig. 1.3. On the other hand, "high energy" indicates the energy region above $E_\gamma = 2.4$ GeV.

1.1.2 Regge theory and the Pomeron

In this subsection, we give a short review of the Regge theory and the Pomeron, which are developed in 1960s before the QCD was established. Originally, the Regge theory is developed to explain the non-perturbative region of the hadron scattering, using hadronic degrees of freedom. It is based on relativistic S-matrix theory, and the starting point is not the Lagrangians

or Hamiltonians. Note that the key idea of the theory is treating the angular momentum as a complex variable as described below.

Postulates of S-matrix theory

The abth element of S-matrix is the overlap between the in-state $|a\rangle$, and the out-state $|b\rangle$ (free particle states as $t \to -\infty$ and $t \to +\infty$, respectively), as follows:

$$S_{ab} = \langle b_{\text{out}} | a_{\text{in}} \rangle \, . \tag{1.2}$$

We give a set of postulates of S-matrix [20].

Postulate 1 The S-matrix is Lorentz invariant.

Postulate 2 The S-matrix is unitary: $SS^\dagger = S^\dagger S = \mathbb{1}$.

Postulate 3 The S-matrix is a holomorphic function of Lorentz invariants (regarded as complex variables), with singularities dictated by unitarity.

Here, we consider only two-particle to two-particle scattering $1 + 2 \to 3 + 4$. From the first postulate, the S-matrix can be expressed as a function of the Mandelstam variables s and t, i.e., $S = S(s, t)$. The definitions of the Mandelstam variables s, t, and u are as follows [21]:

$$s = (p_1 + p_2)^2, \tag{1.3}$$
$$t = (p_1 - p_3)^2, \tag{1.4}$$
$$u = (p_1 - p_4)^2, \tag{1.5}$$

where p_1 and p_2 are the 4-momenta of the incoming particles and p_3 and p_4 are the 4-momenta of the outgoing particles. Note that for two-particle to n particle scattering processes, there are $3n - 4$ independent invariants.

The second postulate comes from the conservation of probability, and leads to the Cutkosky rule (and optical theorem) described below. The scattering amplitude $\mathcal{A}$ is defined as follows:

$$S_{ab} = \delta_{ab} + i(2\pi)^4 \delta^4 \left(\sum_a p_a - \sum_b p_b \right) \mathcal{A}_{ab}, \tag{1.6}$$

where p denotes the 4-momentum. By using $S_{ab} = S_{ba}$, which comes from the parity and time reversal conservation, the unitarity condition of the S-matrix is converted as follows:

$$2\text{Im}\mathcal{A}_{ab} = (2\pi)^4 \delta^4 \left(\sum_a p_a - \sum_b p_b \right) \sum_c \mathcal{A}_{ac} \mathcal{A}^\dagger_{cb}. \tag{1.7}$$

This is called Cutkosky rule [22, 23], and a generalization of the optical theorem which relates the imaginary part of the forward elastic scattering amplitude $\mathcal{A}_{aa}$ to the total cross section ($\sigma_{\text{tot}} \propto \text{Im}\mathcal{A}_{aa}$)[1]. Eq. (1.7) allows us to get the imaginary part of an amplitude by considering the amplitudes of the incoming and outgoing states into all possible intermediate states. This rule will be used in later chapters.

The third postulate determines the singularity structure of the S-matrix. Only simple poles and branch cuts are the allowed singularities, and physical information is contained in these poles and cuts. Also, causality is related to this analyticity, and the satisfaction of the dispersion relation [24] is ensured by the third postulate.

[1] This is a special case of $a = b$ in the Cutkosky rule Eq. (1.7).

Sommerfeld-Watson transform

The scattering amplitude can be expanded in a series as follows:

$$\mathcal{A}(s,t) = \sum_{\ell=0}^{\infty}(2\ell+1)a_\ell(t)P_\ell(1+2s/t). \tag{1.8}$$

Note that this expansion is obtained by interchanging s and t after the standard partial wave expansion of the t-channel amplitude [3, 20]. This t-channel partial-wave series representation is motivated by the dominance of the t-channel diagrams in the hadron scatterings at high energies (and small $|t|$). Sommerfeld and Watson rewrote this formula in terms of a contour integral in the complex angular momentum ℓ-plane as follows [25, 26]:

$$\mathcal{A}(s,t) = -\frac{1}{2\pi i}\oint_C (2\ell+1)a(\ell,t)P(\ell,-1-2s/t)\frac{\pi}{\sin\pi\ell}d\ell, \tag{1.9}$$

where the contour C surrounds nonnegative integers as shown in Fig. 1.4. The function $P(\ell,z)$ is a generalized Legendre polynomials (hypergeometric function), and has a complex argument ℓ. $P(\ell,z) = P_\ell(z)$ holds for each nonnegative integer ℓ. Also, $a(\ell,t)$ is an extension of $a_\ell(t)$, and an analytic function of the complex argument ℓ. Eq. (1.8) can be reproduced, using the following two properties: (a) $\frac{\pi}{\sin\pi\ell}$ is a meromorphic function having simple poles at $\ell = n$, $n \in \mathbb{Z}$ with residue $(-1)^n$, and there are no other singularities in the complex plane, and (b) $P(\ell,-z) = (-1)^\ell P(\ell,z)$ holds for each nonnegative integer ℓ. The overall sign is determined by the orientation of the contour C.

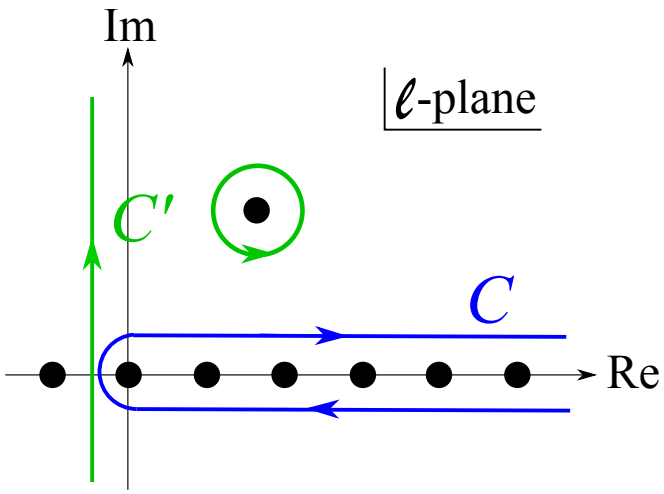

Fig. 1.4: The integration contour for the Sommerfeld-Watson transform of the scattering amplitude. The black dots on the real axis represent integers, which are the simple poles of the function $\frac{\pi}{\sin\pi\ell}$. The other black dot (Re$\ell > 0$, Im$\ell > 0$) represents a simple pole of $a(\ell,t)$. The blue contour C surrounds the nonnegative integers $0, 1, 2, \cdots$. The green one C' is the deformed integration contour. See text for details.

Regge poles

Next, we deform the contour C into C', which runs parallel to the imaginary axis with Re $\ell = -1/2$, as shown in Fig. 1.4. In deforming the contour, we must encircle any poles or branch

cuts of the function $a(\ell, t)$. In Fig. 1.4, we show the deformed contour in the case of $a(\ell, t)$ having one simple pole. Let the Laurent series of the function $a(\ell, t)$ about the simple pole be

$$a(\ell, t) = \frac{\beta(t)}{\ell - \alpha(t)} + f(\ell, t), \tag{1.10}$$

where $f(\ell, t)$ is an entire function about ℓ, i.e., the residue of $a(\ell, t)$ at $\ell = \alpha(t)$ is $\beta(t)$. Then, we arrive at

$$\mathcal{A}(s,t) = -\frac{\pi(2\alpha(t)+1)\beta(t)}{\sin\pi\alpha(t)} P(\alpha(t), -1-2s/t) - \frac{1}{2i}\int_{-\frac{1}{2}-i\infty}^{-\frac{1}{2}+i\infty} \frac{2\ell+1}{\sin\pi\ell} a(\ell,t) P(\ell, -1-2s/t) d\ell. \tag{1.11}$$

In the Regge limit where $s \gg |t|$,

$$P(\ell, -1-2s/t) \longrightarrow \frac{\Gamma(2\ell+1)}{\Gamma^2(\ell+1)} \left(-\frac{s}{2t}\right)^\ell \tag{1.12}$$

holds, where Γ is the Euler gamma function. Therefore, the second term on the right hand side of Eq. (1.11) can be neglected as $s \to \infty$. Finally, the amplitude (first term) can be written as:

$$\mathcal{A}(s,t) = \tilde{\beta}(t) s^{\alpha(t)}, \tag{1.13}$$

where some factors depending on t (but not on s) have been absorbed into the function $\tilde{\beta}$.

Regge trajectories

If we consider that the physical particle of spin J and mass M is exchanged in the t-channel, we can expect the following relation:

$$\alpha(t = M^2) = J. \tag{1.14}$$

Chew and Frautschi noticed that the spins of light mesons are linearly related to the square masses [27, 28], as shown in Fig. 1.5.

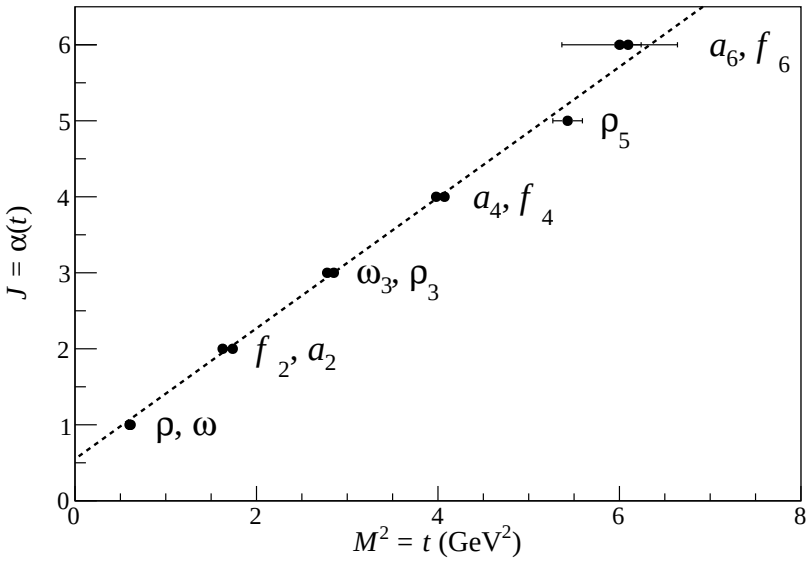

Fig. 1.5: The Chew-Frautschi plot.

In other words $\alpha(t)$ is a linear function, and from Fig. 1.5, the intercept and slope of $\alpha(t)$ are obtained as follows:

$$\alpha(0) = 0.55 \tag{1.15}$$
$$\alpha' = 0.86\ \text{GeV}^{-2}, \tag{1.16}$$

where $\alpha(t) = \alpha(0) + \alpha' t$. This is called a mesonic "Regge trajectory". It is known that baryons also furnish Regge trajectories.

Pomeron

If t-channel exchange of the Regge trajectory $\alpha(t)$ is dominant, the total cross section behaves as follows:

$$\sigma_{\text{tot}} \propto s^{\alpha(0)-1}, \tag{1.17}$$

which is derived from Eq. (1.13) and the optical theorem. Because the mesonic and baryonic Regge trajectories satisfy $\alpha(0) < 1$ [Eq. (1.15)], it is expected that the cross section vanishes asymptotically at large $\sqrt{s}$. However, as shown in Fig 1.6, the observed total cross sections rise slowly as $\sqrt{s}$ increases. If we attribute the slow rise to the t-channel exchange of a single Regge trajectory, its intercept $\alpha(0)$ is greater than 1. This trajectory is called the Pomeron, named after its inventor Pomeranchuk. Foldy and Peierls has pointed out that if the cross section does not fall as $\sqrt{s}$ increases, its reaction processes should be dominated by the t-channel exchange of vacuum quantum numbers [29]. Therefore, the Pomeron is considered to carry the quantum numbers of the vacuum.

Using the Pomeron contribution, Donnachie and Landshoff (1992) extracted the following expression of the total cross sections for the proton-antiproton and proton-proton scatterings [30]:

$$\sigma_{\bar{p}p} = 21.7 s^{0.08} + 98.4 s^{-0.45}\ \text{mb} \tag{1.18}$$
$$\sigma_{pp} = 21.7 s^{0.08} + 56.1 s^{-0.45}\ \text{mb} \tag{1.19}$$

with s in GeV^2 by the fit as shown in the top left of Fig. 1.6. Fitting region was $\sqrt{s} < 100$ GeV. Note that the data points of $\sqrt{s} > 100$ GeV were obtained using the Fermilab Tevatron accelerator after Donnachie and Landshoff had got Eqs. (1.18,1.19). The first terms on the right hand sides of Eqs. (1.18,1.19) $21.7 s^{0.08}$ are the Pomeron contribution, which are dominant at high energies. They are the same because the Pomeron carries the vacuum quantum numbers, and cannot distinguish between particles and antiparticles. The second terms are due to the Regge trajectory shown in Fig. 1.5, which are, on the other hand, important at low energies. Because the intercept $\alpha(0)$ of the mesonic Regge trajectory is $\alpha(0) = 0.55$ [see Eq. (1.15)], the exponent $\alpha(0) - 1 = -0.45$ is obtained [Eq. (1.17)]. The fit tells us that the Pomeron has an intercept $\alpha(0) = 1 + 0.08 = 1.08$.

Other hadron scatterings show the same behavior $\sigma = X s^{0.08} + Y s^{-0.45}$ as shown in Fig. 1.6, which indicates that the Pomeron contribution is universal. The coefficients X and Y are determined by the fit. Note that the coefficient X is common to ab and $\bar{a}b$ scatterings for the same reason as the proton-antiproton and proton-proton scatterings.

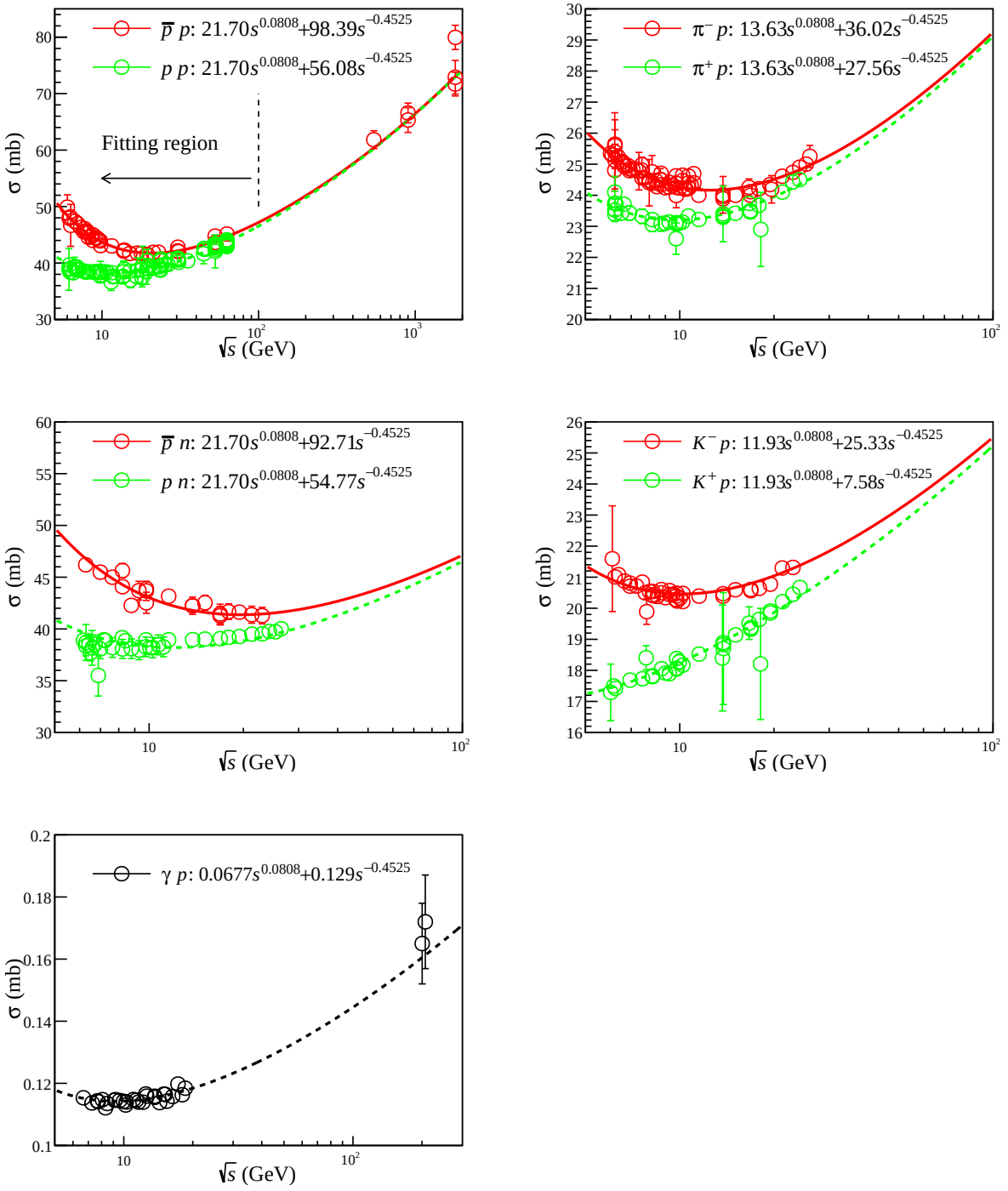

Fig. 1.6: Total cross sections.

The top right of Fig. 1.6 shows the results for $\pi^{\pm}p$. The coefficients of the Pomeron term X in the fits to $p(\bar{p})$-p and π-p scatterings are in the ratio $1.59 : 1 \simeq 3 : 2$. This ratio can be understood by the quark-counting rule [31]. The proton has three valence quarks whereas the pion has two. Here, the Pomeron is assumed to behave like a point particle, which is inferred from the t-dependence of p-p (or $\bar{p}$-p) differential elastic cross sections [20].

The bottom of Fig. 1.6 shows the results for γp. The $Xs^{0.08} + Ys^{-0.45}$ shape describes the data well, though the error bars of the data points at high energies are large. This supports the vector-meson dominance assumption.

The slope of the Pomeron trajectory has been determined to be $\alpha' = 0.25$ GeV^{-2}, by the p-p (or $\bar{p}$-p) differential cross section measurements of ISR at CERN and Tevatron at Fermilab. The ρ-parameter ($\rho = \mathrm{Re}\mathcal{A}/\mathrm{Im}\mathcal{A}$) can also be obtained from the differential elastic cross section at zero degrees and the total cross section. UA4/2 Collaboration at CERN gives $\rho \simeq 0.1$ at $\sqrt{s} \sim 100$ GeV [32, 33]. In other words, the Pomeron exchange amplitude is predominantly imaginary, at least at around this high energy region.

So far, the physical particles on the Pomeron trajectory have not been conclusively identified. As already indicated in this section, they have the quantum numbers of the vacuum, and that makes the detection difficult. However, the glueballs or bound states of gluons, whose existences are predicted by QCD, are expected to lie on the Pomeron trajectory. Another controversy exists about until how low energy the Pomeron picture can be applied. Also, it is important to pin down the Pomeron behaviors at low energies, since it is universal for all the hadronic scatterings.

1.2 What's to be measured?

Here, we introduce physical quantities which characterize the ϕ-meson photoproduction.

1.2.1 Diffractive exchange parameters B and $(d\sigma/dt)_{t=t_{\mathrm{min}}}$

Differential cross section $d\sigma/dt$ is a fundamental quantity, which depends on the beam energy E_γ[2] and the production angle of the ϕ meson. We use Mandelstam variable t to express the production angle, instead of the polar angle $\cos\theta_{\mathrm{c.m.}}$ or $\cos\theta_{\mathrm{lab}}$. Phenomenologically, ϕ-meson production cross sections at forward angles are characterized by the following diffractive exchange parameters B and $(d\sigma/dt)_{t=t_{\mathrm{min}}}$:

$$\frac{d\sigma}{dt} = \left(\frac{d\sigma}{dt}\right)_{t=t_{\mathrm{min}}} \exp[B(t - t_{\mathrm{min}})], \tag{1.20}$$

where t_{min} denotes t at zero degrees[3]. This forward peaking structure reflects that t-channel exchange processes are dominant. Here, the diffractive exchange parameters B and $(d\sigma/dt)_{t=t_{\mathrm{min}}}$ are the functions of E_γ, which give important information about the ϕ photoproduction. The t-slope factor B is related to the hadron size, and $(d\sigma/dt)_{t=t_{\mathrm{min}}}$ is the cross section at zero degrees. Figures 1.7 show the kinematic relationship of t and $\cos\theta_{\mathrm{lab}}$ and the E_γ dependence of t_{min}.

[2] In this thesis, E_γ denotes the photon beam energy in the laboratory system.

[3] t is negative, and t_{min} is the maximum value of t at the fixed E_γ. The subscript "min" represents the minimum momentum transfer.

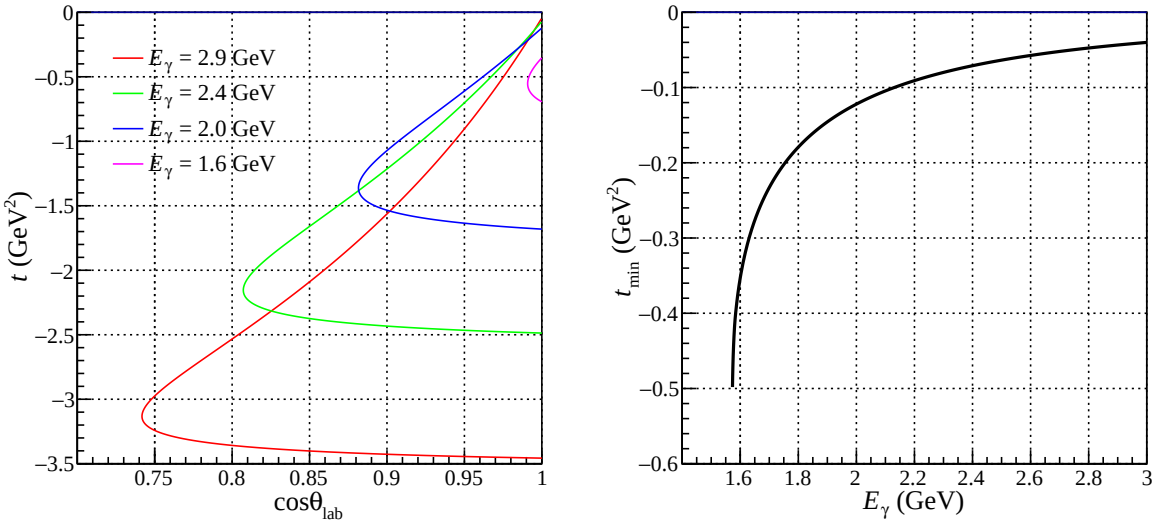

Fig. 1.7: t vs $\cos\theta_{\rm lab}$ (left) and $t_{\rm min}$ vs E_γ (right) for the ϕ-meson photoproduction on the proton.

The LEPS spectrometer measures ϕ mesons at forward angles ($\cos\theta_{\rm lab} > 0.95$), as will be described in the next chapter 2.

1.2.2 Spin observables

Besides the cross section, spin observables give important information to pin down the production mechanism of the ϕ meson. Experimentally, it is difficult to directly measure the spin orientation of the ϕ meson event by event. However, the spin information is inherited by decay products, and we can obtain the spin information, or spin-density matrix of the produced ϕ meson, by measuring its decay angular distributions.

Gottfried-Jackson, helicity and Adair frames

To define angles of the decay products, a coordinate system should be prepared. Essentially, this is equivalent to specify the spin-quantization z-axis of the ϕ meson. Here, we introduce three commonly used choices, Gottfried-Jackson (GJ) frame, helicity frame and Adair frame (Fig. 1.8).

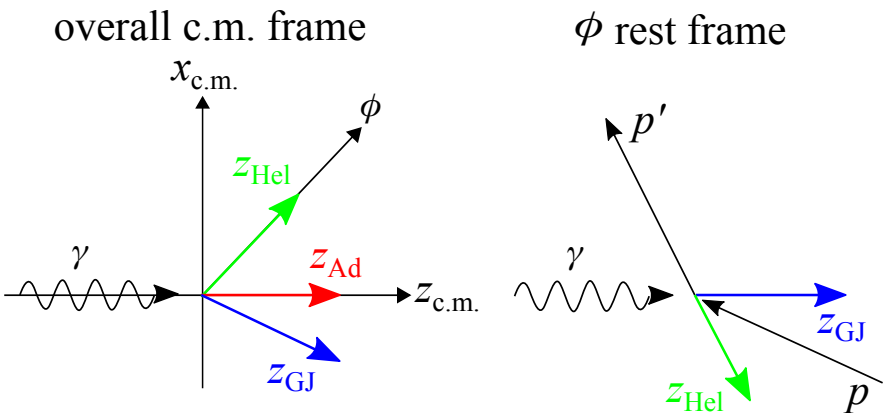

Fig. 1.8: Left: The spin-quantization axes for the helicity (Hel, in green), Adair (Ad, in red), and Gottfried-Jackson (GJ, in blue) frames, in relation to the overall c.m. frame. Right: The spin-quantization axes for the helicity (Hel, in green), and Gottfried-Jackson (GJ, in blue) frames, in relation to the ϕ-meson rest frame. p (p') represents the incident (outgoing) proton.

GJ frame z-axis is the direction of the incoming photon in the ϕ-meson rest frame.

Helicity frame z-axis is the direction of the ϕ meson in the overall c.m. frame. This is equivalent to the opposite direction of the outgoing proton in the ϕ-meson rest frame.

Adair frame z-axis is the direction of the incoming photon in the overall c.m. frame.

x- and y-axes are defined in the following manner. y-axis is defined as the direction of $\vec{p}_\gamma \times \vec{p}_\phi$, where $\vec{p}_\gamma$ and $\vec{p}_\phi$ are 3-momenta of the incident photon and outgoing ϕ meson, respectively. x-axis is defined to complete an orthogonal right-handed system. Note that the xz-plane is the production plane, and that when ϕ meson is scattered at zero degrees, the directions of the z-axes of these three frames are the same. In this thesis, we basically use the GJ frame if the frame is not explicitly specified.

Spin-density matrix and Decay angular distribution

The spin-density matrix is defined as follows:

$$\rho = \sum_i p_i \left|\psi^i\right\rangle \left\langle\psi^i\right|, \tag{1.21}$$

where $|\psi^i\rangle$ is a state vector in the spin Hilbert space, and p_i is a probability to find the state $|\psi^i\rangle$ in the mixed states. Since the ϕ meson has spin 1, the spin-density matrix of the ϕ meson can be represented by a 3×3 matrix.

In general, when the particle with spin s and spin-density matrix ρ decays to two particles a and b, the angular distribution of a has the form [34]:

$$W(\cos\theta, \varphi) = \frac{2s+1}{4\pi} \sum_{\lambda,\lambda',\lambda_a,\lambda_b} D^{s*}_{\lambda,\lambda_a-\lambda_b}(\varphi,\theta,0)\rho_{\lambda\lambda'} D^{s}_{\lambda',\lambda_a-\lambda_b}(\varphi,\theta,0), \tag{1.22}$$

where θ and φ denote the polar and azimuthal angles of a in the selected frame, respectively. λ and λ' denote the spin projections of the ϕ meson, and $\lambda_{a(b)}$ denotes the helicity of $a(b)$ (they

are all bound variables). The Wigner rotation function can be decomposed as follows [35]:

$$D^s_{m',m}(\alpha,\beta,\gamma) = \exp(-im'\alpha) d^s_{m',m}(\beta) \exp(-im\gamma). \tag{1.23}$$

In the case of $\phi \to K^+K^-$ ($a = K^+$), we obtain:

$$W(\cos\theta,\varphi) = \frac{3}{4\pi}\left(\frac{\rho_{11}+\rho_{-1-1}}{2}\sin^2\theta + \rho_{00}\cos^2\theta - \frac{\mathrm{Re}\rho_{10}-\mathrm{Re}\rho_{-10}}{\sqrt{2}}\sin 2\theta\cos\varphi \right.$$
$$\left. + \frac{\mathrm{Im}\rho_{10}+\mathrm{Im}\rho_{-10}}{\sqrt{2}}\sin 2\theta\sin\varphi - \mathrm{Re}\rho_{1-1}\sin^2\theta\cos 2\varphi + \mathrm{Im}\rho_{1-1}\sin^2\theta\sin 2\varphi\right), \tag{1.24}$$

using the hermiticity of the spin-density matrix [36, 37].

Using polarized photons (and unpolarized target), the spin-density matrix of the vector meson can be decomposed as follows [36]:

$$\rho(V) = \rho^0 + \sum_{\alpha=1}^{3} P^\alpha_\gamma \rho^\alpha, \tag{1.25}$$

where P^α_γ is the Stokes vector[4]. This decomposition comes from spin-density matrix of the incident photon $\rho(\gamma)$, written as a linear combination of the Pauli matrices. Because the decay angular distribution W in Eq. (1.22) is linear in ρ, it is decomposed as well:

$$W(\cos\theta,\varphi) = W^0(\cos\theta,\varphi) + \sum_{\alpha=1}^{3} P^\alpha_\gamma W^\alpha(\cos\theta,\varphi), \tag{1.26}$$

where W^α ($\alpha = 0,1,2,3$) is defined by Eq. (1.24) with ρ replaced by ρ^α. Using the symmetries of the ρ^α [36, 37]:

$$\rho^\alpha_{\lambda\lambda'} = (-1)^{\lambda-\lambda'}\rho^\alpha_{-\lambda-\lambda'} \quad (\alpha = 0,1), \tag{1.27}$$
$$\rho^\alpha_{\lambda\lambda'} = -(-1)^{\lambda-\lambda'}\rho^\alpha_{-\lambda-\lambda'} \quad (\alpha = 2,3), \tag{1.28}$$

which reflect the parity conservation, W^α are expressed as follows[5]:

$$W^0(\cos\theta,\varphi) = \frac{3}{4\pi}\left(\frac{1-\rho^0_{00}}{2} + \frac{3\rho^0_{00}-1}{2}\cos^2\theta - \sqrt{2}\mathrm{Re}\rho^0_{10}\sin 2\theta\cos\varphi - \mathrm{Re}\rho^0_{1-1}\sin^2\theta\cos 2\varphi\right), \tag{1.29}$$

$$W^1(\cos\theta,\varphi) = \frac{3}{4\pi}\left(\rho^1_{11}\sin^2\theta + \rho^1_{00}\cos^2\theta - \sqrt{2}\mathrm{Re}\rho^1_{10}\sin 2\theta\cos\varphi - \mathrm{Re}\rho^1_{1-1}\sin^2\theta\cos 2\varphi\right), \tag{1.30}$$

$$W^\alpha(\cos\theta,\varphi) = \frac{3}{4\pi}\left(\sqrt{2}\mathrm{Im}\rho^\alpha_{10}\sin 2\theta\sin\varphi + \mathrm{Im}\rho^\alpha_{1-1}\sin^2\theta\sin 2\varphi\right) \quad (\alpha = 2,3). \tag{1.31}$$

W^0 and W^1 differ because we use the normalization condition $\mathrm{tr}\rho^0 = 1$ whereas there is no trace condition for ρ^1. Hereafter, we will use the term "spin-density matrix element (SDME)" to represent $\rho^\alpha_{\lambda\lambda'}$ in Eqs. (1.29,1.30,1.31). Note that these SDMEs are the functions of the

[4]The Stokes vector specifies the photon polarization. See Ref. [36] for details.

[5]Since ρ^α_{1-1} ($\alpha = 0,1$) are real numbers, $\mathrm{Re}\rho^\alpha_{1-1}$ in Eqs. (1.29,1.30) are often written as ρ^α_{1-1} [36, 18]

energy (E_γ) and the ϕ-meson polar angle (Mandelstam t). When the incident photon is linearly polarized, the Stokes vector P_γ^α can be written as

$$(P_\gamma^\alpha) = P_\gamma(-\cos 2\Phi, -\sin 2\Phi, 0), \tag{1.32}$$

where P_γ is the degree of polarization of the photon beam, and Φ denotes the angle between the photon-polarization vector and ϕ-meson production plane. Note that W^3 in Eq. (1.26) has meaning when the incident photon is circularly polarized ($P_\gamma^3 \neq 0$). Comparing to W^1 and W^2, W^3 provides less information about exchanged particles in the t-channel.

Integrated one-dimensional angular distribution

With limited statistics, the following integrated one-dimensional angular distributions are useful to extract the SDMEs:

$$W(\cos\theta) = \frac{3}{2}\left(\frac{1-\rho^0_{00}}{2}\sin^2\theta + \rho^0_{00}\cos^2\theta\right), \tag{1.33}$$

$$W(\varphi) = \frac{1}{2\pi}\left(1 - 2\mathrm{Re}\rho^0_{1-1}\cos 2\varphi\right), \tag{1.34}$$

$$W(\varphi - \Phi) = \frac{1}{2\pi}\left(1 + 2P_\gamma\frac{\rho^1_{1-1} - \mathrm{Im}\rho^2_{1-1}}{2}\cos\left[2\left(\varphi - \Phi\right)\right]\right), \tag{1.35}$$

$$W(\varphi + \Phi) = \frac{1}{2\pi}\left(1 + 2P_\gamma\frac{\rho^1_{1-1} + \mathrm{Im}\rho^2_{1-1}}{2}\cos\left[2\left(\varphi + \Phi\right)\right]\right), \tag{1.36}$$

$$W(\Phi) = 1 - P_\gamma\left(2\rho^1_{11} + \rho^1_{00}\right)\cos 2\Phi. \tag{1.37}$$

The following symbols are also used:

$$\bar{\rho}^1_{1-1} = \frac{\rho^1_{1-1} - \mathrm{Im}\rho^2_{1-1}}{2}, \tag{1.38}$$

$$\Delta_{1-1} = \frac{\rho^1_{1-1} + \mathrm{Im}\rho^2_{1-1}}{2}. \tag{1.39}$$

Note that $2\rho^1_{11} + \rho^1_{00}$ in Eq. (1.37) is a beam asymmetry for the $\gamma p \to \phi p$ reaction, which is independent on the decay properties of the ϕ meson.

Observables expressed in terms of amplitudes

The amplitude, which corresponds to the wave function in quantum mechanics, has all the information about the reaction, and every observable can be expressed in terms of amplitudes. Here, we introduce how the observables are expressed in terms of amplitudes. There are several conventions to define the amplitude, and we use the invariant amplitude I defined in Ref. [18]. The invariant amplitude I is normalized such that the differential cross section is expressed as:

$$\frac{d\sigma}{dt} = \frac{1}{64\pi(s - m_p^2)^2}\sum_{m,\lambda_\gamma,\lambda_\phi}|I_{m;\lambda_\phi,\lambda_\gamma}|^2, \tag{1.40}$$

where m_p represents the proton mass. The symbol m includes the polarizations of the incoming and the outgoing protons. λ_γ represents the helicity of the incident photon. λ and λ' are the ϕ-meson spin projections. Note that I is dimensionless.

The spin-density matrix of the outgoing vector meson $\rho(V)$ and that of incoming photon $\rho(\gamma)$ are connected by the invariant amplitude I as follows [36]:

$$\rho(V) = \frac{2}{N} I \rho(\gamma) I^\dagger, \tag{1.41}$$

where the normalization factor N reads

$$N = \sum_{m,\lambda,\lambda_\gamma} I_{m;\lambda,\lambda_\gamma} I^\dagger_{m;\lambda,\lambda_\gamma}. \tag{1.42}$$

Here, the photon density matrix $\rho(\gamma)$ can be written as

$$\rho(\gamma) = \frac{1}{2} \left(\mathbb{1} + \boldsymbol{P}_\gamma \cdot \boldsymbol{\sigma} \right), \tag{1.43}$$

using the Stokes vector $\boldsymbol{P}_\gamma$ and the Pauli operator $\boldsymbol{\sigma}$. Therefore, the four Hermitian matrices ρ^α $(\alpha = 0, 1, 2, 3)$ read explicitly [18]:

$$\rho^0_{\lambda\lambda'} = \frac{1}{N} \sum_{m,\lambda_\gamma} I_{m;\lambda,\lambda_\gamma} I^\dagger_{m;\lambda',\lambda_\gamma}, \tag{1.44}$$

$$\rho^1_{\lambda\lambda'} = \frac{1}{N} \sum_{m,\lambda_\gamma} I_{m;\lambda,-\lambda_\gamma} I^\dagger_{m;\lambda',\lambda_\gamma}, \tag{1.45}$$

$$\rho^2_{\lambda\lambda'} = \frac{i}{N} \sum_{m,\lambda_\gamma} \lambda_\gamma I_{m;\lambda,-\lambda_\gamma} I^\dagger_{m;\lambda',\lambda_\gamma}, \tag{1.46}$$

$$\rho^3_{\lambda\lambda'} = \frac{1}{N} \sum_{m,\lambda_\gamma} \lambda_\gamma I_{m;\lambda,\lambda_\gamma} I^\dagger_{m;\lambda',\lambda_\gamma}. \tag{1.47}$$

Note that these formulae do not contain information about decay products explicitly, and depend on the spin projection of the ϕ meson.

Physical meaning of the SDME

ρ^0_{00} in Eq. (1.33) and $\mathrm{Re}\rho^0_{1-1}$ in Eq. (1.34) are sensitive to the spin-flip processes. The term "spin-flip" means that the spin projection of the ϕ meson (λ_ϕ) differs from the helicity of the incident photon (λ_γ). If the single spin-flip amplitude is non-zero, ρ^0_{00} have a non-zero value, as is shown in Eq. (1.44). On the other hand, non-zero $\mathrm{Re}\rho^0_{1-1}$ indicates the double spin-flip processes [Eq. (1.44)]. In the helicity-conserving case ($\lambda_\gamma = \lambda_\phi$), ρ^1_{1-1} (or $\bar{\rho}^1_{1-1}$) reflects contributions of natural- and unnatural-parity exchange processes in the t-channel. In the case of the fully natural-parity exchange (for example, Pomeron exchange), ρ^1_{1-1} reaches $+0.5$, and in the case of the fully unnatural-parity exchange such as the exchange of the pseudoscalar meson, ρ^1_{1-1} becomes -0.5. Therefore, this SDME ρ^1_{1-1} is a good indicator to know the ratio of the natural- and unnatural-parity exchanges. Note that this "ratio" is in terms of the cross section ($\sim |I|^2$), not in terms of the amplitude ($|I|^1$). Figure 1.9 shows visually the decay pattern for natural- and unnatural-parity exchanges, when the ϕ meson is emitted at zero degrees.

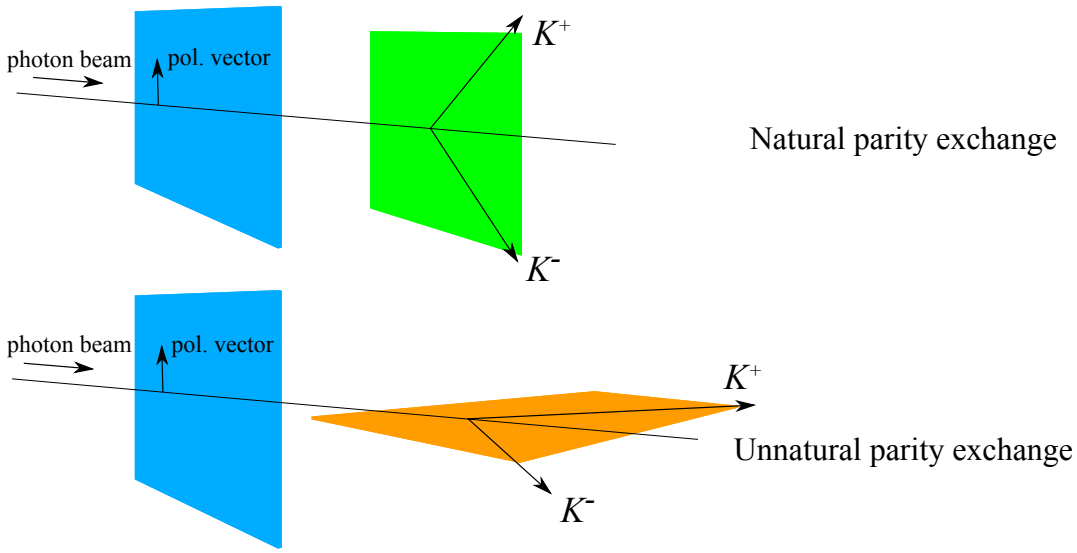

Fig. 1.9: Decay patterns for t-channel natural- and unnatural-parity exchanges. Note that these schematics represent the case when the ϕ meson is emitted at zero degrees. The blue plane is determined by the photon beam axis and the polarization vector of the incoming photon. If the natural-parity exchange process is dominant, the probability of the decay plane (green) being parallel to the blue plane becomes highest. On the other hand, if the unnatural-parity exchange process is dominant, the probability of the decay plane (orange) being perpendicular to the blue plane becomes highest.

1.3 Experimental Status of ϕ Photoproduction

Here, we review the previous measurements. To pin down the amplitudes near threshold, deuteron and ^{4}He data provide valuable information in addition to the proton data.

1.3.1 Photoproduction on the proton

At forward angles, the following processes have been considered to be dominant (Fig. 1.10).

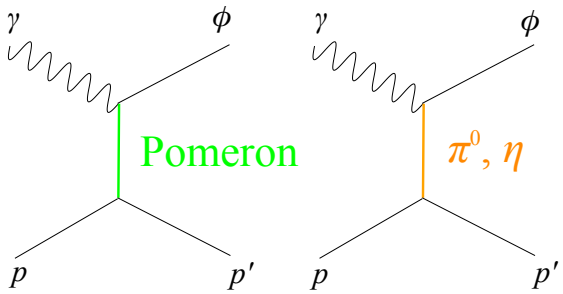

Fig. 1.10: Possible t-channel processes with different exchanged particles.

To first order, the Pomeron exchange process, which is the natural-parity exchange process, is

dominant, and the unnatural-parity (π^0, η) exchange processes could have some limited contributions.

LEPS 2005 and 2010 measurements

In 2005, the LEPS Collaboration measured the $\gamma p \to \phi p$ reaction using a linearly polarized photon beam in the low-energy region from threshold ($E_\gamma^{\rm th} = 1.57$ GeV) to $E_\gamma = 2.37$ GeV [10]. Also in 2010, precise measurements of the spin-density matrix elements with 1.7 times larger statistics was performed [38]. Figure 1.11 shows the t-dependence of the differential cross section $d\sigma/dt$. Forward peaking structures were observed, indicating the t-channel dominance.

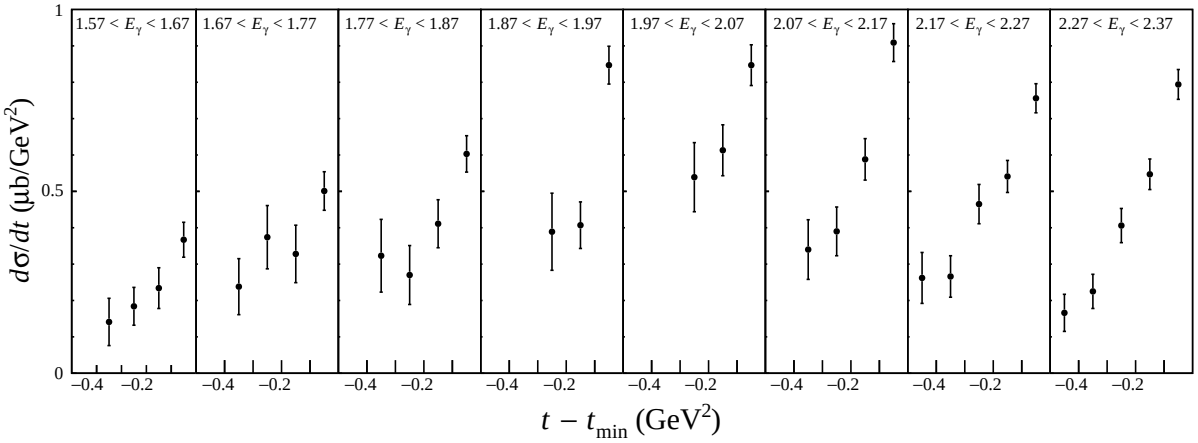

Fig. 1.11: Differential cross sections for the $\gamma p \to \phi p$ reaction in the energy range $E_\gamma < 2.37$ GeV [10].

Next, the contributions of the natural- and unnatural-parity exchange processes are quantitatively evaluated by measuring the SDMEs. Figure 1.12 shows the results of SDME measurements in the energy range below $E_\gamma = 2.37$ GeV.

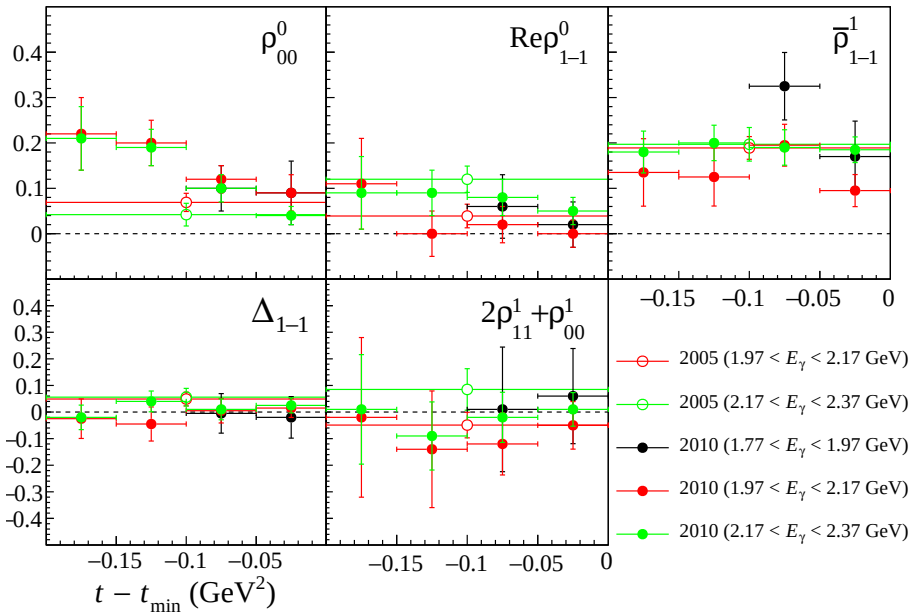

Fig. 1.12: SDMEs for the $\gamma p \to \phi p$ reaction in the GJ system [10, 38].

ρ^0_{00} and $\mathrm{Re}\rho^0_{1-1}$ are consistent with zero in the forward region, indicating the helicity conservation. Therefore, $\bar{\rho}^1_{1-1}$ indicates the ratio of natural- and unnatural-parity exchanges. The value of $\bar{\rho}^1_{1-1} \sim 0.2$ was observed at $2.17 < E_\gamma < 2.37$ GeV, which deviates from $+0.5$. This observation indicates the Pomeron (natural-parity) exchange process is dominant, while there exists about 30% pseudoscalar meson (unnatural-parity) exchange contribution in this energy region.

t-slope factor B

As shown in Fig. 1.13, the CLAS Collaboration observed that energy dependence of the t-slope factor B [Eq. (1.20)] changes at around $\sqrt{s} = 2.3$ GeV, and claimed that the production mechanism changes at around this energy [17].

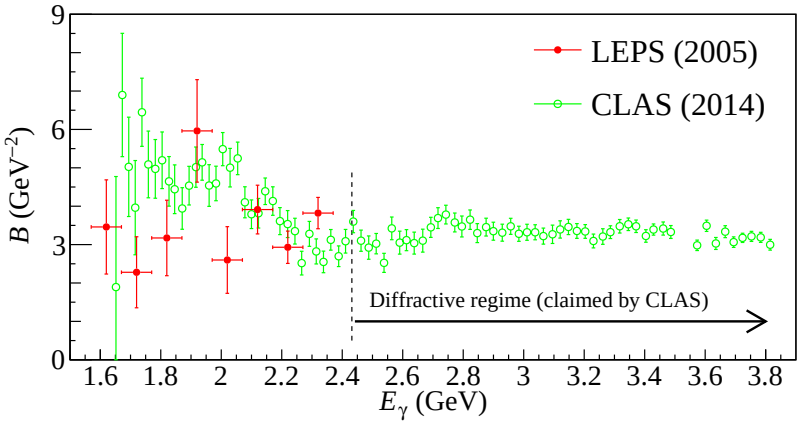

Fig. 1.13: Energy dependence of t-slope factor B. Data points are taken from Refs. [10, 17].

1.3.2 Photoproduction on the deuteron

A deuterium target can be used for the following two purposes. First, the coherent production ($\gamma d \to \phi d$) filters out the t-channel π^0 exchange, since the deuteron is isoscalar and cannot emit an isovector particle such as pion. Second, the incoherent production ($\gamma d \to \phi pn$) allows us to study the ϕ photoproduction on the neutron. Because the π-η interference is destructive in γn reactions while it is constructive in γp reactions [39], the incoherent production is useful to disentangle the π^0, η, and Pomeron amplitudes.

Coherent production

Figure 1.14 shows LEPS 2010 results of the SDMEs for the coherent production [38]. At the very forward angles ($t - t_{\rm min} > -0.05$ GeV^2), ρ^0_{00} and Reρ^0_{1-1} are consistent with zero, indicating the helicity conservation. The values of $\bar{\rho}^1_{1-1}$ are about 0.45, suggesting that the contribution from the unnatural parity exchanges is reduced. It could be understood as a result of the forbidden πdd coupling.

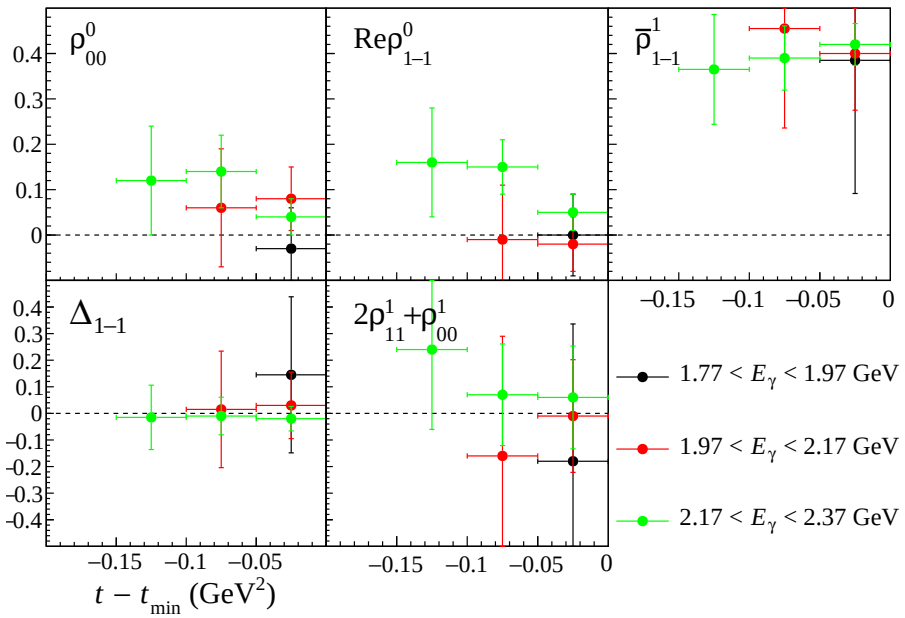

Fig. 1.14: SDMEs for the $\gamma d \to \phi d$ reaction in the GJ system [38].

Figure 1.15 shows LEPS 2008 results of energy dependence of $(d\sigma/dt)_{t=t_{\rm min}}$ for the coherent production from deuterons [40].

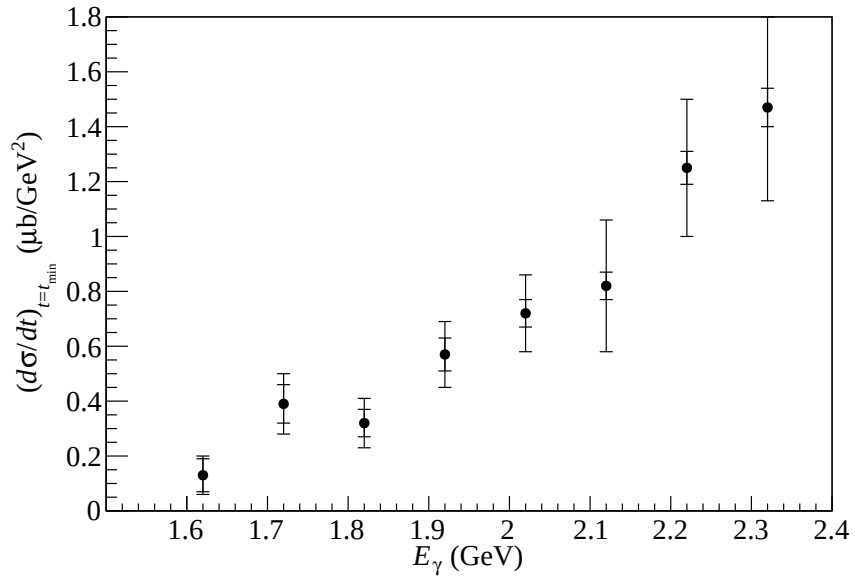

Fig. 1.15: Energy dependence of $(d\sigma/dt)_{t=t_{\text{min}}}$ for the $\gamma d \to \phi d$ reaction [40]. The smaller error bars represent the range of statistical errors.

No nonmonotonic structures can be clearly seen, and the data shows monotonically increasing energy structure within the experimental uncertainties. This measurement detected only kaons from the ϕ mesons, and the deuterons were not detected. The number of coherent events were counted using a missing mass distribution, and the small binding energy of the deuteron made the coherent/incoherent disentanglement difficult and made the systematic uncertainties large.

Incoherent production

Figure 1.16 shows LEPS 2010 results of the SDMEs for the incoherent production [38, 41]. The results are similar to those of the proton data (Fig. 1.12) except of $\bar{\rho}^1_{1-1}$. When compared to the proton data, the values of $\bar{\rho}^1_{1-1}$ are slightly larger ($\bar{\rho}^1_{1-1} \sim 0.25$), suggesting that the contribution from unnatural parity exchanges is reduced in the production on neutrons. It could be interpreted as a destructive π-η interference in the ϕ photoproduction on the neutron.

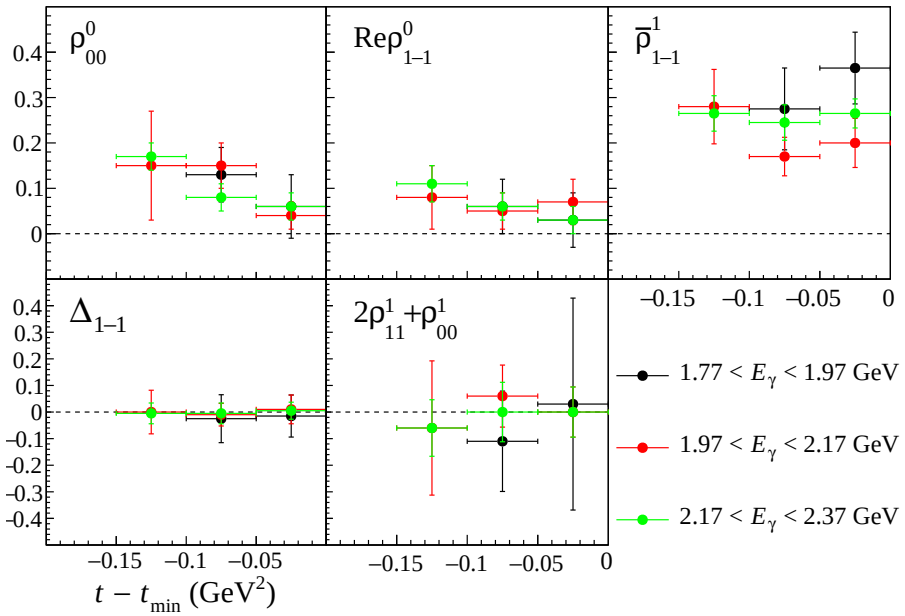

Fig. 1.16: SDMEs for the $\gamma d \to \phi pn$ reaction in the GJ system [38].

1.3.3 Coherent photoproduction on the helium-4

The coherent $\gamma^4\mathrm{He} \to \phi^4\mathrm{He}$ reaction filters out the t-channel unnatural parity (π^0 and η) exchanges, since the ^{4}He nucleus has $J^P = 0^+$ and cannot emit an unnatural-parity particle assuming the conservation of parity and angular momentum. LEPS Collaboration has measured the ϕ photoproduction from the ^{4}He target by detecting K^+K^- pairs from the ϕ meson decays [42]. The ^{4}He target has an advantage in studying the coherent production. Owing to the large separation energy of the ^{4}He nucleus, the coherent production events can be cleanly separated from the incoherent ones without detecting recoil ^{4}He nuclei, using the missing mass distribution $MM(\gamma, K^+K^-)$. Figure 1.17 shows the LEPS 2017 results of the SDMEs for the coherent production from ^{4}He. The values of $\bar{\rho}^1_{1-1}$ are close to $+0.5$, indicating the almost pure natural-parity exchanges in the t-channel. To judge whether the cross section $(d\sigma/dt)_{t_{\mathrm{min}}}$ actually deviates from the monotonically increasing energy structure at around this E_γ bin, more precise measurements are necessary.

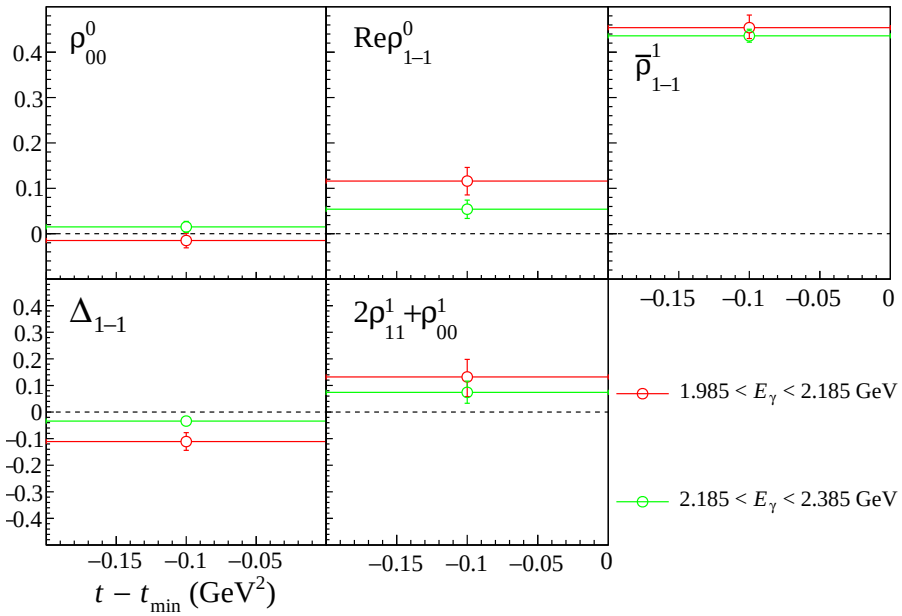

Fig. 1.17: SDMEs for the γ^4He $\rightarrow \phi^4$He reaction in the GJ system [42].

Figure 1.18 shows the energy dependence of $(d\sigma/dt)_{t=t_{\mathrm{min}}}$ for the coherent production from ^{4}He. $(d\sigma/dt)_{t=t_{\mathrm{min}}}$ increases monotonically except for the data point for $2.185 < E_\gamma < 2.285$ GeV bin.

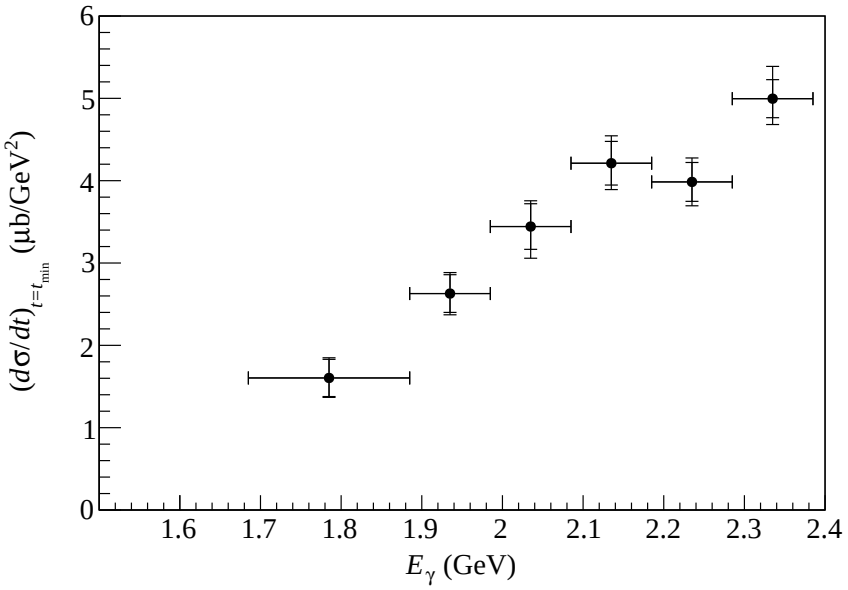

Fig. 1.18: Energy dependence of $(d\sigma/dt)_{t=t_{\mathrm{min}}}$ for the γ^4He $\rightarrow \phi^4$He reaction [42]. The smaller error bars represent the range of statistical errors.

1.4 Reaction Mechanisms for Nonmonotonic Structure

Several production mechanisms have been suggested to explain the nonmonotonic structure, such as nucleon resonances [43, 44], interference between ϕp and $K^+\Lambda(1520)$ amplitudes [45], rescattering processes [46, 47], and additional gluonic processes [48, 49].

Kiswandhi *et al.* introduced nucleon resonances ($J^P = 3/2^\pm$) in the s-channel to explain the nonmonotonic structure [43, 44]. However, this picture seems unlikely because the nonmonotonic structure observed by CLAS appears only at forward angles [17].

1.4.1 Interference between ϕp and $K^+\Lambda(1520)$

As shown in Fig. 1.19, $\gamma p \to K^+\Lambda^*$ (or Σ^{*0}) reaction shares the same K^+K^-p final state with the $\gamma p \to \phi p$ reaction.

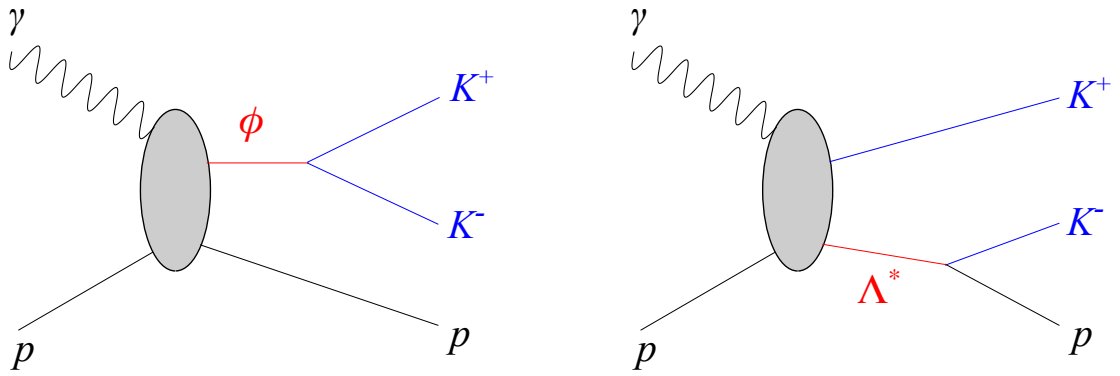

Fig. 1.19: Interference effect. $\gamma p \to \phi p \to K^+K^-p$ and $\gamma p \to K^+\Lambda^* \to K^+K^-p$ reactions share the same final state and could interfere with each other.

Therefore, these two processes could interfere with each other. Because the nonmonotonic structure occurs close to the threshold energy of $\Lambda(1520)$ production ($E_\gamma^{\text{th}} = 1.69$ GeV), the ϕp and $K^+\Lambda(1520)$ interference could account for the nonmonotonic structure. Actually, LEPS 2010 measurement observed a similar bump structure in the $\gamma p \to K^+\Lambda(1520)$ reaction [50]. Figure 1.20 shows the LEPS 2010 results.

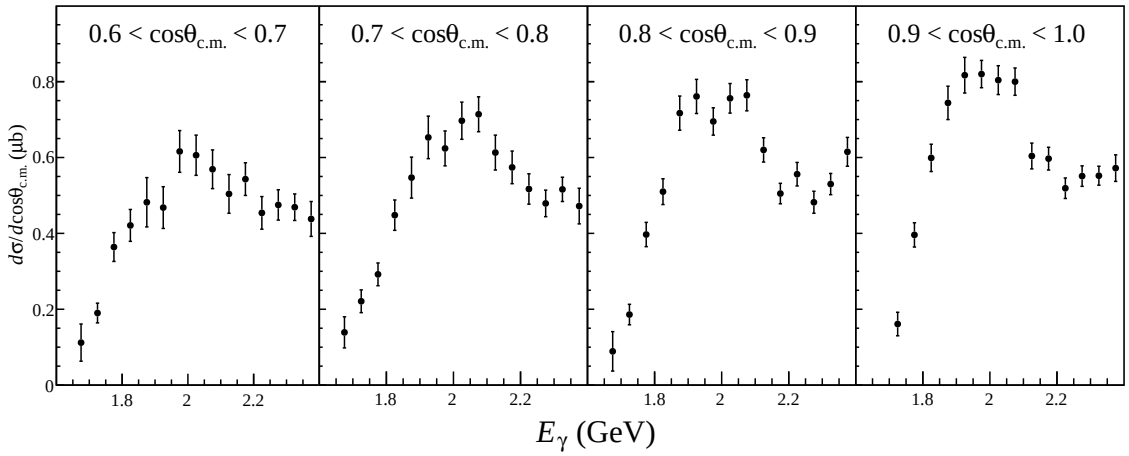

Fig. 1.20: Differential cross sections for the $\gamma p \to K^+\Lambda(1520)$ reaction [50]. A bump structure can be seen at around $E_\gamma = 2$ GeV.

This observation suggests that the ϕ-$\Lambda(1520)$ interference effect could possibly explain the nonmonotonic structure of the ϕ photoproduction. In 2016, LEPS Collaboration measured the interference effect [45]. Figure 1.21 shows the scatter plot of the invariant mass of the K^+K^- versus that of the K^-p. The box region is the ϕ-$\Lambda(1520)$ interference region, and was excluded to extract the cross section for the $\gamma p \to \phi p$ reaction without the interference effect.

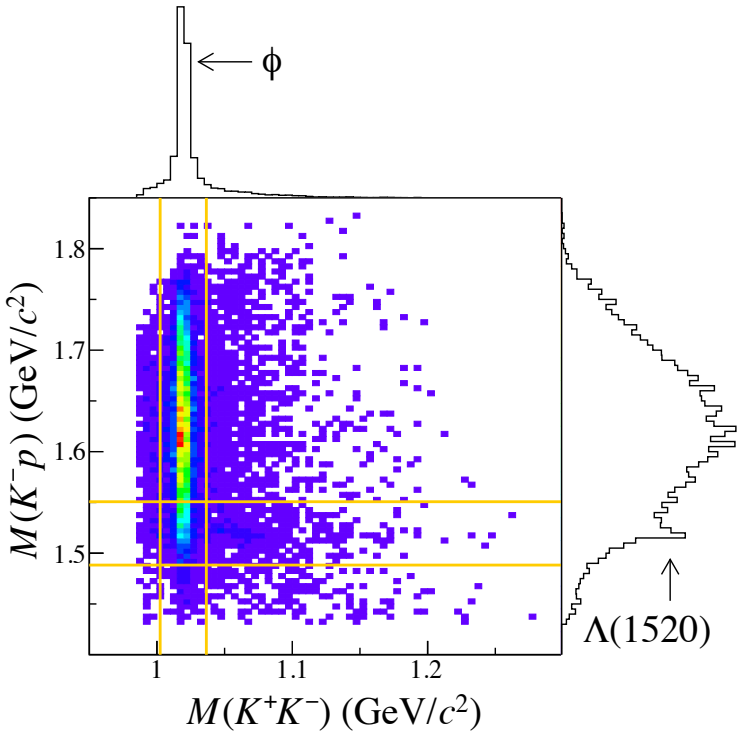

Fig. 1.21: The scatter plot of the invariant mass of the K^+K^- system versus that of the K^-p system [45]. The projections are shown onto each invariant mass axis.

Figure 1.22 shows the cross section results. Note that the LEPS 2005 results are obtained without considering the interference effect.

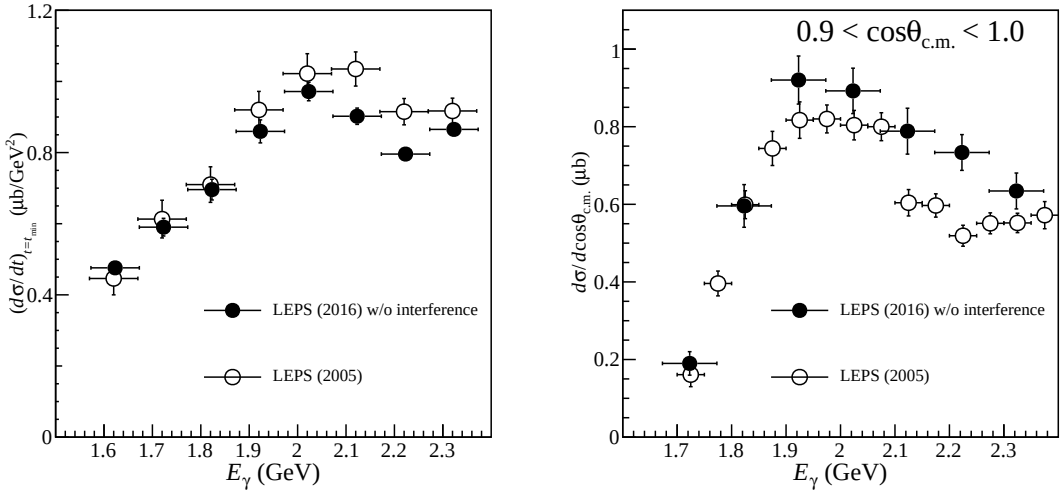

Fig. 1.22: Forward differential cross sections for (left) ϕ and (right) $\Lambda(1520)$ photoproduction [45].

The result shows us that the interference effect is too small to account for the nonmonotonic structure.

As shown in Fig. 1.19, the charged kaon K^+ must appear in the final state of the $\Lambda(1520)$ photoproduction. Therefore, we can avoid the interference effect by detecting the neutral kaon pair $K^0_S K^0_L$ from the ϕ meson decay (neutral decay mode). CLAS Collaboration has measured both the neutral and charged decay mode at $0.9 < \cos\theta_{\text{c.m.}} < 0.95$ [19, 17]. The results are shown in Fig. 1.23. As for the charged mode, they performed the analysis in two ways: including or excluding the Λ^* cut. No significant difference between the three sets of results are found, supporting the idea of a small interference effect.

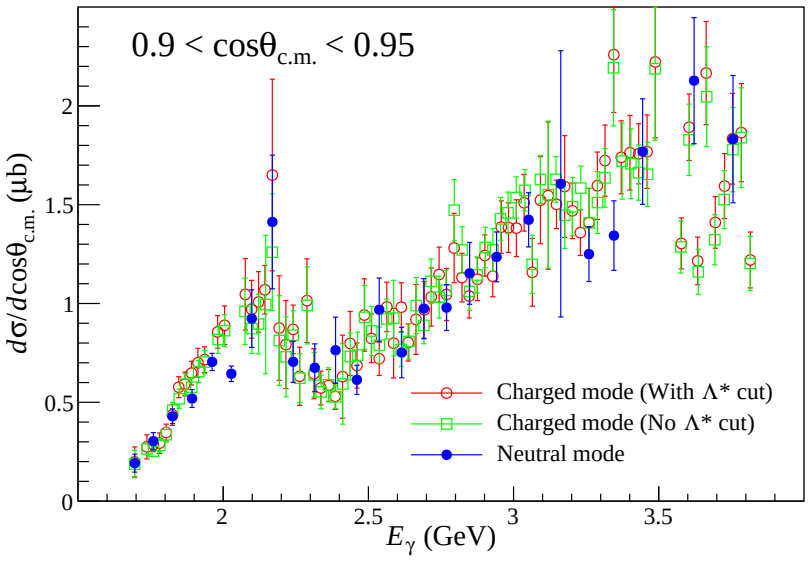

Fig. 1.23: Comparison of the charged- and neutral-mode $d\sigma/d\cos\theta_{\text{c.m.}}$ results in $0.9 < \cos\theta_{\text{c.m.}} < 0.95$ [17].

1.4.2 Rescattering effect

In 2014, Ryu *et. al.* suggested that the nonmonotonic structure can be explained by taking into account the $K^+\Lambda(1520)$ rescattering process [47]. The rescattering process is schematically shown in Fig. 1.24.

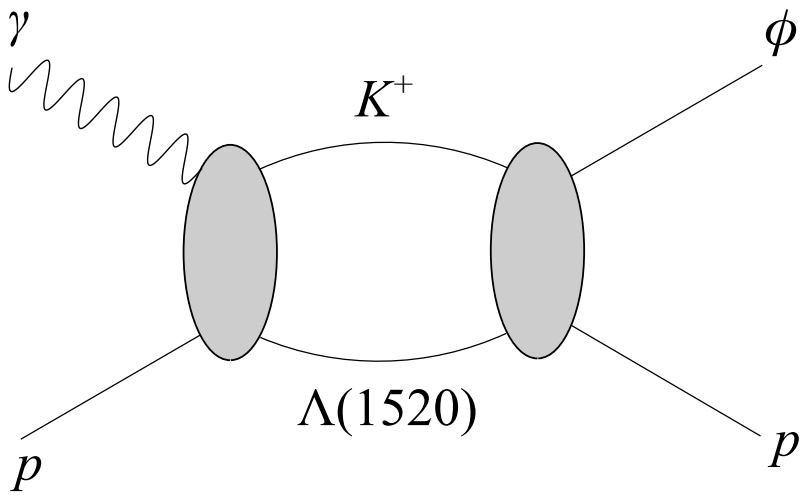

Fig. 1.24: Diagram for the rescattering effect.

First, the incoming photon scatters on the proton and produce the meson and baryon system such as $K^+\Lambda(1520)$. Next, the produced meson rescatters on the baryon and produce the ϕp final state. This rescattering effect is a kind of higher order effects. However, Ryu's calculation suggests that the rescattering process gives a significant level of contributions at low energies mainly because of the large coupling constants of the $KN\Lambda(1520)$ and ϕKK vertices. These coupling constants have been determined from the widths of decays $\Lambda(1520) \to \overline{K}N$ and $\phi \to KK$ [51, 52]. Figure 1.25 shows the calculation results of $(d\sigma/dt)_{t=t_{\rm min}}$.

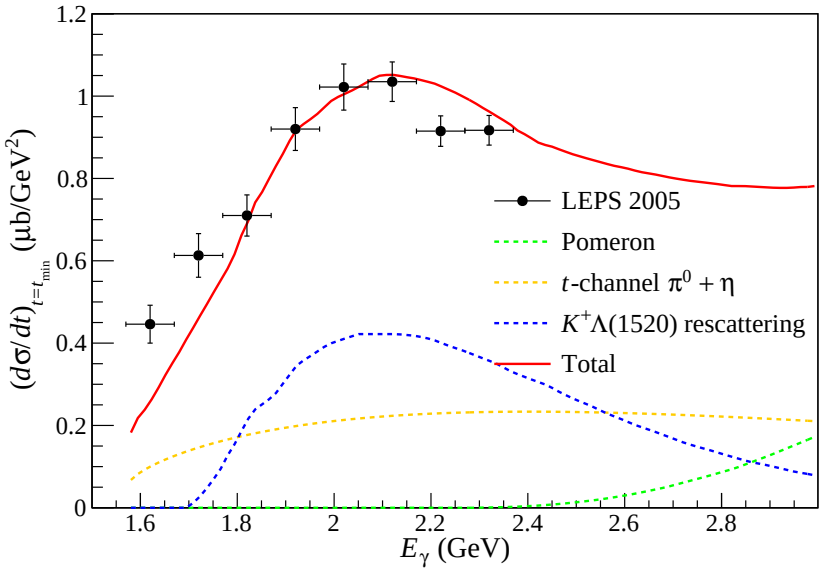

Fig. 1.25: Calculations of $(d\sigma/dt)_{t=t_{\rm min}}$ including the rescattering amplitudes [47]. Only the dominant contributions are shown in the dashed lines. There are almost no contributions of Pomeron exchange amplitude (green dashed line) at low energies because of an artificial Pomeron suppression factor. See text and Ref. [47] for details.

Since it is involved to compute the rescattering amplitude explicitly, they calculated only imaginary parts of the rescattering amplitudes using the Cutkosky rule [see Eq. (1.7)]. Also, they introduced an artificial Pomeron exchange suppression factor to enhance the rescattering effects near the threshold. Since there are no measurements of the $K^+\Lambda(1520) \to \phi p$ reaction, the form factor, which accounts for loop corrections of the second scattering [$K^+\Lambda(1520) \to \phi p$], has large uncertainties. It is determined by a fit to the experimental data for $\gamma p \to \phi p$ reaction.

As for the angular distributions, there are some inconsistencies in the paper Ref. [47]. In Fig. 11 of Ref. [47], they claims that the calculation of $\bar{\rho}^1_{1-1} = (\rho^1_{1-1} - {\rm Im}\rho^2_{1-1})/2$ reproduces the LEPS 2005 results. However, in Fig. 12 of Ref. [47] their calculation results of ρ^1_{1-1} and ${\rm Im}\rho^2_{1-1}$ are almost zero and do not reproduce the LEPS 2005 and LEPS 2010 results. Also, these results are inconsistent with those in Fig. 11 of Ref. [47]. More careful calculations are necessary at least for the spin-density matrix elements.

1.4.3 Other possibilities

Because little is known about the Pomeron behaviour at low energies, it is possible that the magnitude or phase of the Pomeron exchange amplitude changes at around $E_\gamma = 2$ GeV. If the Pomeron exchange amplitude at low energies has a large real-part component, it could interfere with meson-exchange amplitudes such as π^0 and η amplitudes. Also, the possibility of the additional gluonic contributions near the threshold has not been ruled out.

1.5 Aim of This Study

The LEPS 2005 measurement revealed that the $(d\sigma/dt)_{t=t_{\rm min}}$ for the $\gamma p \rightarrow \phi p$ reaction shows the nonmonotonic energy dependence, which cannot be explained by the t-channel Pomeron+π^0 + η model. The origin of the nonmonotonic structure is still unresolved. In addition, while the simple t-channel Pomeron+π^0 + η model is considered to work at sufficiently high energies, how low energy the model works from is still controversial. To clarify this situation and determine the contribution of the Pomeron-exchange process, we have extended the energy range from $1.5 < E_\gamma < 2.4$ GeV to $1.5 < E_\gamma < 2.9$ GeV toward the high energy side. This extension has been realized by changing the wavelength of laser photons for the backward Compton scattering technique (see section 2.1.1 for details). Then, we have measured the cross section and SDMEs, fully utilizing a highly polarized photon beam of the SPring-8/LEPS beamline. By determining the Pomeron+π^0 + η contributions using the cross section and SDMEs at high energies, we can estimate how much the additional process is necessary to explain the nonmonotonic structure.

As for the difference from the CLAS experiment, the acceptances are different in addition to the polarization degree of the photon beam. The LEPS spectrometer covers forward angles $\theta_{\rm lab} < 20$ degree, while the CLAS spectrometer covers larger angles $\theta_{\rm lab} > 20$ degree. To study of the Pomeron-exchange process, it is important to measure ϕ mesons at forward angles, and determine the differential cross section at zero degrees $(d\sigma/dt)_{t=t_{\rm min}}$ with small systematic errors. The LEPS spectrometer is the ideal spectrometer for this purpose.

In this thesis, we report the t-slope factor, $(d\sigma/dt)_{t=t_{\rm min}}$, and SDMEs for the $\gamma p \rightarrow \phi p$ reaction. We further compare our data with several theoretical models trying to understand the reaction mechanism for the nonmonotonic structure. These results are presented in the discussion chapter.

CHAPTER

TWO

EXPERIMENT

The experiment was carried out at SPring-8/LEPS[1] beamline [54] in 2007[2] and 2015. The beamline provides a few GeV polarized photon beam by the backward Compton scattering (BCS) of (deep) ultraviolet laser photons off 8 GeV electrons circulating in SPring-8 storage ring. The photon beam, whose energy is tagged by momentum-analyzing the recoil electron, is injected into the target material, and produced charged particles are detected by the LEPS spectrometer. In this experiment, linearly polarized photons at $E_\gamma = 1.5 - 2.9$ GeV are injected into the LH_2 target. We detected charged kaons, which are the decay products of ϕ mesons produced in the target, using the LEPS spectrometer. In this chapter, the experimental setup is described.

2.1 LEPS Facility

To produce the γ-ray beam, which we refer to as a 'Laser-Electron Photon' (LEP) beam, the LEPS beamline consists of three parts as shown in Fig. 2.1.

The laser photons are produced in the (b) laser hutch. Ultraviolet (UV) lasers for the maximum LEP beam energy of 2.4 GeV and deep ultraviolet (DUV) lasers for the maximum LEP beam energy of 2.9 GeV are available [56]. A polarization vector of the LEP beam is controllable by handling the laser polarization, which can be linear, circular, or elliptical. In this work, we used the linearly polarized DUV lasers to use the LEP beam with the maximum energy of 2.9 GeV.

The injected laser photons collide with electrons at the straight section in the storage ring, as shown in Fig. 2.1 (a). After the head-on collision, the produced multi-GeV photon is transported to the (c) experimental hutch. On the other hand, the recoil electron is detected and momentum-analyzed to tag the energy of the produced photon.

In this section, we describe how the photon beam is produced, and its energy is tagged.

[1] Laser Electron Photon at SPring-8 [53]

[2] Originally, the 2007 data were taken for the $\kappa(800)$ scalar meson search [55].

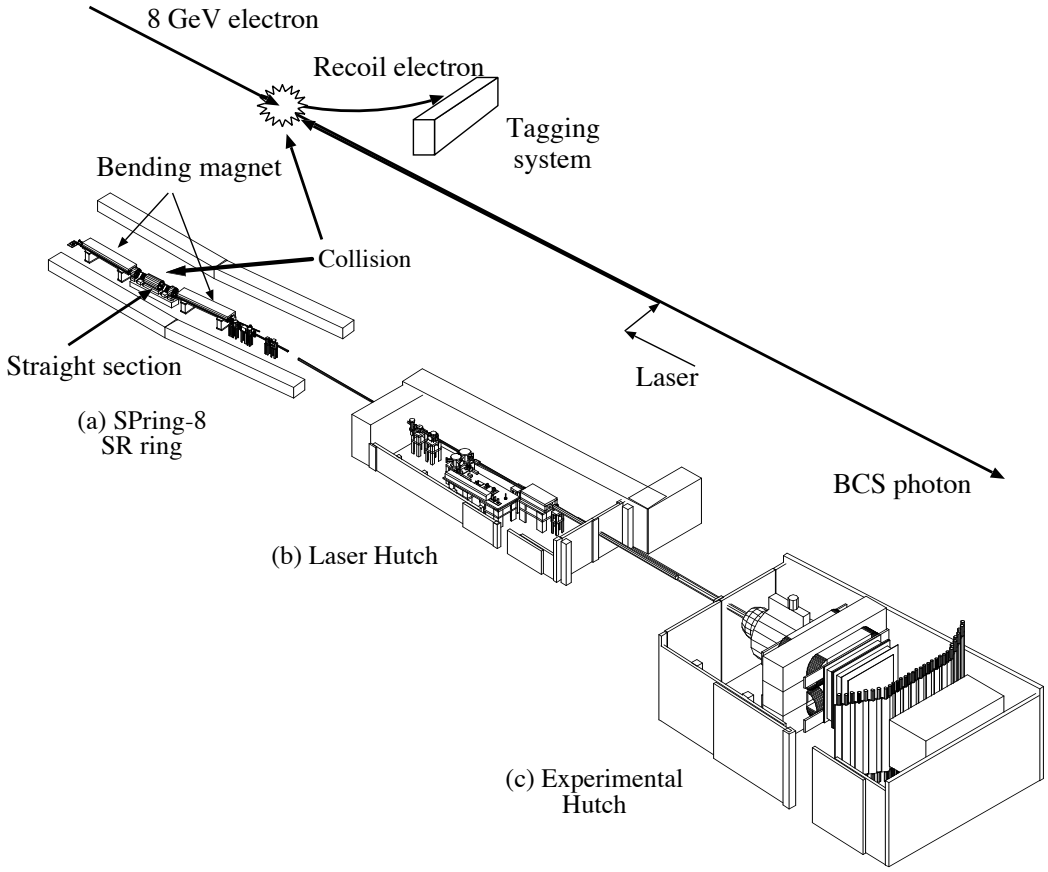

Fig. 2.1: Schematic view of the LEPS facility at SPring-8. The facility consists of three parts: (a) laser-electron collision part in the storage (SR) ring, (b) laser hutch for a laser injection, and (c) experimental hutch. A schematic explanation of the collision between an electron and a laser photon in backward-Compton scattering is inserted in the figure.

2.1.1 Backward Compton scattering

Here, we describe the principle of the Compton backscattering technique [57]. If a laser photon of energy k_1 strikes an electron of energy E as shown in Fig. 2.2, the energy of the final photon E_γ is calculated as follows:

$$E_\gamma = k_1 \frac{1 - \beta \cos\theta_1}{1 - \beta \cos\theta_2 + (k_1/E)(1 - \cos(\theta_1 - \theta_2))}, \tag{2.1}$$

where the definitions of the angles are shown in Fig. 2.2. β denotes the incoming electron velocity in units of the speed of light c.

In the LEPS experiment, $\theta_1 \simeq \pi$ (rad), and the BCS photons have the maximum energy when $\theta_2 = 0$. In this work, we used 257.2-nm and 266-nm lasers in 2007 and 2015, respectively. The electron beam energy of SPring-8 is 7.975 GeV, therefore the maximum LEP beam energies $E_\gamma^{\max}$ (Compton edges) are calculated to be 2.956 GeV and 2.894 GeV in 2007 and 2015, respectively. Note that a 355-nm laser, which is often used in the past LEPS experiment, produces the LEP beam with the maximum energy of 2.385 GeV.

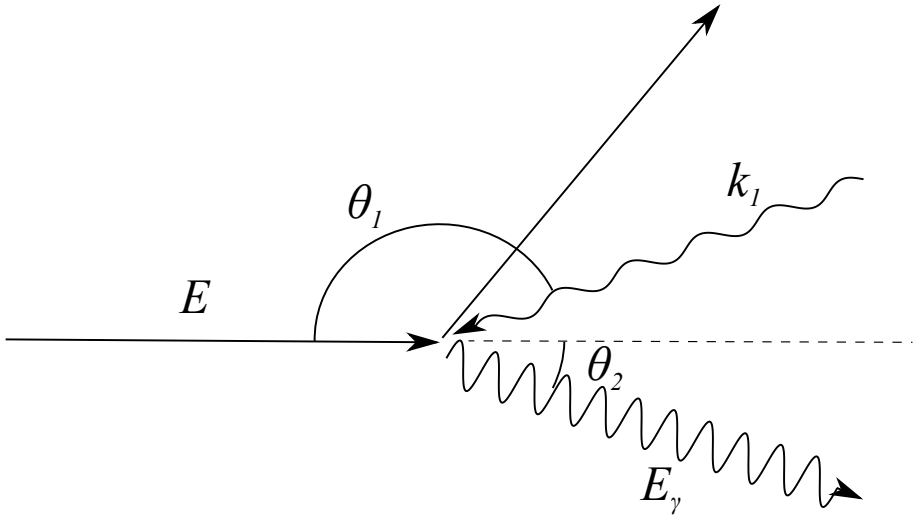

Fig. 2.2: Backward Compton scattering in the laboratory frame.

The differential cross section for Compton scattering in the laboratory frame is written as follows [57]:

$$\frac{d\sigma}{dE_\gamma} = \frac{2\pi r_e^2 a}{E_\gamma^{\max}} \left(\chi + 1 + \cos^2\alpha\right), \tag{2.2}$$

where

$$a = \frac{m_e^2}{m_e^2 + 4Ek_1}, \tag{2.3}$$

$$\chi = \frac{(E_\gamma/E_\gamma^{\max})^2(1-a)^2}{1-(E_\gamma/E_\gamma^{\max})(1-a)}, \tag{2.4}$$

$$\cos\alpha = \frac{E_\gamma^{\max} - E_\gamma(1+a)}{E_\gamma^{\max} - E_\gamma(1-a)}. \tag{2.5}$$

$r_e = 2.818$ fm is the classical electron radius, and m_e represents the electron mass.

The degree of linear polarization (P_γ) of the scattered photon is proportional to that of the laser beam (P_{laser}) as follows [57]:

$$P_\gamma = P_{\text{laser}} \frac{(1-\cos\alpha)^2}{2(\chi + 1 + \cos^2\alpha)}. \tag{2.6}$$

Figure 2.3 shows the E_γ dependence of the differential cross sections (left) and the degree of linear polarization (right) for 266-nm (2015) and 257.2-nm (2007) lasers. The results for the 355-nm laser are also shown for reference. Note that in the case of the circularly polarized photon, the polarization decreases with increasing E_γ.

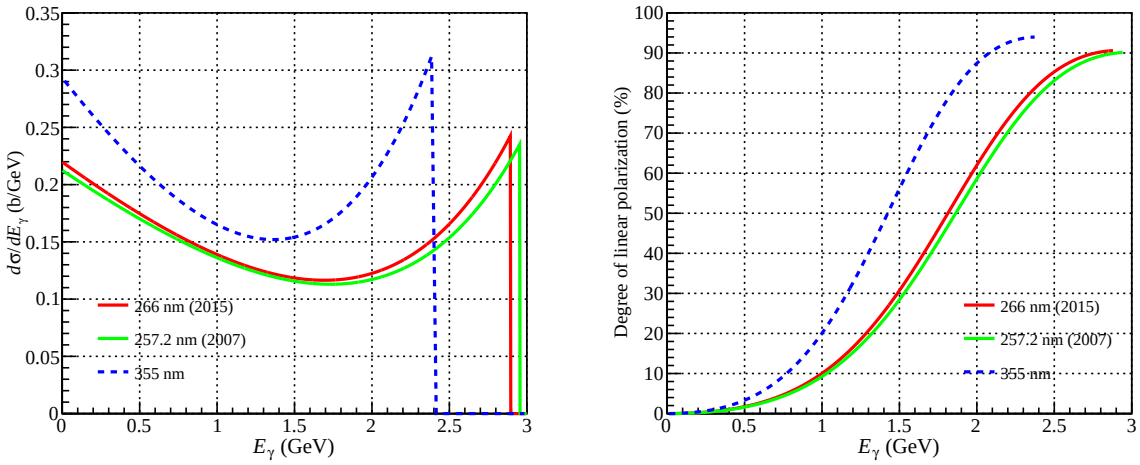

Fig. 2.3: Left: Differential cross section for the BCS process. Right: Linear polarization of the BCS photons as a function of E_γ, assuming that the degree of the laser polarization P_{laser} is 100%.

2.1.2 Laser injection system

Figure 2.4 shows the schematic view of the laser injection system.

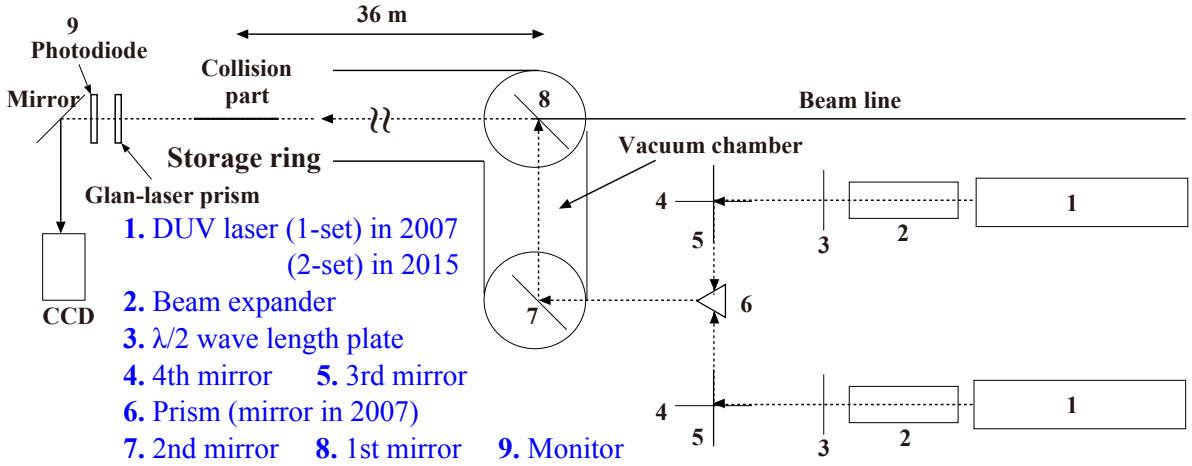

Fig. 2.4: Schematic view of the laser injection system.

Properties of the DUV lasers are summarized in Table 2.1. DUV laser photons are produced using a frequency conversion technique. A seed green laser is sent to a nonlinear optical crystal to double its frequency. This is called the intracavity frequency-doubling technique or second-harmonic generation (SHG) [58, 59]. In the lasers in Table 2.1, the β-BaB_2O_4 (BBO) crystal is used as the nonlinear optical crystal for SHG. The output laser is almost 100% linearly polarized.

Table 2.1: Properties of the DUV lasers used in this work [56]. The "$1/e^2$ diameter" is defined as a diameter of the circular region where the beam density is higher than the $1/e^2$ of the peak value.

Year	2007	2015
Laser name	Innova Sabre MotoFreD (Coherent Inc.)	Frequad-HP (Oxide Corp.)
Wavelength	257.2 nm	266 nm
Compton edge	2.956 GeV	2.894 GeV
Emission frequency	Continuous wave	Continuous wave
UV output power	1 W	1 W
$1/e^2$ diameter	0.6-0.9 mm	3.0 mm
Divergence	0.5-0.85 mrad	0.4 mrad
Power consumption	10 kW	300 W

The laser photon travels a distance of 37 m before it collides with a 8-GeV electron. Therefore, to enhance the collision efficiency of the laser photon with a narrow electron beam, we introduced the beam expander, which once enlarges a laser diameter for making a beam waist at the collision point. The orientation of the linear polarization was controlled by a quartz half-wave ($\lambda/2$) plate, whose diameter was 48 mm. To suppress the systematic error of the spin observables due to the acceptance difference, we used two configurations: the polarization vector of the incident γ ray is vertical and horizontal. The 3rd and 4th mirrors are the high-reflection coated mirrors mounted on a set of micro-stepping motors for a remote control of horizontal rotation and vertical elevation angles. The laser direction and position were tuned by controlling these two mirrors to maximize the LEP beam intensity during the data taking period. The 1st and 2nd mirrors are the aluminum coated silicon mirrors to transfer the laser photons to the straight section. A remotely rotatable Glan-laser prism and a photodiode were used to measure the degree of laser polarization. The Glan-laser prism passes photons with the polarization in a certain direction. By rotating the prism and measuring the intensity of the laser using the photodiode after the prism, the orientation of the polarization vector and the degree of polarization of the laser photons were determined. Figure 2.5 shows the intensity distribution as a function of the rotation angle of the Glan-laser prism.

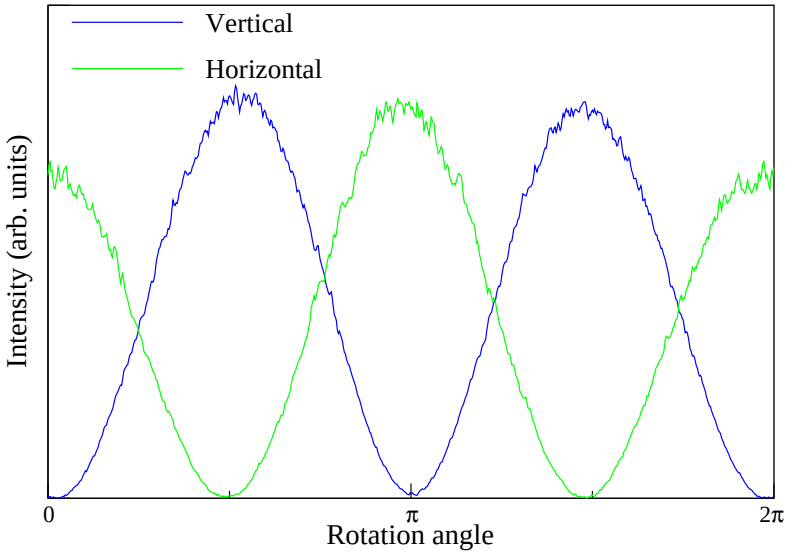

Fig. 2.5: Laser polarization measurements. The horizontal axis is the rotation angle of the Glan-laser prism. The vertical axis is the intensity measured by the photodiode. "Vertical" ("Horizontal") means the incident γ ray is vertically (horizontally) polarized.

2.1.3 Energy tagging system (tagger)

The BCS photon energy E_γ is determined by measuring the energy of the recoil electron $E_{e'}$ as:

$$E_\gamma = E_e - E_{e'}, \tag{2.7}$$

where $E_e = 7.975$ GeV is the energy of the electron circulating in the storage ring. As shown in Fig. 2.6, the injected laser photon collides with an electron at the straight section. The recoil electron has the lower energy than E_e, and slides off the track by the bending magnet located behind the interaction region. By detecting the position of the recoil electron behind the bending magnet, the momentum, or the energy, of the electron is determined, and the photon energy is tagged.

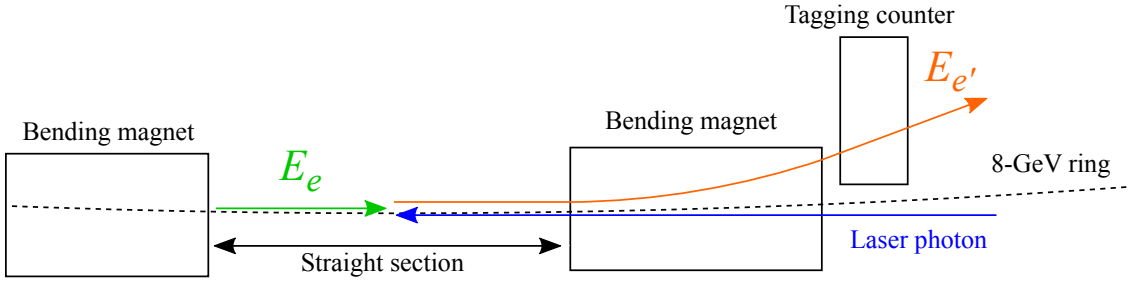

Fig. 2.6: Detection of the recoil electron.

Figure 2.7 shows a schematic view of the tagging system. The tagging system is placed at the outside of a vacuum pipe of the storage ring. Due to the mechanical reason (Fig. 2.7), the recoil electron whose energy is less than $E_{e'} = 6.5$ GeV can be measured. This corresponds to the

BCS photon energy $E_\gamma = 1.5$ GeV, therefore, the lower limit of the tagged photon energy is smaller than the ϕ meson production threshold $E_\gamma^{\rm th} = 1.573$ GeV.

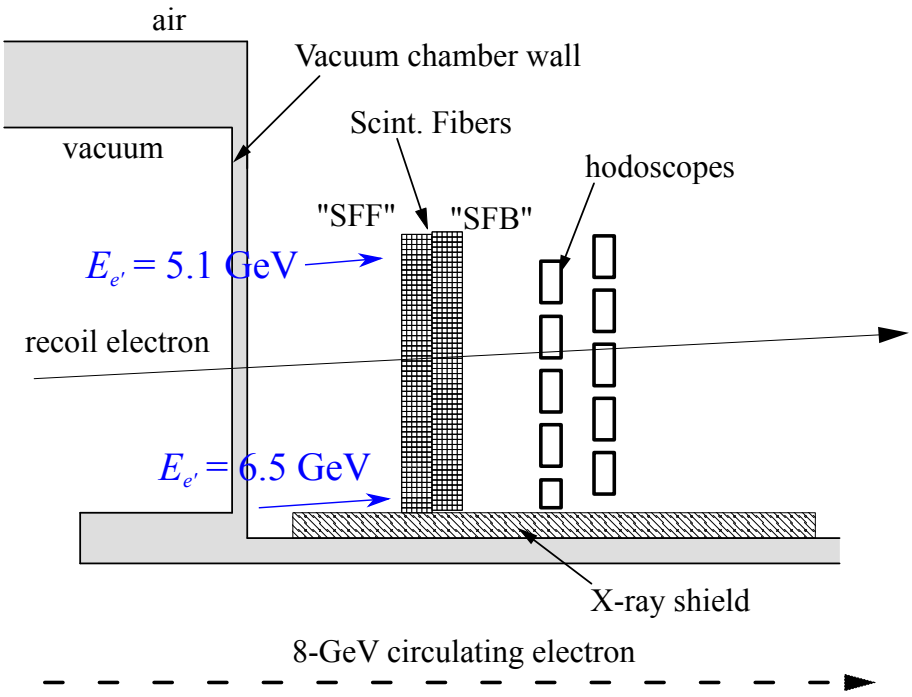

Fig. 2.7: Schematic view of the tagging system.

The tagging system consists of one layer of the plastic scintillator hodoscope (TAG-PL) and two layers of the scintillating fibers (TAG-SF).

The TAG-SF determines the hit position of an recoil electron track. Each fiber layer consists of 55 fiber bundles, and each fiber bundle is made of 6 fibers with the cross section of 1×1 mm^2. There exists 4.2% inefficient region in one fiber. The backward layer (TAG-SFB) is 0.5 mm shifted in the x direction to cover the inefficient region of the backward layer (TAG-SFF). We used multi-anode PMTs (HAMAMATSU R5900-00-M4, H6568-10) to read the signals from the fiber bundles. To prevent the X-rays from firing the tagging system, the shield was installed as shown in Fig. 2.7. In addition, to suppress the X-ray triggered events, the TAG-PL was used. We took a coincidence of the TAG-SF and TAG-PL to generate a trigger. The plastic scintillator hodoscope TAG-PL consists of 10 plastic scintillation counters. The size of the plastic scintillator is 10.0 mm high, 7.4 mm wide, and 3.0 mm thick, except for the scintillator which is closest to the storage ring. It has the width of 5.5 mm. The plastic scintillators are arranged with an overlap of 2.7 mm. The PMT (HAMAMATSAU H3164-10) was used to read the signal of the TAG-PL.

2.2 LEPS Spectrometer

The target in the experimental hutch is irradiated with the LEP beam (Fig. 2.1), and particles are produced and emitted from the target. To determine the 4-momenta and production vertices of these particles, the LEPS spectrometer, which is shown in Fig. 2.8, is used.

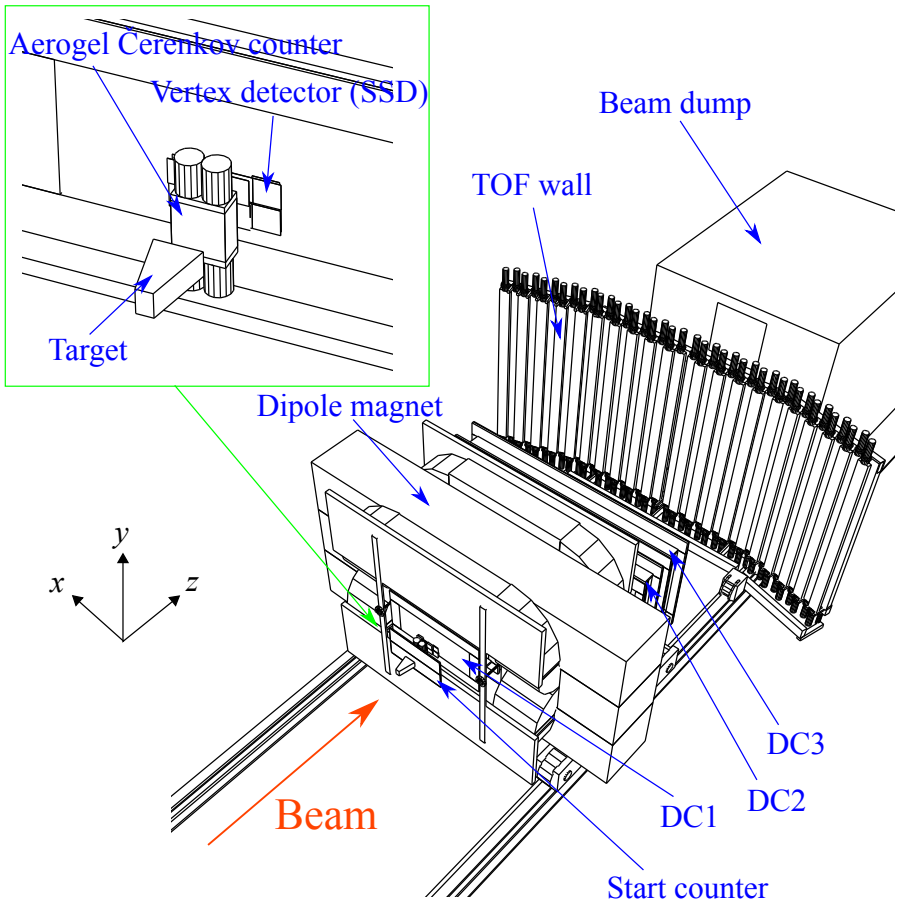

Fig. 2.8: Schematic view of the LEPS spectrometer. In the enlarged view (top left), the start counter, which is located between the target and aerogel Čerenkov counter, is not drawn for clarity.

The LEPS spectrometer covers the forward region, and can detect charged particles produced at forward angles. The angular coverage of the LEPS spectrometer is about ± 0.4 and ± 0.2 rad in the horizontal and vertical directions, respectively. For the momentum analysis, the charged particle is bent by the dipole magnet, and the trajectory is measured using the tracking devices. As for the tracking devices, the silicon strip vertex detector (SVTX, or SSD) and three drift chambers (DC1, DC2, and DC3) are mainly used[3]. SVTX and DC1 are located at the upstream of the dipole magnet, and DC2 and DC3 are located at the downstream, as shown in Fig. 2.8.

For the particle identification, time-of-fight (TOF) information is obtained by the TOF wall. There are other detectors such as the start counter to make a trigger for data acquisition system, and silica-aerogel Čerenkov counter to remove high-momentum pions and leptons. In this section, we describe the details of components of the LEPS spectrometer.

2.2.1 Upstream-veto counter

Some BCS photons convert to e^+e^- pairs before reaching the target, due to the materials in the beamline, such as air, Al windows of the beam pipe, and X-ray absorber (lead). These conver-

[3]TOF wall is also used as a tracking device when the particle passes through DC2 and TOF wall, and does not pass through DC3.

sion events are removed at the trigger level, using an upstream-veto counter. The upstream-veto counter (UPveto) is installed at 4 m upstream of the target. Figure 2.9 shows the drawing of the upstream-veto counter. This counter is made of a plastic scintillator with a size of 200 mm high, 190 mm wide and 5 mm thick. A 2-inch fine-mesh PMT (HAMAMATSU H7195) is coupled to the plastic scintillator through a light guide.

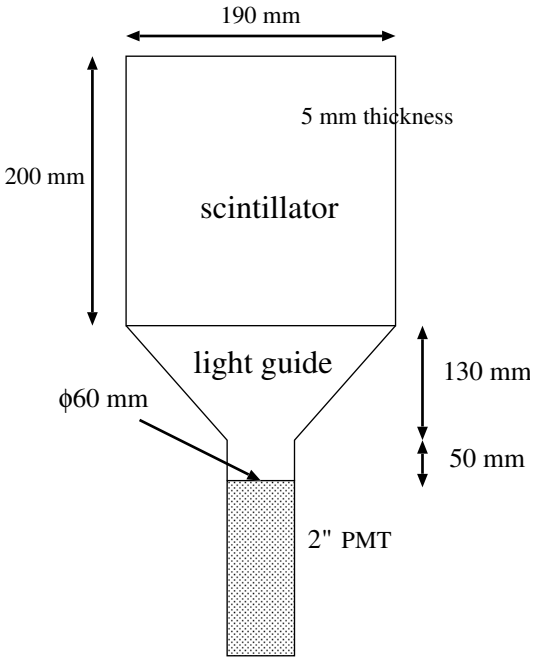

Fig. 2.9: Front view of the upstream-veto counter.

2.2.2 LH_2 target

In this work, a 15-cm-long LH_2 target was used for the measurement of $\gamma p \to \phi p$ reaction. Figure 2.10 shows a schematic view of the target cell.

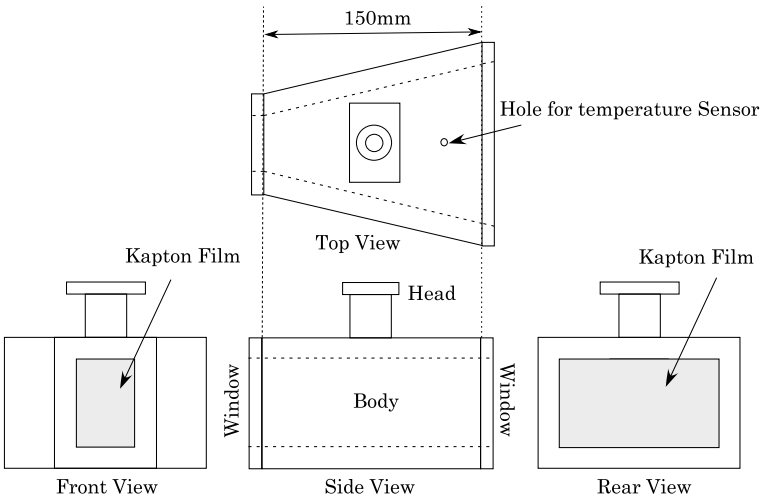

Fig. 2.10: Schematic view of the target cell.

The target cell was made of copper with a thickness of 8 mm, and the volume of the cell was 660 cm^3. The entrance and exit windows were made of kapton films with a thickness of 125 μm. The target cell was designed to be a trapezoid shape in order to reduce the probability that the produced particle hits the wall of the cell.

2.2.3 Start counter

The start counter is located at 15 cm downstream from the target center to make a trigger for the data acquisition system when charged particles from the target pass through the counter. In 2007 and 2015 data taking periods, we used different start counters.

Figure 2.11 shows the start counter (or the trigger counter, TRG) used in 2007.

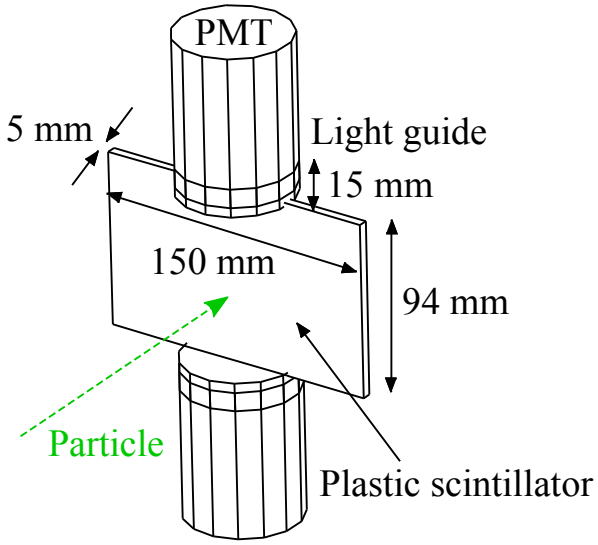

Fig. 2.11: The start counter in 2007.

It was a 5-mm-thick plastic scintillator with 94 mm high and 150 mm wide. Two 2-inch-diameter fine-mesh PMTs (HAMAMATSU H6614-01) were coupled to the top and bottom sides of the plastic scintillator through light guides with a thickness of 15 mm.

Since 2013, the large-area start counter (SC), which consists of two plastic scintillation counters, is used for the study of the pentaquark Θ^+ [60]. Each plastic scintillator counter is 172 mm high, 600 mm wide and 10 mm thick.

2.2.4 Silica-aerogel Čerenkov counter

In 2015 data taking period, a silica-aerogel Čerenkov counter (AC) with refractive index 1.008 was installed at 21 cm downstream from the target center to reject e^+e^- pair (and high-momentum pion) creation events at the trigger level, while no Čerenkov counters were used in 2007. Figure 2.12 shows the schematic view of the AC. Two sheets of silica-aerogel radiators were inserted into the black paper box. To collect the Čerenkov lights, four fine-mesh

PMT (HAMAMATSU H6614-01) were coupled to the top and bottom sides of the box. Each radiator is 110 mm high, 110 mm wide and 25 mm thick.

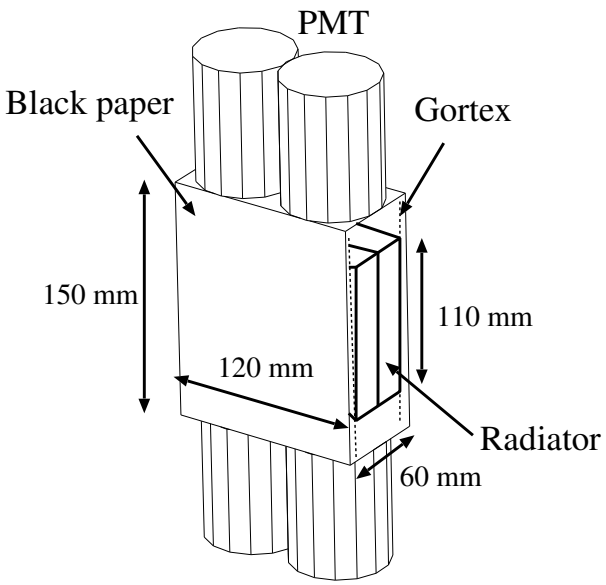

Fig. 2.12: Schematic view of the silica-aerogel Čerenkov counter.

Figure 2.13 shows the threshold momentum for the emission of Čerenkov lights as a function of the refractive index. The thresholds with the refractive index 1.03 are also shown for reference, since it had been used in the previous LEPS experiment. The momentum of the hadron is less than 3 GeV/c in the LEPS experiment (see Fig. 3.2), therefore no kaon or proton events were removed by the AC veto signal.

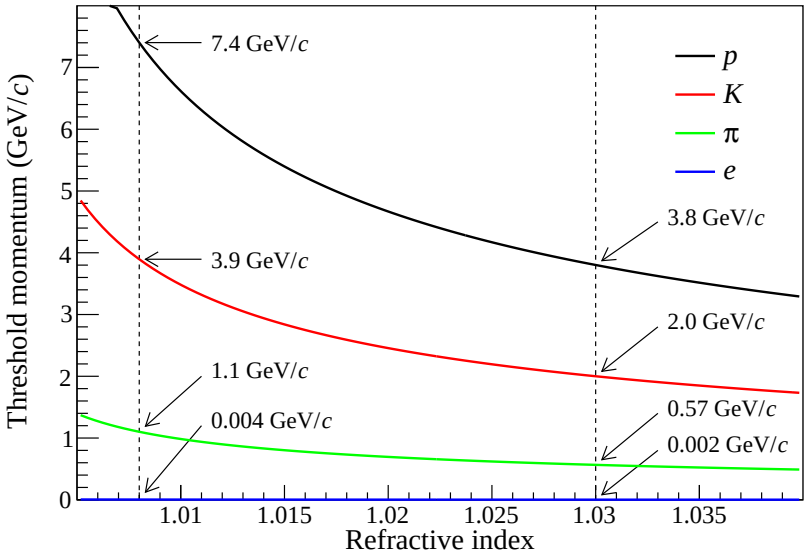

Fig. 2.13: Threshold momentum vs refractive index for proton, charged kaons, charged pions, and electrons (positrons). In this work, a Čerenkov counter with refractive index of 1.008 is used in 2015, while that with index of 1.03 was used in the previous LEPS experiment.

2.2.5 Silicon strip vertex detector (SVTX)

A silicon strip vertex detector (SVTX) was used to determine a trajectory of a charged particle together with drift chambers. By using the SVTX, the vertex position can be determined with high precision. The SVTX was placed downstream of the AC. Figure 2.14 shows the front view of the SVTX.

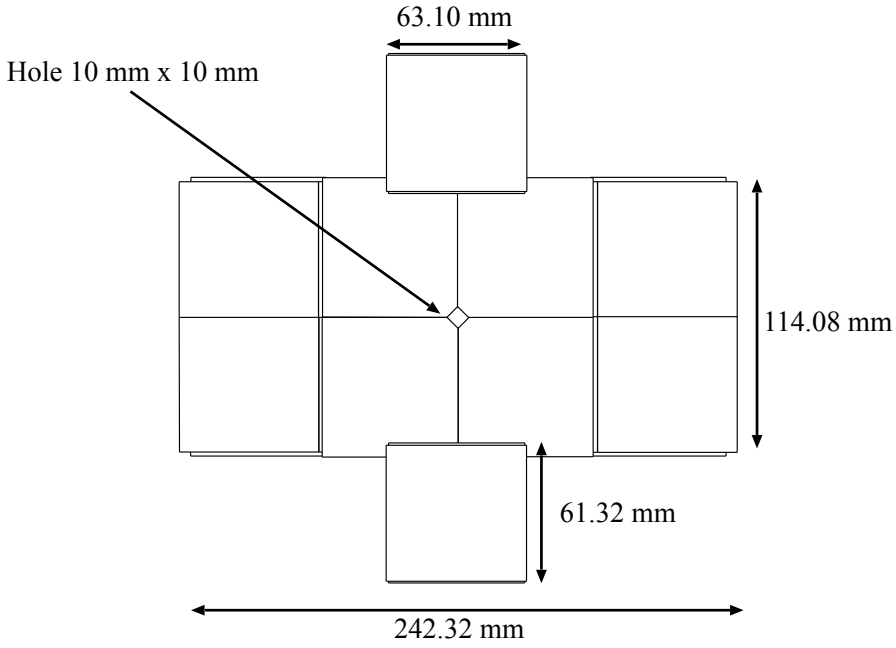

Fig. 2.14: Front view of the SVTX.

The SVTX consists of two layers of silicon strip detectors (SSD's). One of layers is used for the x-position measurement and the other is for the y-position measurement. The strip pitch is 0.12 mm and the thickness is 0.3 mm. The SVTX has a rhombic-shaped hole for the beam path which is 10 mm $\times$ 10 mm in size. VLSI chips (VA) [61] were used for the data readout. Silicon strips and the VA chip are mounted on a printed circuit board (hybrid board). The hybrid board was connected to a repeater card which contains level converters for logic signals, buffer amplifiers for analog output signals, and adjustable bias supplier for the VA chip. The VA chip is controlled by a VME board. Analog signals from the VA chip were sent to a flash ADC module through the repeater card. The analog signal from the silicon strip was read out only when the trigger signal was generated.

2.2.6 Drift chambers

We used three multi-wire drift chambers (DC1, DC2, DC3) for the track reconstruction, in addition to the SVTX. The DC1 was located between the SVTX and the dipole magnet (see Fig. 2.16), having the active area of 600 mm $\times$ 300 mm. The DC2, which has an active area of 2000 mm $\times$ 800 mm, was located behind the magnet. The DC3 is the same chamber as the DC2, and was located just behind the DC2. Each drift chamber has sense wires in three different directions (X, U, V). The X wires are vertically strained to measure the x coordinate. For the DC1, the U (V) wires are at an angle of $+45°$ ($-45°$) relative to the X wires. For the

DC2, the U (V) wires are at an angle of $+30°$ ($-30°$) relative to the X wires. The DC1 has six layers of sensitive wire planes of a configuration of X-X'-U-U'-V-X''. The DC2 (DC3) has five layers of sensitive wire planes, and the configuration is X-X'-U-U'-V. Figure 2.15 shows a schematic drawing of sense, field, and shield wires of DC1. Sense wires of each plane in DC1 are positioned with a 12 mm spacing, while those in DC2 and DC3 are positioned with a 20 mm spacing. The sense wires are surrounded by field wires arranged with a honeycomb shape. Shield wires are installed outside the field wires in order to arrange the electric field.

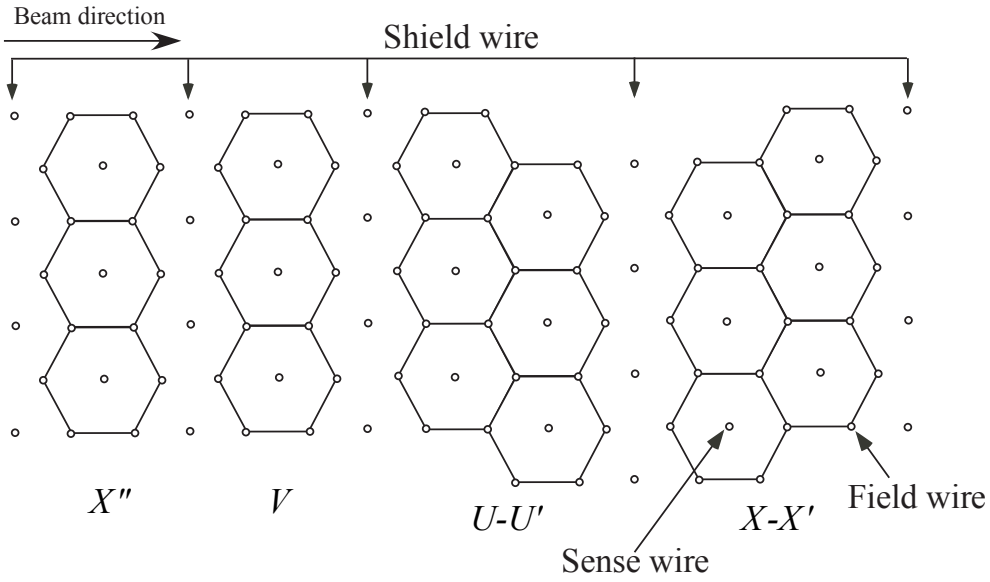

Fig. 2.15: Schematic drawing of the wire configuration of the drift chambers DC1. DC2 and DC3 have no X'' planes.

All the sense wires are made of gold-plated tungsten (Au-W). The wire diameters are 25 and 30 μm for DC1 and DC2 (DC3), respectively. The field and shield wires are made of Au-BeCu with a diameter of 100 μm. The windows are made of mylar with a thickness of 125 μm. The design parameters of the DC's are shown in Table 2.2. The gas mixture used to operate the DC's was 70% argon and 30% isobutane. The spatial resolution of the DC's was found to be approximately 200 μm. The efficiency for each plane was more than 98%.

Table 2.2: Design parameters of the DC's. The orientation is the inclination angle of the wires with respect to the vertical direction. The origin of the location z is the center of the dipole magnet.

	Plane	Orientation	#sense wires	Wire spacing (mm)	Active area $x \times y$ (mm^2)	Location z (mm)
DC1	X-X'	$0°$	48×2	12-12	600×300	-466.0
	U-U'	$+45°$	48×2	12-12		
	V	$-45°$	48	12		
	X''	$0°$	48	12		
DC2	X-X'	$0°$	104×2	20-20	2000×800	860.5
	U-U'	$+30°$	78×2	20-20		
	V	$-30°$	79	20		
DC3	X-X'	$0°$	104×2	20-20	2000×800	1260.5
	U-U'	$+30°$	78×2	20-20		
	V	$-30°$	79	20		

2.2.7 Dipole magnet

A dipole magnet was used as a momentum analyzer by bending charged particles. The magnet is located at the center of the spectrometer. The magnet has an aperture with 55 cm high and 135 cm wide. The length of the pole along the beam is 60 cm. The 800 A current was applied in order to set the strength of the magnetic field to be 0.7 T at the center. Figure 2.16 shows the y-component of the magnetic field (B_y) as a function of the z-position at $x = 0$ and $y = 0$ in 2015. TOSCA simulation program was used to obtain the distribution.

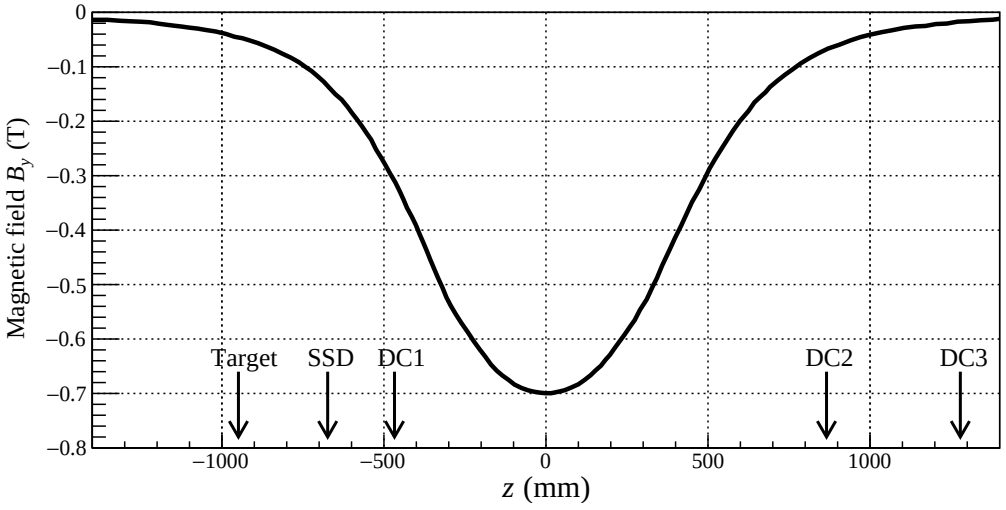

Fig. 2.16: Magnetic field B_y vs z-position at $x = 0$ and $y = 0$ (2015). The position of $z = 0$ corresponds to the center of the dipole magnet. In the 2007 data-taking period, the orientation of the magnetic field was opposite.

In 2007, the orientation of the magnetic field was opposite from that in 2015. The magnetic field was measured with a hole probe and the measured distribution was compared with the

TOSCA result. Because they show a good agreement, we used the TOSCA result in the tracking analysis.

2.2.8 Downstream e^+e^- veto counter

To reject e^+e^- pair creation events at the trigger level, the downstream e^+e^- veto counter (EEveto) was installed just behind of the DC3 as shown in Fig. 2.17.

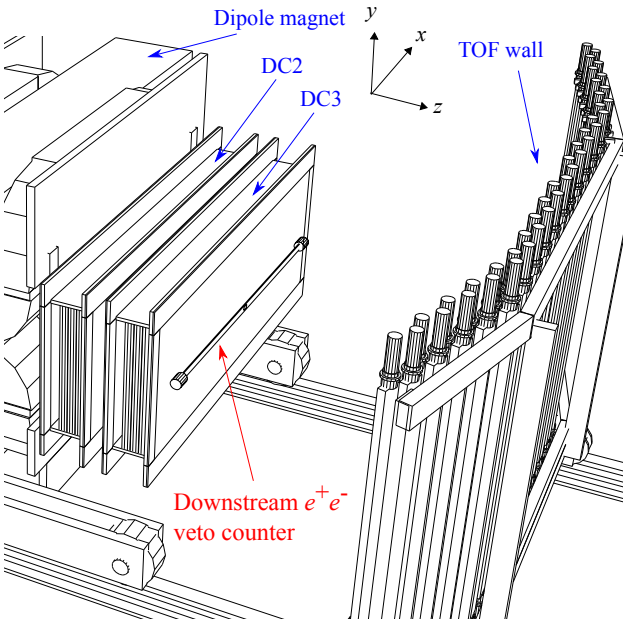

Fig. 2.17: Rear top view of the LEPS spectrometer.

Figure 2.18 shows a schematic view of EEveto counter. It is a 185-mm-long plastic scintillator. The height is 40 mm and the thickness is 20 mm. For the photon beam path, there is a 50×20 mm^2 hole in the center.

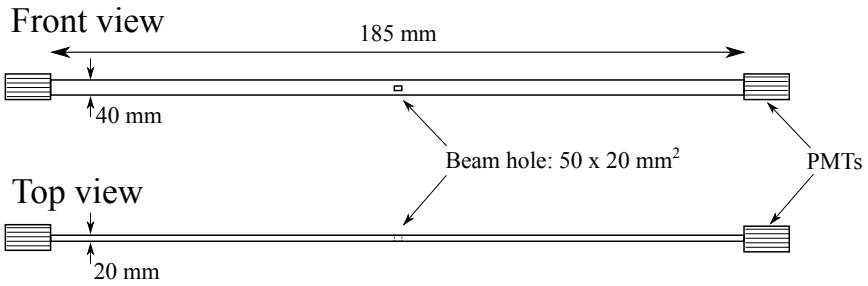

Fig. 2.18: Schematic view of the downstream e^+e^- veto counter (EEveto).

2.2.9 TOF wall

For the particle identification, the time-of-flight of the produced charged particle was measured by a TOF wall. It was placed downstream of the DC3 and determined the angular coverage of

the LEPS spectrometer. The center of the TOF wall is $z = 3151.5$ mm, where the origin $z = 0$ is the center of the dipole magnet. The schematic view of the TOF wall is shown in Fig. 2.19.

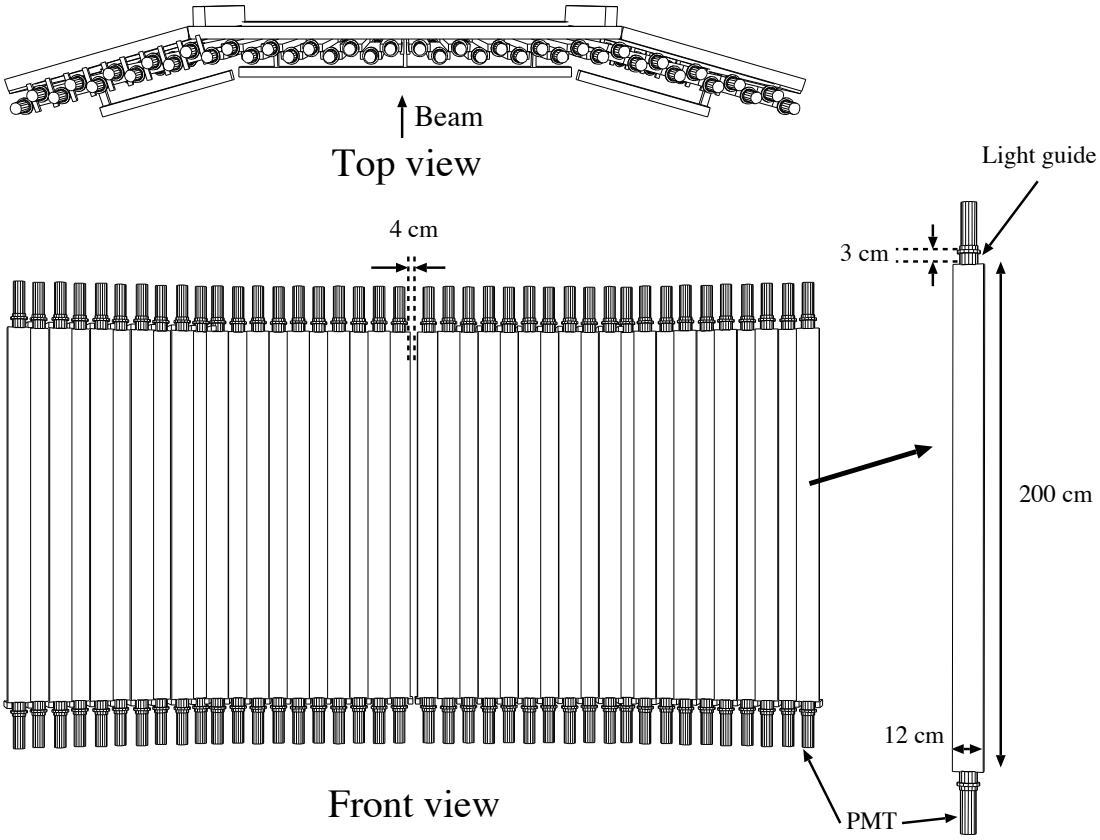

Fig. 2.19: TOF wall.

TOF wall consists of 40 plastic scintillator bars (BC-408). The size of the scintillator bar is 2000 mm long, 120 mm wide, and 40 mm thick. Two 2-inch-diameter PMTs (HAMAMATSU H7195) are coupled to the top and bottom sides of the scintillator bar through light guides with a thickness of 30 mm. Each bar is overlapped with adjacent bars by 1 cm. Sideway bars were aligned in the planes tilted by $\pm 15^\circ$ as shown in the top view of Fig. 2.19. There exists a gap of 40 mm between the central two scintillator bars to avoid being directly irradiated with the photon beam.

2.2.10 RF signal

At SPring-8, the 508.579343 MHz radio frequency (RF) system is used to accelerate an electron beam. Therefore the electrons in the storage ring has a bunch structure, whose time interval of the successive bunches is 1.966 nsec. The RF signal was used to precisely determine the event start timing for the time-of-flight measurement. Figure 2.20 shows the circuit diagram for the RF signal readout. First, the RF signals were prescaled with a factor $1/87$ using 17K32 508-MHz 30 bit counters made by DIGITAL LABORATORY. Two output signals were read with the 25 psec high resolution TDC (FASTBUS TDC 1875A). Next, one of the signals was delayed by 86 nsec relative to the other signal so that either signal can be captured (i.e. the signal comes in the time window of the TDC module) without fail. One signal was again

prescaled with a factor of $1/28$ and was divided into three output signals. These three signals were read by the 0.5 nsec low resolution TDC (FASTBUS TDC 1877S) to study the accidental rate of the tagging system. One of the output signal was delayed by 1.8 μsec and another one was delayed by 3.6 μsec as shown in Fig. 2.20.

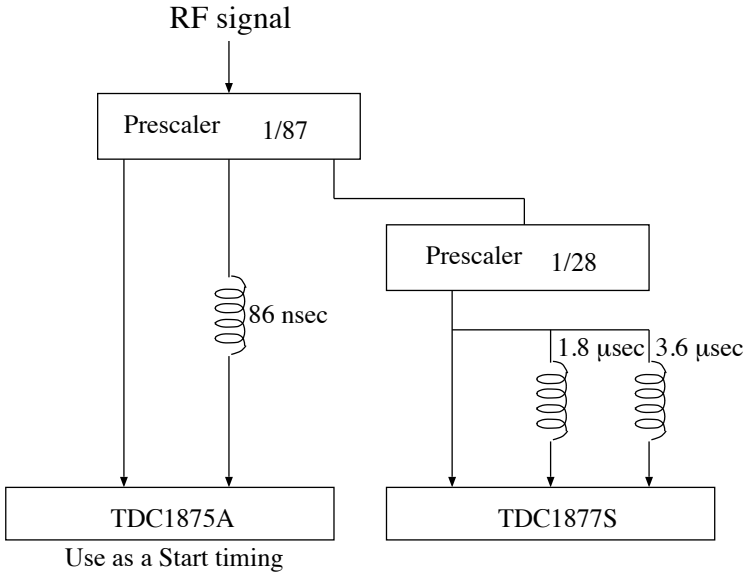

Fig. 2.20: Circuit diagram for the RF signal readout.

2.3 Data Acquisition System

In this section, the readout electronics for the LEPS detector and the trigger system are described [62, 63].

2.3.1 Electronics

Table 2.3 shows the digitizers used in this work to read out the signals from the LEPS detectors. We used two types of the analog-to-digital converter (ADC) modules to record the pulse height information. LeCroy FERA (Fast Encoding and Readout ADC) 4300B modules were used for TAG-PL, UPVeto, SC, AC, EEveto, and TOF counters. For the SVTX, flash ADC modules were used in the VME system. Timing information was recorded using two types of the time-to-digital converter (TDC) modules. The 25 psec high resolution TDC modules (FASTBUS 1875A) were used to readout the signals from the tagging counter, UPveto, start counter, silica-aerogel Čerenkov counter, EEveto, and TOF counter. The electron drift time of the drift chambers were digitized using the 0.5 nsec low resolution TDC modules (FASTBUS 1877S).

Table 2.3: Digitizers for each detector.

Detector	ADC	TDC	Used as a trigger detector
TAG-PL	FERA	FASTBUS 1875A/1877S	TAG
TAG-SF		FASTBUS 1877S	TAG
UPveto	FERA	FASTBUS 1875A	UPveto
SC	FERA	FASTBUS 1875A	SC
AC	FERA	FASTBUS 1875A	AC
SVTX	Flash ADC		
DC's		FASTBUS 1877S	
EEveto	FERA	FASTBUS 1875A	EEveto
TOF	FERA	FASTBUS 1875A	TOF ($M \geq 1$)
RF		FASTBUS 1875A/1877S	

2.3.2 Trigger

The trigger signal was generated from the tagging system (TAG), upstream veto counter (UPveto), start counter (SC), silica-aerogel Čerenkov counter (AC), downstream e^+e^- counter (EEveto), and TOF wall (TOF). In 2007, AC was not installed. The trigger conditions are listed below.

2015 TAG $\otimes$ $\overline{\text{UPveto}}$ $\otimes$ SC $\otimes$ $\overline{\text{AC}}$ $\otimes$ $\overline{\text{EEveto}}$ $\otimes$ TOF($M \geq 1$)
2007 TAG $\otimes$ $\overline{\text{UPveto}}$ $\otimes$ SC $\otimes$ $\overline{\text{EEveto}}$ $\otimes$ TOF($M \geq 1$)

Details of the trigger logic for each detector are described below.

TAG In the tagging system, OR signals of the TAG-PL and OR signals of TAG-SF were made. Then, the AND signal of them were used in the trigger logic.

UPveto A logic signal from the upstream veto counter was used as a veto signal. The width of the veto signal was set to 50 nsec.

SC For each plastic counter, AND signals of the PMTs on both sides were made. Then, the OR signal of the two AND signals from the both scintillators were used in the trigger logic. It supplied the common start and stop for TDCs. The width of the coincidence signal was set to 25 nsec.

AC The OR signal of the four PMTs was used to make a veto signal for a trigger logic. The width of the veto signal was set to 50 nsec.

EEveto The OR signal of the PMTs on both sides were used in the trigger logic.

TOF In the TOF system, the mean timing of the logic signals from the two PMTs of a TOF counter was generated by a mean timer module (CAMAC C561). The signal from the mean timer module was read by the majority logic unit module 4532 (CAMAC). The signal which satisfy the multiplicity $M \geq 1$ was used in the trigger logic.

Figure 2.21 shows the logic circuit diagram.

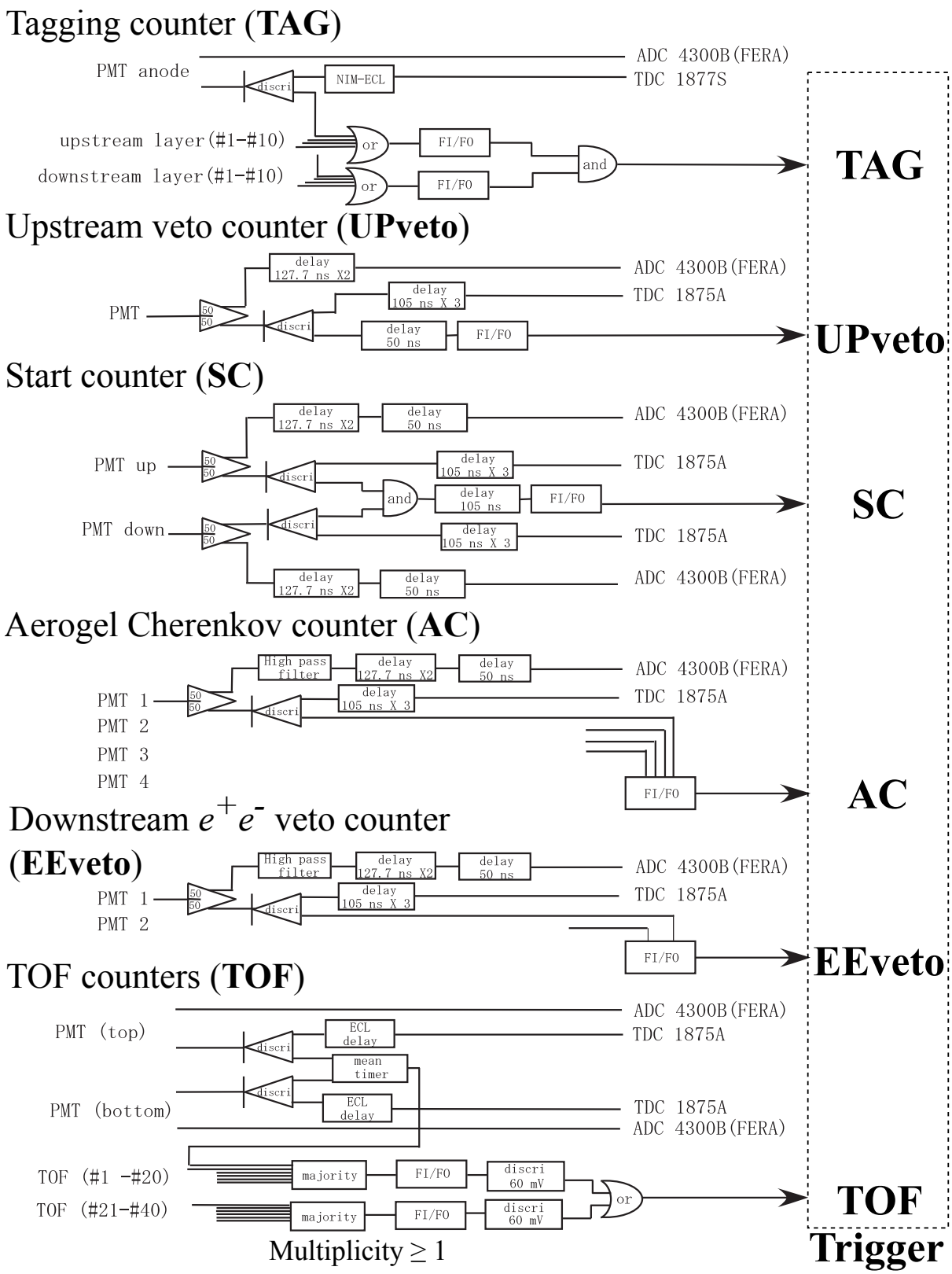

Fig. 2.21: Diagram of the readout circuits for triggers.

2.4 Data Summary

In this work, we use the data sets taken in 2015 and 2007. The differences of the detector (and laser) setups of the two data sets are summarized below.

Laser In 2007, the laser wave length was 257.2 nm (Compton edge: 2.956 GeV). In 2015, the laser wave length was 266 nm (Compton edge: 2.894 GeV).

SC In 2007, one small plastic scintillator counter was used as a start counter. In 2015, two large plastic scintillator counters were used.

Dipole magnet In 2007 and 2015, directions of the magnetic field B were opposite.

AC No ACs were used in 2007. The AC with index $n = 1.008$ was used in 2015.

The number of photons on the target is summarized in Table 2.4. The tagger dead time correction factor, transmission efficiency (0.526) and DAQ efficiency are considered.

Table 2.4: Number of photons on the target for each data set.

Year	Polarization	Laser	SC	B	AC	# photons on the target
2015	vertical	266 nm	large SC	$-y$	$n = 1.008$	3.097×10^{11}
	horizontal					2.766×10^{11}
2007	vertical	257.2 nm	small SC	$+y$	no ACs	1.082×10^{11}
	horizontal					1.103×10^{11}

CHAPTER

THREE

DATA ANALYSIS

The purpose of the data analysis is to obtain the cross section and SDMEs. Roughly speaking, the cross section is calculated using the acceptance-corrected ϕ-meson yield, the number of photons, and the number of target protons per unit area. SDMEs are calculated using only the acceptance-corrected ϕ-meson yield and the degree of polarization of the photon beam P_γ.

The differential cross section $d\sigma/dt$, which is a function of the photon energy E_γ and the Mandelstam variable t, is calculated as follows. First, E_γ and t are divided into several bins, and for each E_γ and t bin, the following $\Delta\sigma$ is calculated:

$$\Delta\sigma = \frac{N_\phi}{N_\gamma \times N_{\text{target}}} = \frac{Y_{\phi\to K^+K^-}/A/\eta_{\text{tag.ana.}}/\eta_{\text{DAQ}}/\text{Br}_{K^+K^-}}{N_{\text{tag.}} \times \omega_\gamma \times T \times N_{\text{target}}}, \tag{3.1}$$

where the meanings of the variables are listed below.

N_ϕ	Number of ϕ mesons produced at the target during the data-taking period.
N_γ	Number of photons injected into the target during the data-taking period.
N_{target}	Number of target protons per unit area.
$Y_{\phi\to K^+K^-}$	Number of $\phi \to K^+K^-$ events reconstructed by the LEPS spectrometer.
A	Acceptance of the LEPS spectrometer.
$\eta_{\text{tag.ana.}}$	Tagger analysis efficiency (0.969).
η_{DAQ}	DAQ (trigger) efficiency.
$\text{Br}_{K^+K^-}$	Branching fraction of $\phi \to K^+K^-$ decay (0.489).
$N_{\text{tag.}}$	Number of recoil BCS electrons counted by the tagger (dead-time corrected).
ω_γ	Photon fraction of the E_γ bin.
T	Transmission efficiency (0.526).

Here, the transmission efficiency T is the probability that a BCS photon travels from the collision point to the target without conversion to the e^+e^- pair in materials.

Next, by dividing the $\Delta\sigma$ by t bin size Δt, we obtain the differential cross section $d\sigma/dt$. On the other hand, the SDMEs are determined only by $Y_{\phi\to K^+K^-}$, A, and P_γ. Note that $\eta_{\text{tag.ana.}}$, η_{DAQ}, $\text{Br}_{K^+K^-}$, $N_{\text{tag.}}$, and T do not depend on E_γ or t bins. ω_γ depends only on the E_γ bin, and other variables ($Y_{\phi\to K^+K^-}$ and A) depend on both the E_γ and t bins[1].

In this chapter, data analysis method to extract the variables in Eq. (3.1) is described.

[1] Furthermore, the yield $Y_{\phi\to K^+K^-}$ and acceptance A depend on the angular bin, when calculating the decay angular distributions.

3.1 Four Momentum Reconstruction

Track reconstruction for momentum analysis, vertexing, and particle mass reconstruction (particle identification) using time-of-flight information are described in this section. These analyses are conducted by the analysis code `LEPSana`, which is developed by the LEPS Collaboration.

3.1.1 Track reconstruction

The 3-momentum of a track is reconstructed from the hit positions of the tracking devices. The particle trajectory is reconstructed by solving the equation of motion in the magnetic field using Runge-Kutta method.

First, to find track candidates, straight line fittings are performed at an upstream and downstream of the dipole magnet separately. The hit position information of the SVTX and DC1 is used for the upstream fitting, and that of the DC2 and DC3 is used for the downstream fitting. After that, consistency of the upstream and downstream straight tracks is checked by using the cross point. Next, the track fitting considering the magnetic field is carried out using the Runge-Kutta method. In this fitting process, Kalman filtering algorithm is applied to take into account multiple scatterings [64].

The momentum resolution is momentum-dependent, and can be phenomenologically parametrized as follows:

$$\left(\frac{\sigma_p}{p}\right)^2 = \frac{a_1^2}{\beta^2} + p^2 a_2^2, \tag{3.2}$$

where p is the momentum, and β is the velocity of the particle. The first term originates from the multiple scattering effect. The multiple scattering term is dominant when the particle has low momentum. The second term is the contribution from the resolution of the LEPS spectrometer. In the high momentum region, this term becomes dominant. Note that the parameter a_1 is dimensionless, and a_2 has a unit of GeV^{-2}. This parametrization is used to construct momentum-dependent mass boundaries for the particle identification, which is described in the following subsection.

3.1.2 Particle identification

RF selection

Time of flight is measured for the particle identification. The stop time is determined by the TOF counter, and we use the RF signal to determine the start time. The timing resolution of the RF signal is 12 psec, and can be ignored compared with other detectors' timing resolutions such as the TOF wall and SC. As described in section 2.2.10, the RF signals were prescaled with a factor $1/87$, and the recorded RF signal timing does not necessarily corresponds to the timing of the electron bunch in which the BCS photon is generated. That is, the RF signal timing has $1.966 \times n$ nsec ambiguity when determining the start time (the BCS photon timing), where 1.966 nsec is the time interval of the successive electron bunches and n is an integer.

To resolve the ambiguity, we use the timing of the SC. Figure 3.1 shows the time difference between the RF signal and SC. The electron bunch structure with 1.966 nsec intervals is clearly seen. We shifted the RF signal timing by $1.966 \times n$ nsec so that the RF $-$ SC distribution shows only one peak. We call this procedure the "RF selection". As shown in Fig. 3.1, the peaks are not perfectly separated and some events are classified in the neighboring peak. These "mis-selected" events cause the particle misidentification, whose fraction is less than 1%.

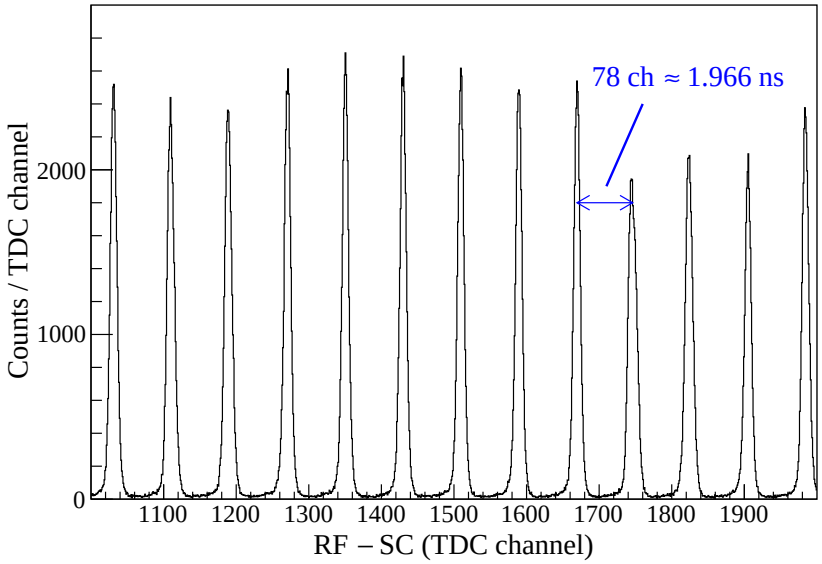

Fig. 3.1: Time difference between the RF signal and SC. The widths of the peaks are determined by the timing resolution of SC. Note that the resolution of the TDC (FASTBUS 1875A) is 25 psec.

Mass reconstruction

The particle mass m is obtained by measuring the time of flight Δt as follows:

$$m^2 = p^2 \left[\left(\frac{\Delta t}{L} \right)^2 - 1 \right], \tag{3.3}$$

where the momentum p and path length L are obtained from the track reconstruction. By differentiating Eq. (3.3),

$$d(m^2) = 2m^2 \frac{dp}{p} + 2(p^2 + m^2) \frac{d(\Delta t)}{\Delta t} - 2(p^2 + m^2) \frac{dL}{L} \tag{3.4}$$

is obtained. The third term is negligible compared with the other terms. Therefore, the resolution of mass squared can be written as:

$$\sigma^2_{m^2} = 4m^4 \left(\frac{\sigma_p}{p} \right)^2 + 4(p^2 + m^2)^2 \left(\frac{\sigma_{\Delta t}}{\Delta t} \right)^2 \tag{3.5}$$

Using Eq. (3.2), the mass resolution can be parametrized as follows:

$$\sigma^2_{m^2} = 4m^4 \left(1 + \frac{m^2}{p^2} \right) a_1^2 + 4m^4 p^2 a_2^2 + 4p^2(p^2 + m^2) \left(\frac{c}{L} a_3 \right)^2, \tag{3.6}$$

where $a_3 = \sigma_{\Delta t}$, and has a unit of time. The parameters were obtained by MC simulation to be $a_1 = 0.00458$, $a_2 = 0.00323$ GeV^{-2}, and $a_3 = 0.175$ nsec. As for the path length L, we use the typical value $L = 4100$ mm. This momentum-dependent mass resolution is used to construct particle identification (PID) boundaries, which are shown later in Fig. 3.3.

Figure 3.2 shows the scatter plot of the momentum vs reconstructed mass/charge. The particle loci are separately seen.

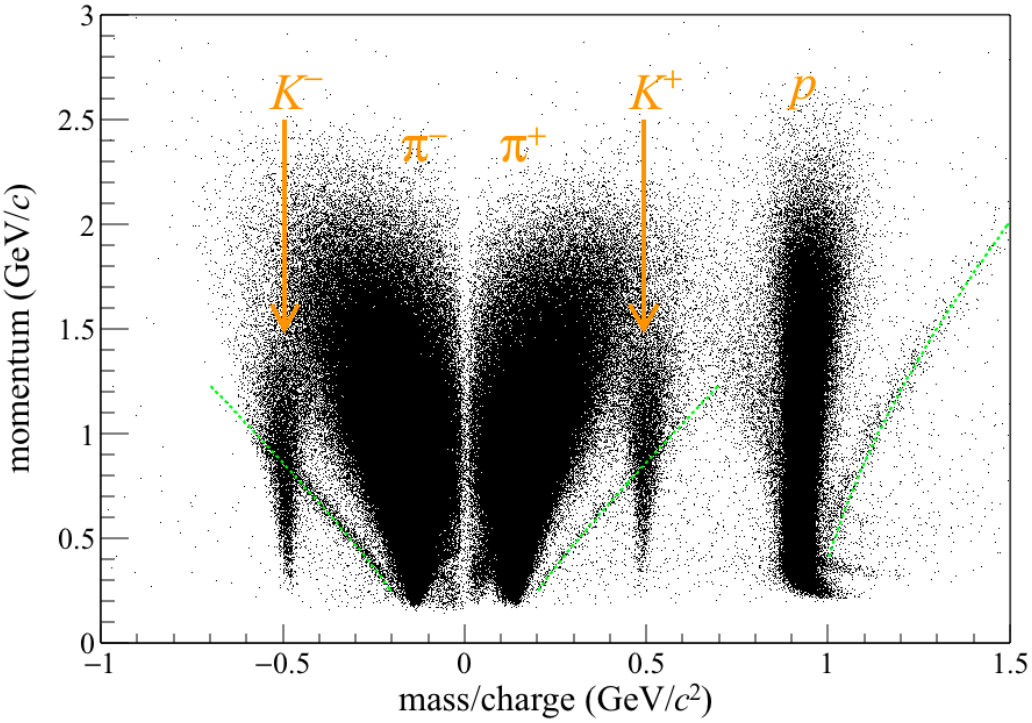

Fig. 3.2: Momentum vs reconstructed mass/charge. Pions, kaons, and protons are seen. The inclined lines are due to the RF mis-selection. See text for details.

The inclined lines are due to the mis-selection of the RF signals. Because the time of flight Δt can be written as

$$\Delta t = L\sqrt{1 + \left(\frac{m_{\text{nominal}}}{p}\right)^2}, \tag{3.7}$$

using the particle nominal mass m_{nominal}. Therefore, from Eq. (3.3) the reconstructed mass m becomes as follows when a neighboring RF bunch is selected:

$$m^2 = p^2\left[\left(\frac{L\sqrt{1 + \left(\frac{m_{\text{nominal}}}{p}\right)^2} \pm 1.966 \text{ nsec}}{L}\right)^2 - 1\right], \tag{3.8}$$

where 1.966 nsec is the RF bunch interval. Eq. (3.8) is drawn in Fig. 3.2 as dashed green lines.

3.1.3 Energy loss correction

The particle loses a part of its energy in matter. For the energy loss correction, we use the following phenomenological paramaterization of the energy loss dE/dx:

$$\frac{dE}{dx} = \frac{c_1}{\beta^{c_2}}, \tag{3.9}$$

where β is the velocity of the particle. The parameters c_1 and c_2 depend on the material, and are listed in Table 3.1.

Table 3.1: Parameters for the energy loss correction.

Material	c_1	c_2
LH_2	0.0251	1.75
SC	0.182	1.70
AC	0.194	1.68
SSD	0.342	1.64
Air	0.000195	1.69

The 3-momentum of the particle is corrected using Eq. (3.9). The correction factor depends on the velocity and scattering angle of the particle, and typically, the corrected momentum is 0.6% larger than before correction.

3.2 Event Selection

After the track reconstruction, the $\gamma p \to K^+K^-p$ events were selected by applying several cuts on the reconstructed kinematic variables. Note that these events are dominated by the $\gamma p \to \phi p \to K^+K^-p$ reactions. Here, we describe the cut-flow in this analysis.

3.2.1 Kaon identification

In this work, we used the events in which K^+ and K^- were detected by the LEPS spectrometer, and the recoil proton in the final state is identified using the missing mass distribution. Figure 3.3 shows the kaon identification.

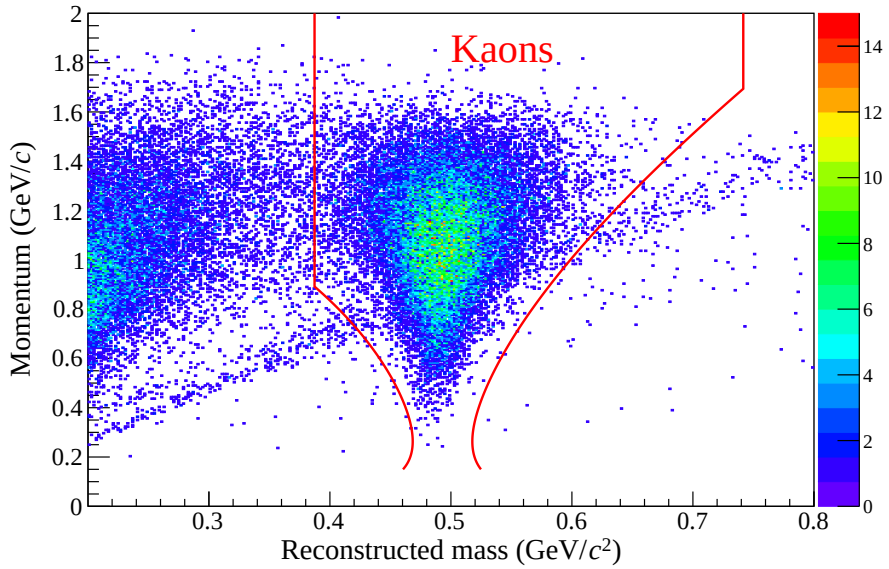

Fig. 3.3: Kaon identification. Two track events with opposite charge whose reconstructed masses are in the range of $[0.2, 0.8]$ GeV$/c^2$ (rough kaon selection) are plotted. The red boundary is the 4σ boundary. See text for details.

We used the momentum-dependent PID boundaries in low momentum region. The boundaries correspond to the $4\sigma_{m^2}$ mass resolution. In high momentum region, the constant values $\sqrt{0.15}$ GeV$/c^2$ and $\sqrt{0.55}$ GeV$/c^2$ were used to separate kaons from pions and protons, respectively. The momentum of the kaon from ϕ decay is not large (< 1.6 GeV$/c$) due to the small decay Q value ($= 32.1$ MeV), so π/K separation power is good enough even when we use the loose PID cut (Fig. 3.3).

3.2.2 Vertexing

To select events in which the ϕ meson was produced at the LH_2 target, we used the vertex of K^+ and K^- tracks, which was obtained by calculating the closest point between the K^+ and K^- tracks. The reconstructed vertices are shown in Fig. 3.4.

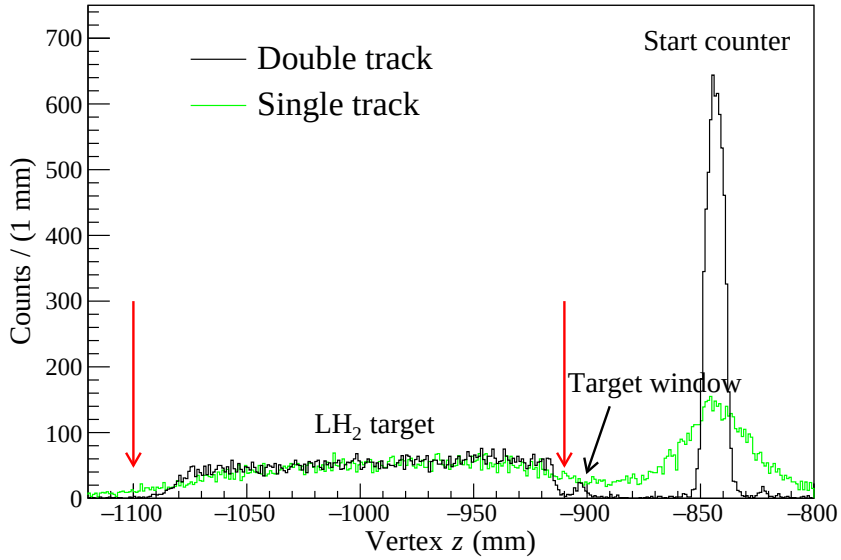

Fig. 3.4: The z-coordinate distribution of the reconstructed vertices. The LH_2 target is separately seen in the black histogram (double track). The red arrows indicate the cut points to select the target.

The black histogram is the z-coordinate distribution of the vertices of the K^+ and K^- tracks (double track). For reference, the single track vertex distribution, which was determined by K^+ track and beam axis (z-axis), is also shown (green histogram). In this analysis, we use the double track events, therefore the vertex resolution is good enough to separate the LH_2 target from other materials such as the start counter and the vacuum window ($z \sim -900$ mm). To select the target, we applied $-1100 <$ vertex-$z < -910$ mm cut as shown in Fig. 3.4 (red arrows).

3.2.3 Good track selection

Next, the tracking quality is checked. We use the χ^2 probability to test the goodness of track fitting. To consider tracks with different degrees of freedom together, χ^2 value of the track fitting with n degrees of freedom is converted to the χ^2 probability as follows:

$$P(\chi^2; n) = \int_{\chi^2}^{\infty} f(x; n) dx, \tag{3.10}$$

where $f(x; n)$ is the probability density function of the chi-square distribution with n degrees of freedom. Here, the number of degree n is the number of position measurements used for the track reconstruction minus the number of track parameters 5. The $P(\chi^2; n)$ means the probability that a random variable, which follows the chi-square distribution with n degrees of freedom, is greater than the actual observed χ^2 value. If the random variable χ^2 follows the chi-square distribution [$f(x; n)$], the converted random variable $P(\chi^2; n)$ follows the uniform distribution between 0 and 1. Figure 3.5 shows an observed $P(\chi^2; n)$ distribution of K^+ and K^- tracks.

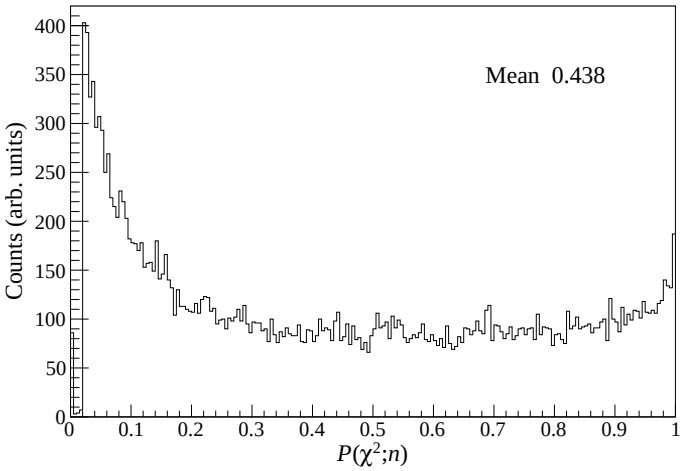

Fig. 3.5: $P(\chi^2; n)$ distribution.

Because the hit positions for each tracking plane are not independent, the $P(\chi^2; n)$ distribution deviates from the flat distribution. $P(\chi^2; n) > 0.02$ cut was used to select the good track events.

Also, the number of outliers can be used to evaluate the tracking quality. If a hit position of the tracking plane is largely deviated from the predicted position by the track, it is regarded as an outlier and removed from tracking. The number of outliers is required to be less than 7 to select good quality tracks.

3.2.4 Decay in flight

The lifetime of the charged kaon is $c\tau = 3.7114$ m, and the typical 1-GeV/c kaon decays with the mean flight length $c\tau\beta\gamma = c\tau \times (1 \text{ GeV}/0.493677 \text{ GeV}) = 7.5$ m. Since the distance between the target and the TOF wall is about 4 m, some kaons decay before reaching the TOF wall. To reduce tracking errors due to these decays in flight, the hit position of TOF wall was checked whether it is consistent with the extrapolated position of the reconstructed track. If not consistent, the particle is considered to decay and change the direction of motion before reaching the TOF wall. Such events are rejected.

TOF-x consistency

The TOF slat, which was predicted to be fired by the tracking analysis, and the adjacent slats were checked whether they were actually fired or not. If none of them were fired, the event was removed. Note that the slat width, which determines the TOF-x resolution, is 120 mm.

TOF-y consistency

The TOF slat is 200-cm-long in the vertical direction as shown in Fig. 2.19, and the propagation length of the scintillation light between the particle hit position and the PMT depends on the y-coordinate of the track. Therefore, the y position of the fired TOF slat can be obtained using

the time difference between the top and bottom PMTs. Let y_{trk} be an extrapolated y position by the tracking analysis, and y_{TOF} be a measured y position by the TOF slat. $|y_{\text{trk}} - y_{\text{TOF}}| < 80$ mm (3.6σ) cut was applied to remove the decay-in-flight events.

3.2.5 Tagger analysis

The position of the recoil electron was reconstructed using the tagging counter to determine the BCS photon energy E_γ. The fired fibers of TAG-SF were clustered and the center of the cluster was used as a reconstructed position of the recoil electron. When more than one track were reconstructed, the hit timing for each track was checked to choose the track corresponding to the BCS photon which generated the trigger. If two reconstructed tracks both satisfied the timing selection cut, the event was removed. The reconstruction efficiency (or the tagger analysis efficiency) $\eta_{\text{tag.ana.}}$ which is the survival ratio of the tagger analysis was determined in the following way. First, high momentum (> 2.0 GeV/c) proton sample was selected using LEPS spectrometer to remove events in which the low energy photon ($E_\gamma < 1.5$ GeV) generated the trigger. Note that the low energy photon was injected into the target, but its energy cannot be determined using the tagging system due to the mechanical reason (see 2.1.3). Next, the number of events which pass the tagger analysis was divided by the sample size. The efficiency was determined to be $\eta_{\text{tag.ana.}} = 0.969$.

Photon energy determination

The correspondence between the reconstructed position and E_γ was determined so that the Λ peak of the missing mass distribution from the $\gamma p \to K^+ X$ reaction [$MM(\gamma, K^+)$] comes to the nominal value $m_\Lambda = 1.115683$ GeV/c^2. Figure 3.6 shows the $MM(\gamma, K^+)$ distribution. The Λ and Σ^0 peaks are seen on the background due to K^+/π^+ misidentification.

The background distribution (green dashed histogram) is calculated in the following manner.

1. Prepare π^+ and K^+ samples.
2. Apply the $MM(\gamma, K^+) < 1.0$ GeV/c^2 cut to both samples[2]. Note that the updated K^+ sample contains only π^+s which are misidentified as K^+s since the missing mass of the K^+ cannot be smaller than the Λ mass (Fig. 3.6).
3. Divide the samples into several momentum bins.
4. Calculate the ratio $\#K^+/\#\pi^+$ (K^+/π^+ misidentification rate) for each bin[3].
5. Calculate $MM(\gamma, K^+)$ for each event in the π^+ sample before applying the $MM(\gamma, K^+) < 1.0$ GeV/c^2 cut, using the momentum-dependent K^+/π^+ misidentification rate as a weighting factor.

The misidentification rate is determined by the tracking devices and TOF wall, and we calculated the rate as a function of the momentum. Figure 3.7 shows the momentum dependence of the misidentification rate.

[2] As for π^+ sample, calculate $MM(\gamma, K^+)$ assuming the particle is K^+, i.e. use the kaon mass.

[3] Since the π^+ sample is dominated by the real π^+, this ratio can be regarded as the probability that the real π^+ is classified as a K^+.

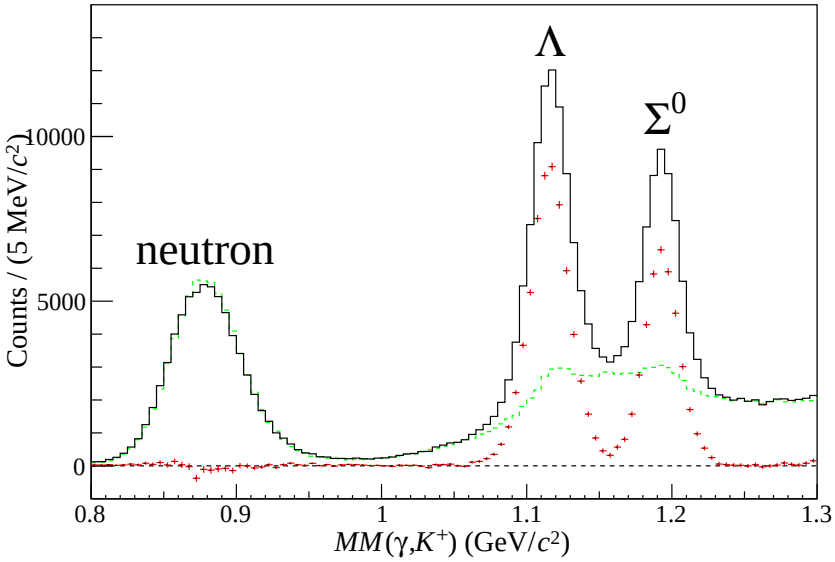

Fig. 3.6: $MM(\gamma, K^+)$ distribution (black). The peak structure around 0.88 GeV$/c^2$ comes from $\gamma p \to \pi^+ n$ reaction in which π^+ is misidentified as K^+. The green dashed histogram represents the background due to K^+/π^+ misidentification. The red histogram represents the background subtracted $MM(\gamma, K^+)$ distribution.

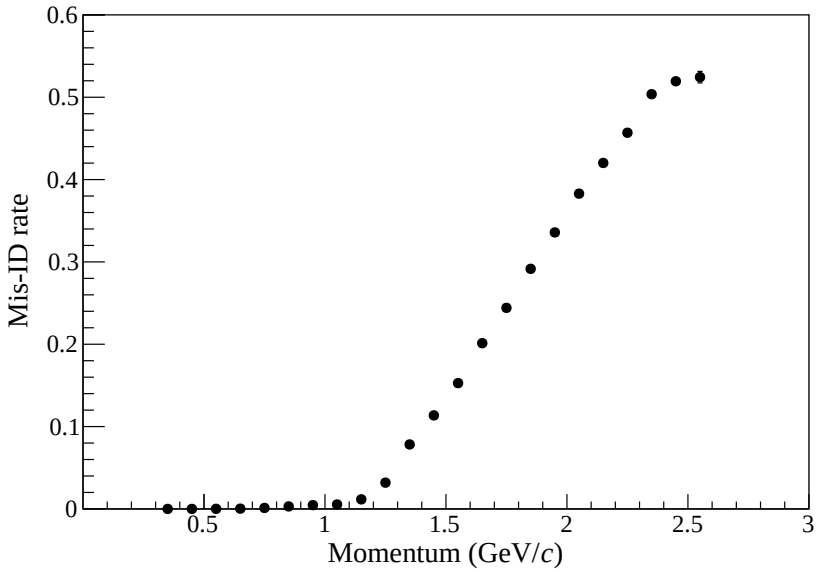

Fig. 3.7: Momentum dependence of the K^+/π^+ misidentification rate.

Then, we obtained the background subtracted $MM(\gamma, K^+)$ distribution as shown in Fig. 3.6, which can be used to determine the TAG-SF channel-E_γ correspondence.

Assuming the $\gamma p \to K^+\Lambda$ reaction, the photon energy can be predicted using the reconstructed variables obtained without the tagging system as follows:

$$E_\gamma^{\text{pred.}} = \frac{m_\Lambda^2 - m_p^2 - m_K^2 + 2m_p E_K}{2\left(m_p - E_K + p_K^z\right)}, \tag{3.11}$$

where m_X represents the mass of the particle X ($X = \Lambda, p, K$), E_K is the total energy of K^+, and p_K^z is the z-component of the K^+ momentum. Figure 3.8 shows the predicted energy $E_\gamma^{\text{pred.}}$ vs TAG-SFF (TAG-SFB) channel.

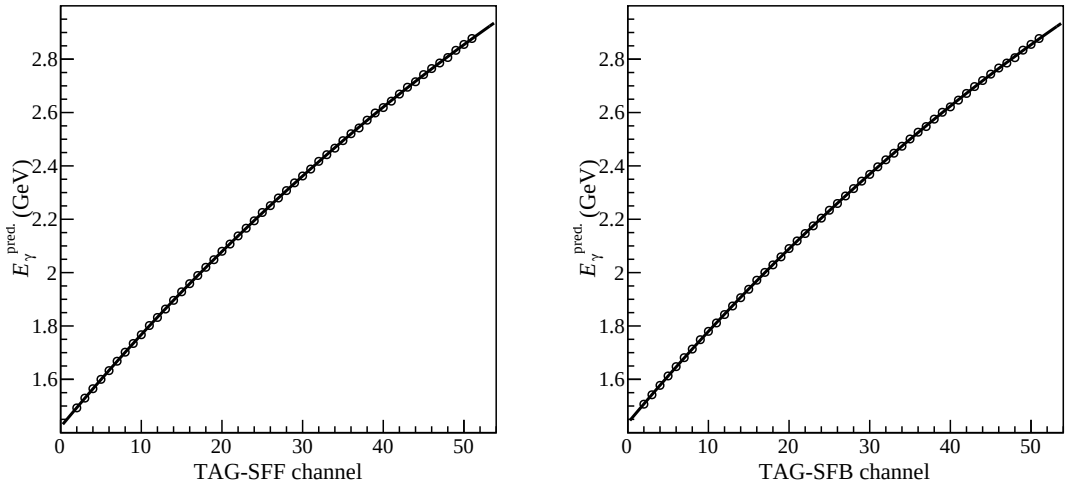

Fig. 3.8: $E_\gamma^{\text{pred.}}$ vs TAG-SFF (TAG-SFB) channel. The solid curves represent the fitting results (spline functions of degree 2 with one knot). See text for details.

The data points are fitted to by a spline function of degree 2 with one knot. The function is of class C^1 and has five free parameters. Using these functions, the reconstructed hit position was converted to the photon energy E_γ.

Missing mass [$MM(\gamma, K^+K^-)$] analysis

To select $\gamma p \to K^+K^-p$ events, a missing mass distribution for $p(\gamma, K^+K^-)X$ reaction [$MM(\gamma, K^+K^-)$] was used. Figure 3.9 shows the $MM(\gamma, K^+K^-)$ distribution. A clear proton peak is seen. In higher mass region at around 1.2 GeV/c^2, events with additional pions (for example, $\gamma p \to \pi KKN$ reactions) are seen. These background events were removed by applying $0.85 < MM(\gamma, K^+K^-) < 1.00$ GeV/c^2 cut, and $\gamma p \to K^+K^-p$ reactions were cleanly selected.

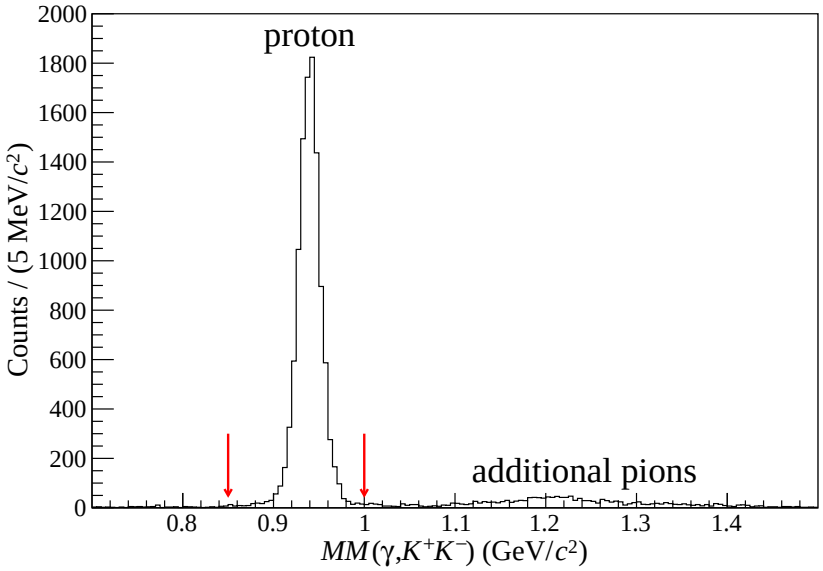

Fig. 3.9: Missing mass distribution for the $p(\gamma, K^+K^-)X$ reaction. The red arrows indicate the cut points.

3.2.6 Cut-flow summary

The applied cuts are summarized as follows.

Kaon identification	
K^+K^- PID	4σ PID boundary
Vertexing	
LH_2 target selection	Vertex-$z \in [-1100, -910]$ mm for 2015 data
	Vertex-$z \in [-1060, -863]$ mm for 2007 data
Vertex-x, y cut	$\lvert$Vertex-$x\rvert < 30$ mm $\wedge$ $\lvert$Vertex-$y\rvert < 30$ mm
Good track selection	
$P(\chi^2; n)$ of the tracking	$P(\chi^2; n) > 0.02$
#outliers cut	#outliers< 7
Decay in flight	
TOF x-consistency	Predicted TOF slat or the adjacent slats was fired.
TOF y-consistency	$\lvert y_{\text{trk}} - y_{\text{TOF}}\rvert < 80$ mm
Tagger analysis	
Track reconstruction	One on-timing track was reconstructed.
Missing mass cut	$0.85 < MM(\gamma, K^+K^-) < 1.00$ GeV/c^2

3.3 Monte Carlo Simulation

For the Monte Carlo (MC) simulation, the LEPS Collaboration has developed `g3leps` software. The MC simulation is used for the following two purposes. One is to calculate the acceptance of the LEPS spectrometer including detector efficiencies and resolutions, and the

other is to estimate background. The $\gamma p \to K^+K^-p$ events are cleanly selected as already shown in Figs 3.3 and 3.9, therefore for the background estimation, we simulated the detector response to the following three reactions which share the K^+K^-p final state.

$$\gamma p \to \phi p \to K^+K^-p \tag{3.12}$$
$$\gamma p \to K^+\Lambda(1520) \to K^+K^-p \tag{3.13}$$
$$\gamma p \to K^+K^-p \quad \text{(nonresonant)} \tag{3.14}$$

For the ϕ meson generation, the t-slope factor B and SDMEs are input to the MC code. These input parameters are iteratively determined. $K^+\Lambda(1520)$ events are generated isotropically in the overall center-of-mass frame. The subsequent $\Lambda(1520) \to K^-p$ decay is also simulated in the isotropic way in the $\Lambda(1520)$-rest frame. The nonresonant K^+K^-p events are uniformly generated in the phase space.

To simulate the detector response, efficiencies and resolutions of each detector are input to the MC codes, in addition to set geometries of detectors and materials in the LEPS spectrometer. The `g3leps` is based on the `GEANT` 3.21 which was developed by CERN [65]. The `GEANT` libraries simulate behaviors of the produced particles, taking account of decays in flight and multiple Coulomb scatterings. Hadronic interactions are simulated with `GHEISHA` package. Generated MC data is analyzed in the exactly same way as the real data analysis by the `LEPSana`.

3.4 Yield Calculation

The yield $Y_{\phi\to K^+K^-}$ [Eq. (3.1)] is calculated using the K^+K^- invariant mass distribution $M(K^+K^-)$ after the event selection cuts, which is shown in Fig. 3.10.

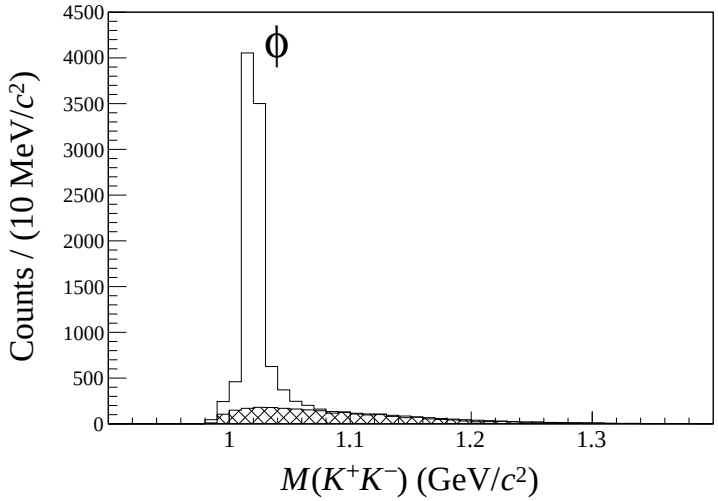

Fig. 3.10: The K^+K^- invariant mass distribution $M(K^+K^-)$. The hatched histogram is the background distribution obtained by the MC simulation which is described in this section.

A peak corresponding to the ϕ meson is seen on top of the background. In this section, we describe how the background distribution (hatched histogram) is evaluated and how the yield is calculated.

3.4.1 Background Subtraction

As described in section 3.3, we considered the two sources of background: $\gamma p \to K^+\Lambda(1520)$ reaction and nonresonant K^+K^-p production. The background level was estimated by the simultaneous fit of the K^+K^- invariant mass $M(K^+K^-)$ and K^-p invariant mass $M(K^-p)$ distributions, using the MC mass distributions of ϕp, $K^+\Lambda(1520)$, and nonresonant K^+K^-p reactions. MC mass distributions were obtained by applying the exactly same cut conditions as were applied to the real data. Figure 3.11 shows the $M(K^-p)$ vs $M(K^+K^-)$ scatter plots of real data, MC ϕ, MC $\Lambda(1520)$, and MC nonresonant K^+K^-p data, for certain four kinematic bins.

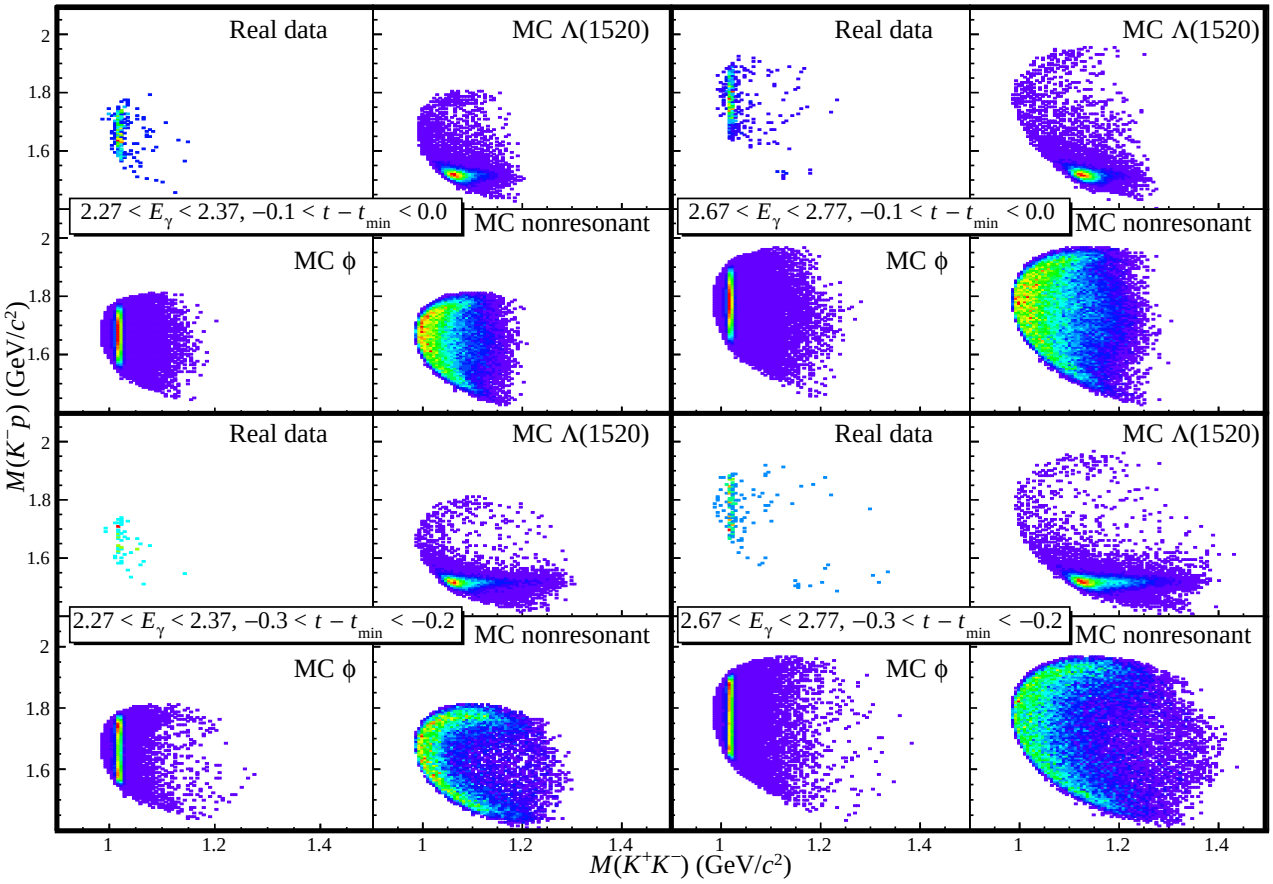

Fig. 3.11: $M(K^-p)$ vs $M(K^+K^-)$ scatter plots of real and MC data for several kinematic bins.

As for $\Lambda(1520)$ production, the $\Lambda(1520)$ events overlap the ϕ events only at low energies (see the left-side figures). As shown in the right-side figures, few $\Lambda(1520)$ events are contaminated in the ϕ mass region $1.005 < M(K^+K^-) < 1.035$ GeV/c^2. Needless to say, nonresonant events overlap the ϕ events at every kinematic bin.

Figure 3.12 shows the fitting results for $2.67 < E_\gamma < 2.77$ GeV bin. The fitting results for the other bins are shown in Appendix A.

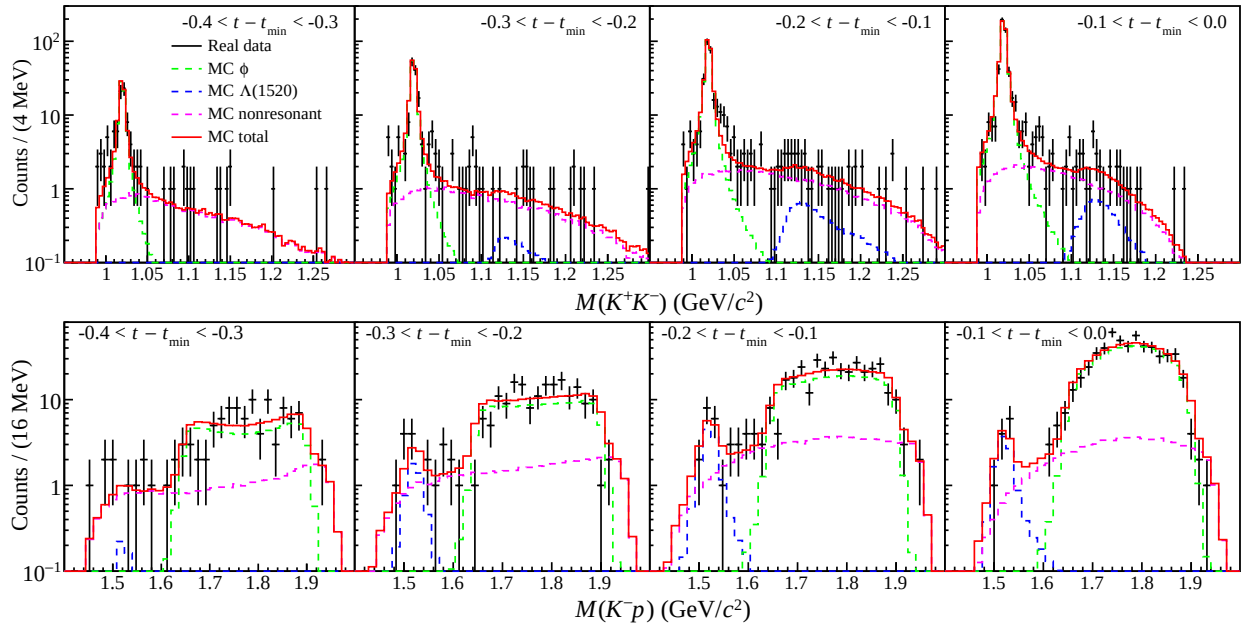

Fig. 3.12: $M(K^+K^-)$ and $M(K^-p)$ distributions for $2.67 < E_\gamma < 2.77$ GeV bin in 2015.

3.4.2 $\phi \to K^+K^-$ yield calculation for cross section

E_γ and t bins for the cross section calculation are listed up in Table 3.2.

Table 3.2: Binning for the cross section extraction.

E_γ bin (GeV)	E_γ bin width (GeV)	t bin (GeV^2)	t bin width (GeV^2)
$[1.67, 1.87]$	0.2	$t_{\text{min}} + [-0.1, 0.0]$	0.1
$[1.87, 2.07]$	0.2	$t_{\text{min}} + [-0.2, -0.1]$	0.1
$[2.07, 2.27]$	0.2	$t_{\text{min}} + [-0.3, -0.2]$	0.1
$[2.27, 2.37]$	0.1	$t_{\text{min}} + [-0.4, -0.3]$	0.1
$[2.37, 2.47]$	0.1	$t_{\text{min}} + [-0.5, -0.4]$	0.1
$[2.47, 2.57]$	0.1	$t_{\text{min}} + [-0.6, -0.5]$	0.1
$[2.57, 2.67]$	0.1		
$[2.67, 2.77]$	0.1		
$[2.77, 2.87]$	0.1		

For each bin, the ϕ-meson yields are obtained by integrating the background [$\Lambda(1520)$ + non-resonant K^+K^-p] subtracted $M(K^+K^-)$ distributions from 1.005 to 1.035 GeV/c^2. The difference between the obtained ϕ-meson yield and the integral of the MC ϕ distribution from 1.005 to 1.035 GeV/c^2 is treated as the systematic uncertainty.

The obtained ϕ-meson yields are shown in Fig. 3.13.

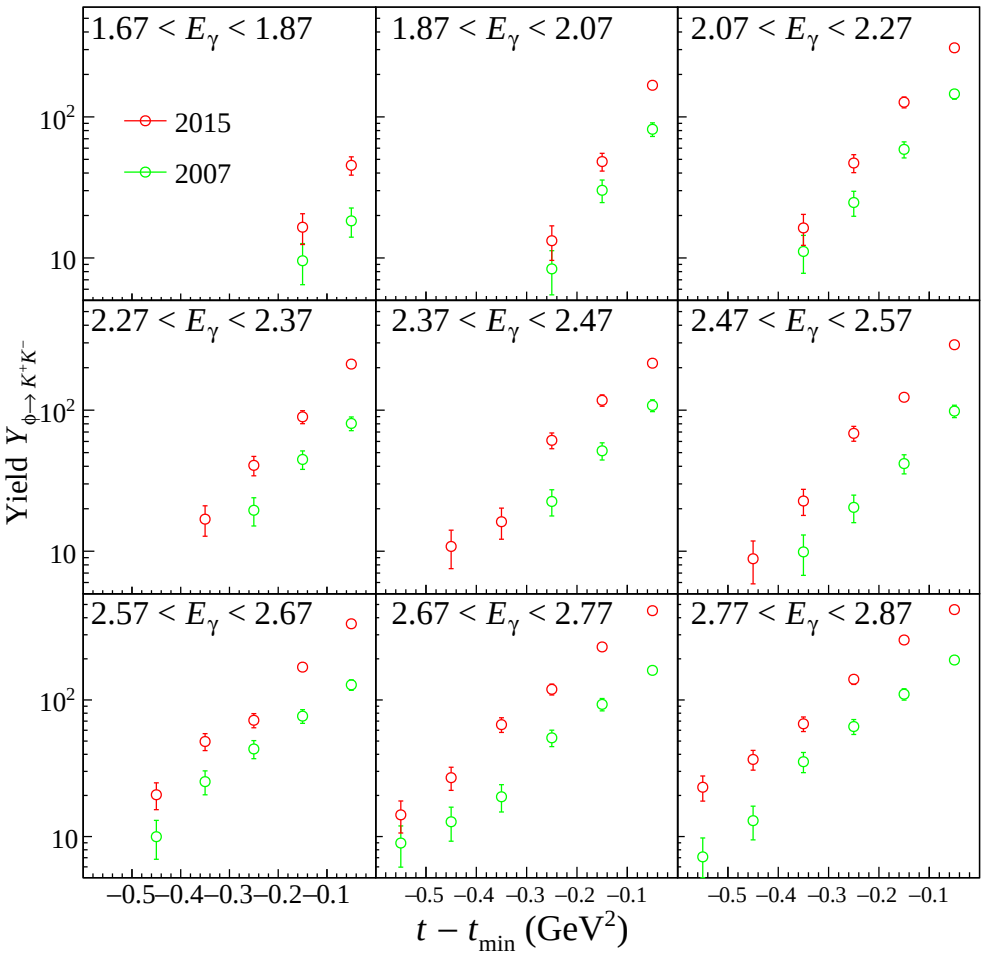

Fig. 3.13: t dependence of the ϕ-meson yields $Y_{\phi\to K^+K^-}$ (before acceptance correction) for each E_γ bin.

3.4.3 Yield calculation for angular distribution

To obtain the angular distributions for each data set (see Table 2.4), the angles are divided into 12 bins, and for each angle bin, ϕ-meson yields are calculated in the same way as described in section 3.4.2. The obtained yields are shown in Fig. 3.14 and Fig. 3.15. To extract the energy dependences of the SDMEs in the forward angle, t range is set to $t - t_{\min} > -0.05$ GeV^2, and the selected forward events were divided into 3 energy bins from 2.17 to 2.77 GeV (Fig. 3.14). On the other hand, to extract the t dependences of the SDMEs, E_γ range was set to $2.37 < E_\gamma < 2.77$ GeV, and the data were divided into four angular bins from -0.2 GeV^2 to 0.0 GeV in $t - t_{\min}$ (Fig. 3.15).

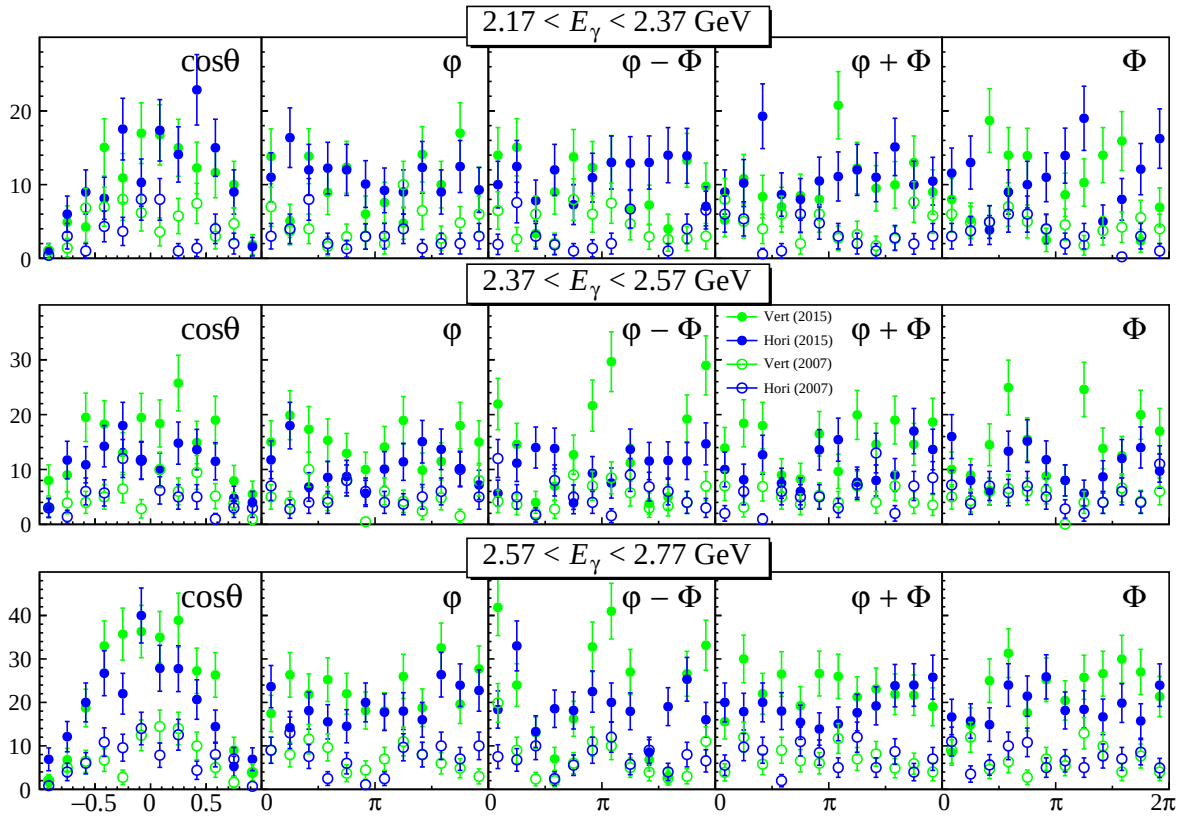

Fig. 3.14: Angle dependences of ϕ-meson yields $Y_{\phi\to K^+K^-}$ (before acceptance correction) for $t - t_{\text{min}} > -0.05$ GeV^2.

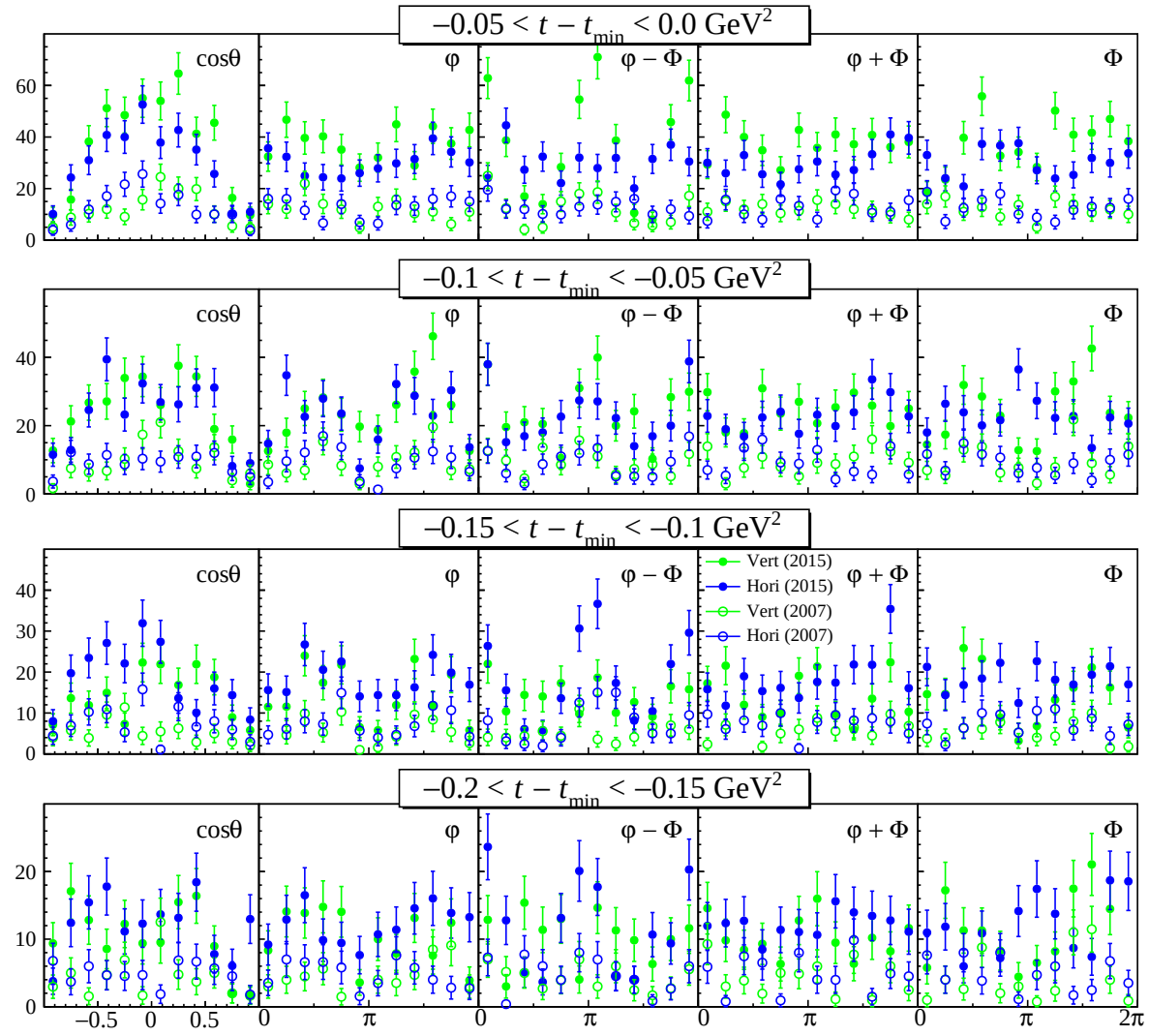

Fig. 3.15: Angle dependences of ϕ-meson yields $Y_{\phi\to K^+K^-}$ (before acceptance correction) for $2.37 < E_\gamma < 2.77$ GeV.

3.5 Acceptance of the LEPS Spectrometer

To convert the yield $Y_{\phi\to K^+K^-}$ to the number of generated ϕ mesons N_ϕ, the acceptance of the LEPS spectrometer A is necessary [see Eq. (3.1)].

3.5.1 How to get the acceptance A

The acceptance of the LEPS spectrometer was calculated using the MC simulation. It is calculated by dividing the number of accepted events by the number of generated events. Here, the "accepted events" means the events which survive all the cuts applied in the real data analysis. When calculating the cross section, we get the acceptance as a function of E_γ and 4-momentum transfer t. On the other hand, when extracting the SDME, the acceptance is calculated as a function of E_γ, t, and the angle which corresponds to the SDME extraction (see subsection

1.2.2). The acceptance is determined by the detector geometries, efficiencies, and resolutions, in addition to the analysis cut criteria. These detector parameters were input to the MC code.

The properties of the ϕ-meson photoproduction should be input into the MC code to reproduce the ϕ-meson events. Because we divide the E_γ range into bins, the E_γ-dependence of the cross section is not necessary to calculate acceptances, assuming that the E_γ-dependence is small in each bin. This assumption cannot be applied to the t-dependence. Since the ϕ-meson photoproduction shows the steep forward peaking structure (see the top middle of Fig. 3.16), the t-dependence in each t-bin is not negligible. Therefore, we used the t-slope factor B to generate the MC ϕ events. Here, the t-slope factor B is just what we want to derive, then it is iteratively determined. Also, SDMEs are necessary to reproduce the decay angular distribution of the ϕ meson. They are also iteratively determined and input into the MC code. As a starting point for the iteration, following three sets of SDMEs are used:

Isotropic decay $\rho^0_{00} = 1/3$
$\mathrm{Re}\rho^0_{10} = \rho^0_{1-1} = \rho^1_{11} = \rho^1_{00} = \mathrm{Re}\rho^1_{10} = \rho^1_{1-1} = \mathrm{Im}\rho^2_{10} = \mathrm{Im}\rho^2_{1-1} = 0$

2005 LEPS results $\rho^0_{00} = 0.069,\ \rho^0_{1-1} = 0.039,\ \rho^1_{1-1} = -\mathrm{Im}\rho^2_{1-1} = 0.189$
$\mathrm{Re}\rho^0_{10} = \rho^1_{11} = \rho^1_{00} = \mathrm{Re}\rho^1_{10} = \mathrm{Im}\rho^2_{10} = 0$

Zero SDMEs $\rho^0_{00} = \mathrm{Re}\rho^0_{10} = \rho^0_{1-1} = \rho^1_{11} = \rho^1_{00} = \mathrm{Re}\rho^1_{10} = \rho^1_{1-1} = \mathrm{Im}\rho^2_{10} = \mathrm{Im}\rho^2_{1-1} = 0.$

The second one comes from the results of $2.17 < E_\gamma < 2.37$ GeV and $t - t_{\mathrm{min}} > -0.2$ GeV^2 [10]. Note that all the SDMEs cannot be zero at once, and the "zero SDMEs" in the third one means that SDMEs in Eqs. (1.29,1.30,1.31) are all zero[4]. We confirmed that the SDMEs converge to the same results by iterating about 3 times, regardless of which one of the three sets we choose.

To check that the detector behavior is appropriately reproduced, distributions of the kinematic variables are compared between real and MC data. Figure 3.16 shows the comparisons of typical variables, and the data is well reproduced by the MC simulation.

[4]For example, $\rho^0_{11} = 1/2$ in the "zero SDMEs" set.

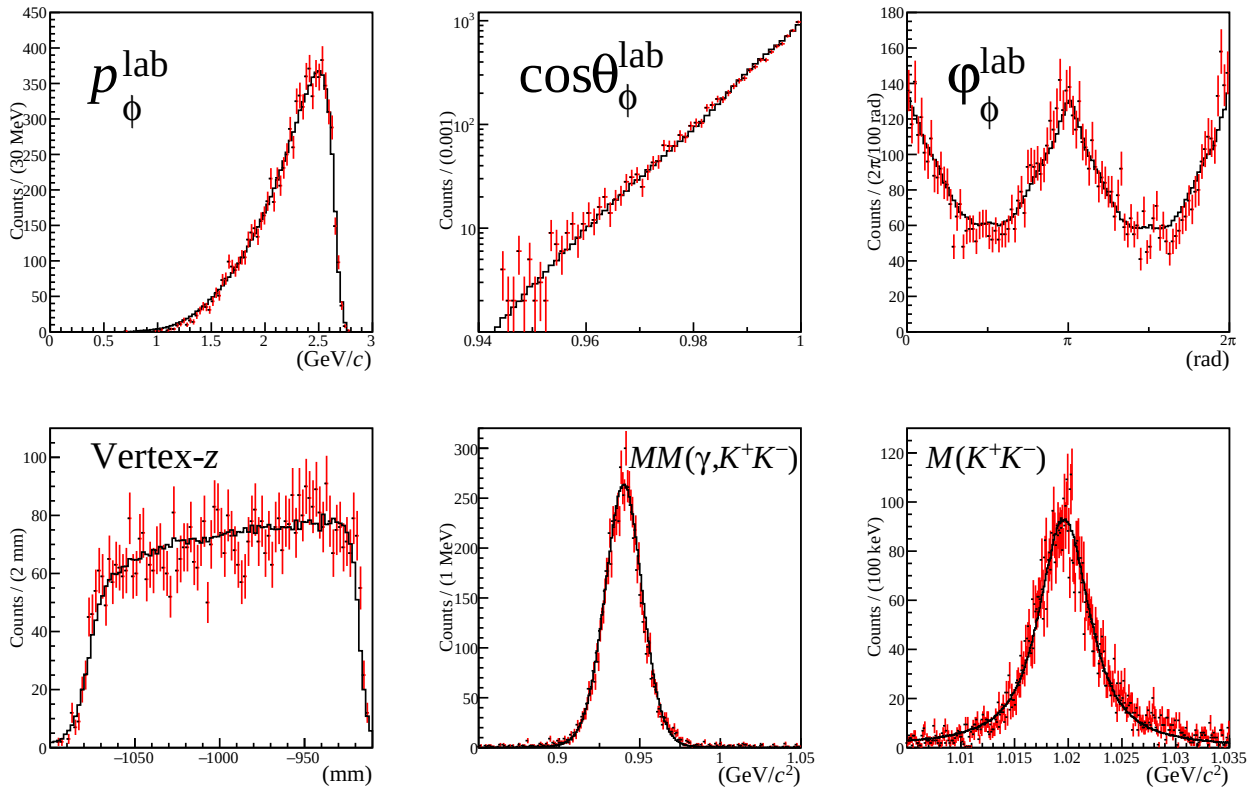

Fig. 3.16: Comparison between real data (red histograms) and MC results (black histograms). Top left: 3-momentum magnitude of ϕ mesons in the laboratory frame. Top middle: Polar angle distribution of ϕ mesons in the laboratory frame. Top right: Azimuthal angle distribution of ϕ mesons in the laboratory frame. Bottom left: Vertex-z distribution of ϕ mesons. Bottom middle: Missing mass distribution $MM(\gamma, K^+K^-)$. Bottom right: K^+K^- invariant mass distribution $M(K^+K^-)$ after the background subtraction.

3.5.2 Acceptance as a function of E_γ and t

For the cross section measurements, the acceptance of the LEPS spectrometer is calculated for each bin in Table 3.2. Figure 3.17 shows t dependences of the acceptance A for each E_γ bin. 2015 and 2007 results are slightly different, mainly because the target position for 2007 data is about 5 cm downstream than that for 2015 data.

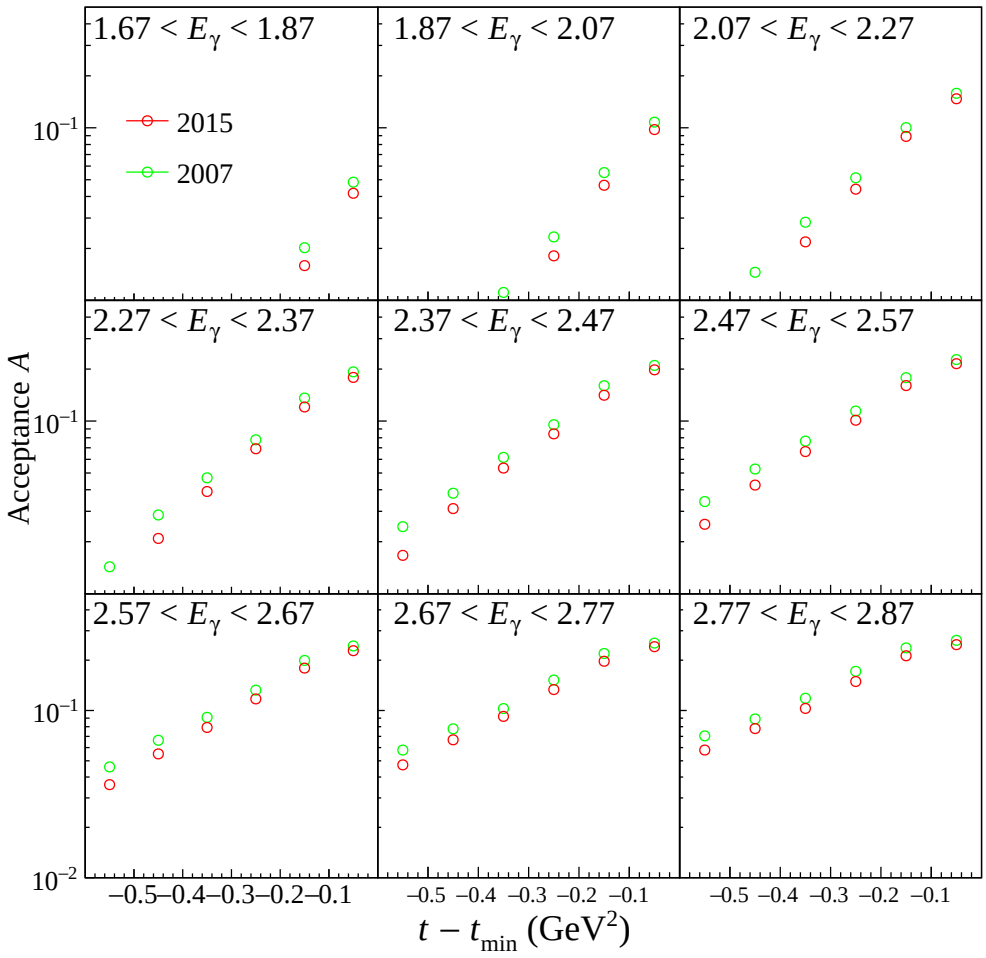

Fig. 3.17: t dependence of the acceptance A of the LEPS spectrometer for each E_γ bin.

3.5.3 Acceptance as a function of E_γ, t, and K^+ angle

The acceptances for the SDME measurements are calculated in the same way as those for the cross section measurements. Note that the SDMEs are iteratively input to the MC simulation codes. The results are shown in Fig. 3.18 and Fig. 3.19.

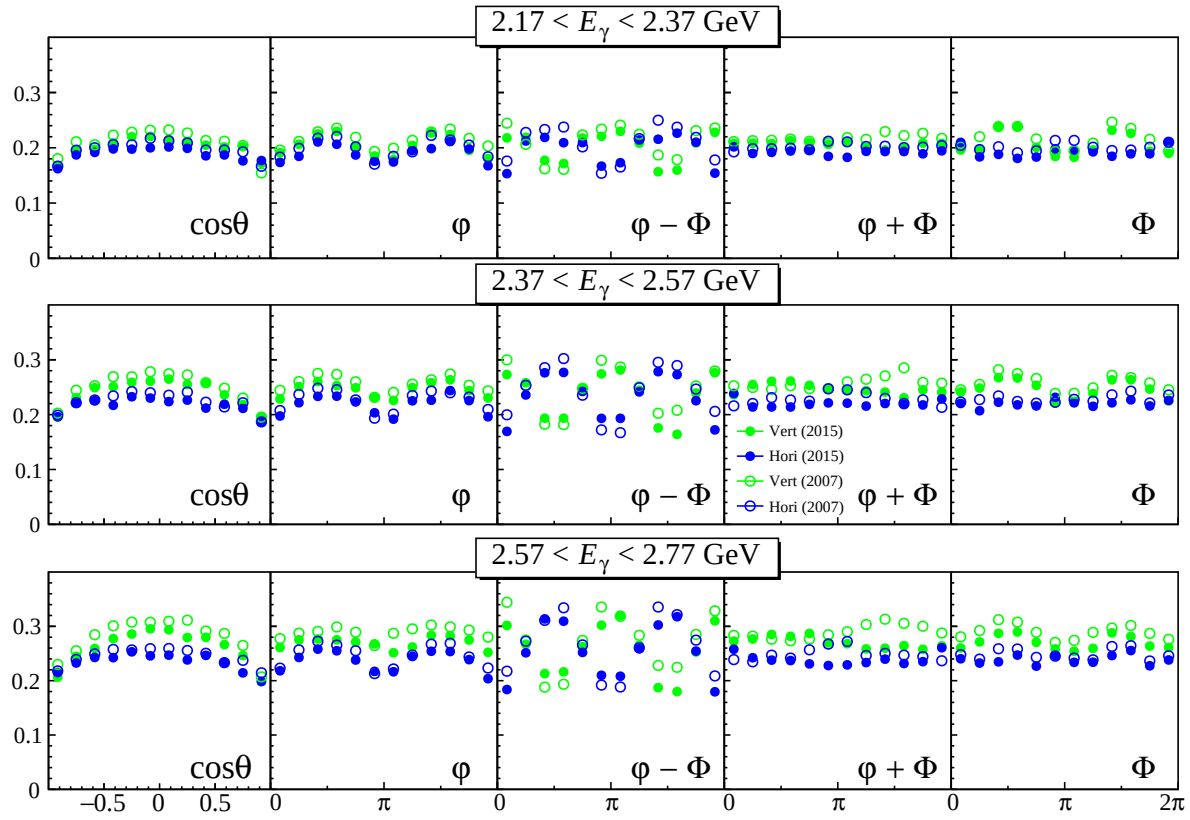

Fig. 3.18: Angle dependences of the acceptances for $t - t_{\text{min}} > -0.05$ GeV^2.

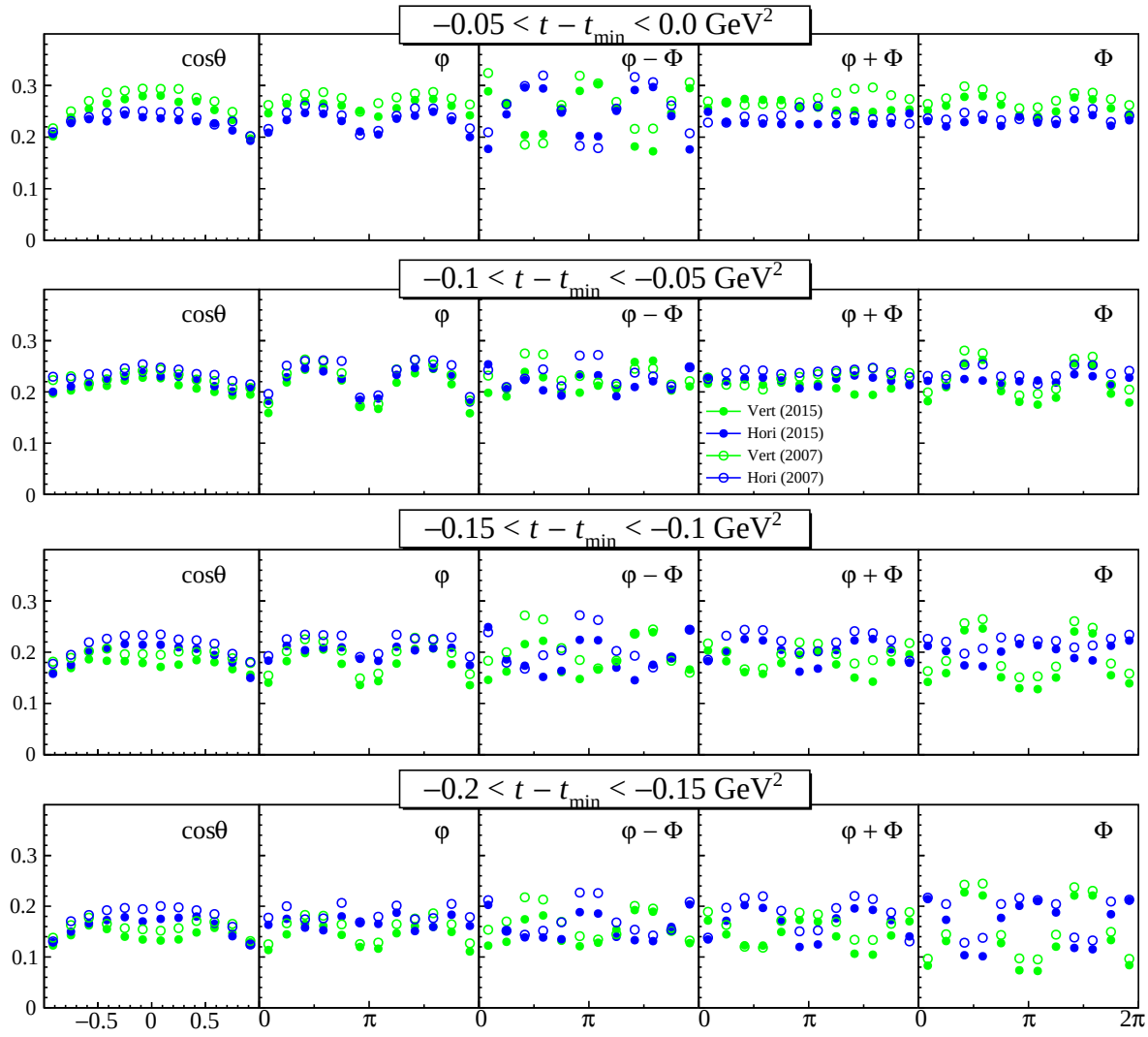

Fig. 3.19: Angle dependences of the acceptances for $2.37 < E_\gamma < 2.77$ GeV.

3.6 Number of Photons and Target Protons and Photon Polarization

3.6.1 Number of photons N_γ

To extract the cross section, the number of photons for each E_γ bin is necessary. The tagger count was converted to the total number of photons on the target in the tagged energy range, by multiplying the live-time correction factor for the tagger scaler and the transmission factor 0.526. Next, the total number of photons was distributed to each E_γ bin, using the Compton spectrum (see Fig. 2.3). In other words, the photon fraction of the E_γ bin ω_γ in Eq. (3.1) is calculated as the ratio of area of the E_γ bin in the Compton spectrum to that of the tagged energy range. Results for six E_γ-bins from 2.27 to 2.87 GeV for 2015 data are shown in Fig. 3.20.

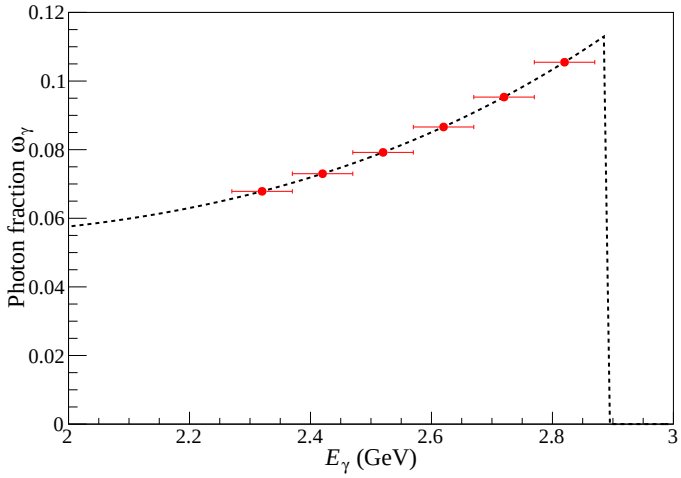

Fig. 3.20: Photon fractions ω_γ for 2015 data. The red solid circles represent the photon fractions for each E_γ bin. The Compton spectrum, whose integral is normalized to 0.1 GeV (E_γ-bin width), is overlaid (black dashed curve).

The photon fractions for all bins used in this work are summarized in Table 3.3.

Table 3.3: Photon fractions ω_γ for each bin.

E_γ-bin (GeV)	ω_γ for 2007 data	ω_γ for 2015 data
$[1.67, 1.87]$	0.1058	0.1100
$[1.87, 2.07]$	0.1088	0.1142
$[2.07, 2.27]$	0.1168	0.1241
$[2.27, 2.37]$	0.0632	0.0679
$[2.37, 2.47]$	0.0676	0.0730
$[2.47, 2.57]$	0.0729	0.0792
$[2.57, 2.67]$	0.0793	0.0866
$[2.67, 2.77]$	0.0869	0.0953
$[2.77, 2.87]$	0.0958	0.1055

3.6.2 Number of target protons per unit area N_{target}

As shown in Fig. 3.21, the effective target length is estimated to be $16.55(7)$ cm, by fitting the edges of the vertex distribution with error functions. This length corresponds to $N_{\text{target}} = 7.04 \times 10^{-7}\ \mu\text{b}^{-1}$.

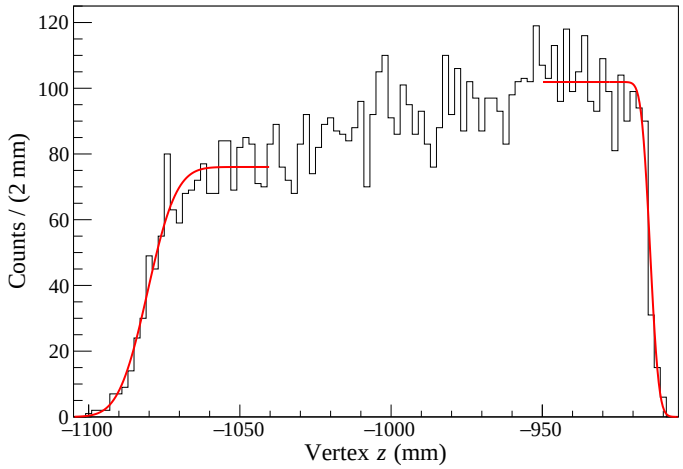

Fig. 3.21: The determination of the effective target length.

3.6.3 Validity checks

To check the data quality and to confirm the validity of the analysis methods, several observables are compared with previous measurements as described below.

Kp detection mode

In addition to the K^+K^- detection mode, the Kp detection mode can be used to study the $\gamma p \to \phi p$ reaction. In the Kp detection mode, one kaon and proton are detected with the LEPS spectrometer, and the missing kaon is identified using the missing-mass technique. The acceptance for the Kp mode drops rapidly with increasing E_γ, as shown in Fig. 3.22, because the ϕp opening angle becomes large when the energy E_γ increases.

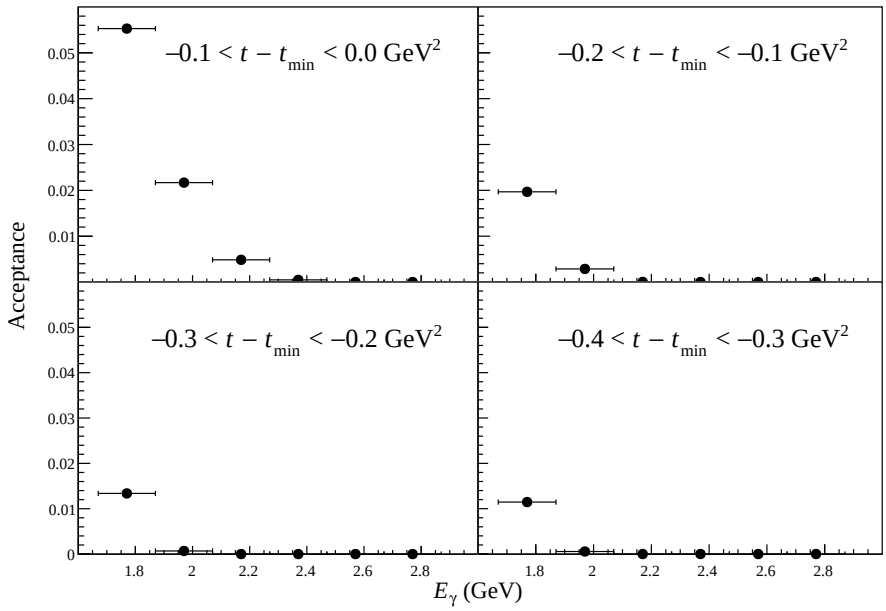

Fig. 3.22: E_γ dependences of the acceptances for K^-p mode (2015).

In the K^-p mode, the ϕ events exist below $E_\gamma = 2.1$ GeV as shown in Fig. 3.23.

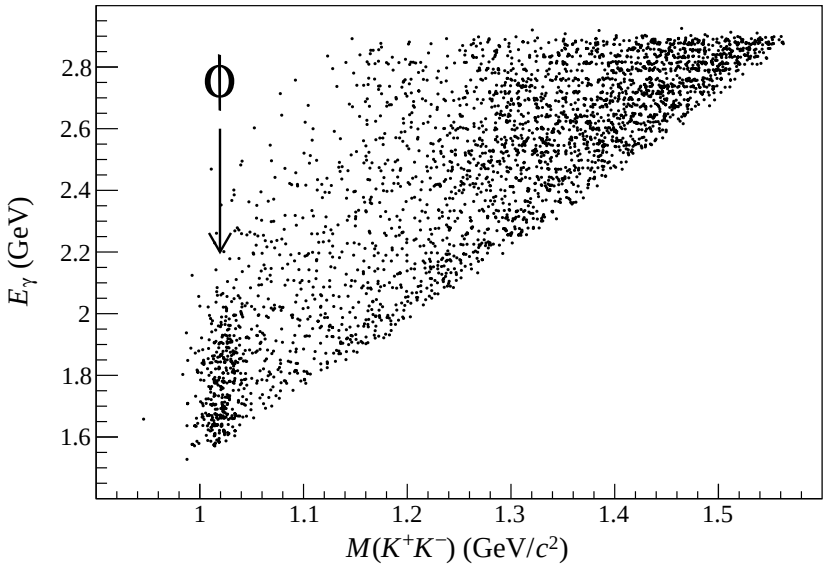

Fig. 3.23: E_γ vs $M(K^+K^-)$ for K^-p detection mode.

Therefore, we used the Kp mode just for the validity check of the ϕ analysis, especially for the validity of the N_γ and N_{target} [Eq. (3.1)] for the cross section measurement. The results are shown in Fig. 3.24. They are consistent with LEPS 2005 results [10] and K^+K^- mode results of this work.

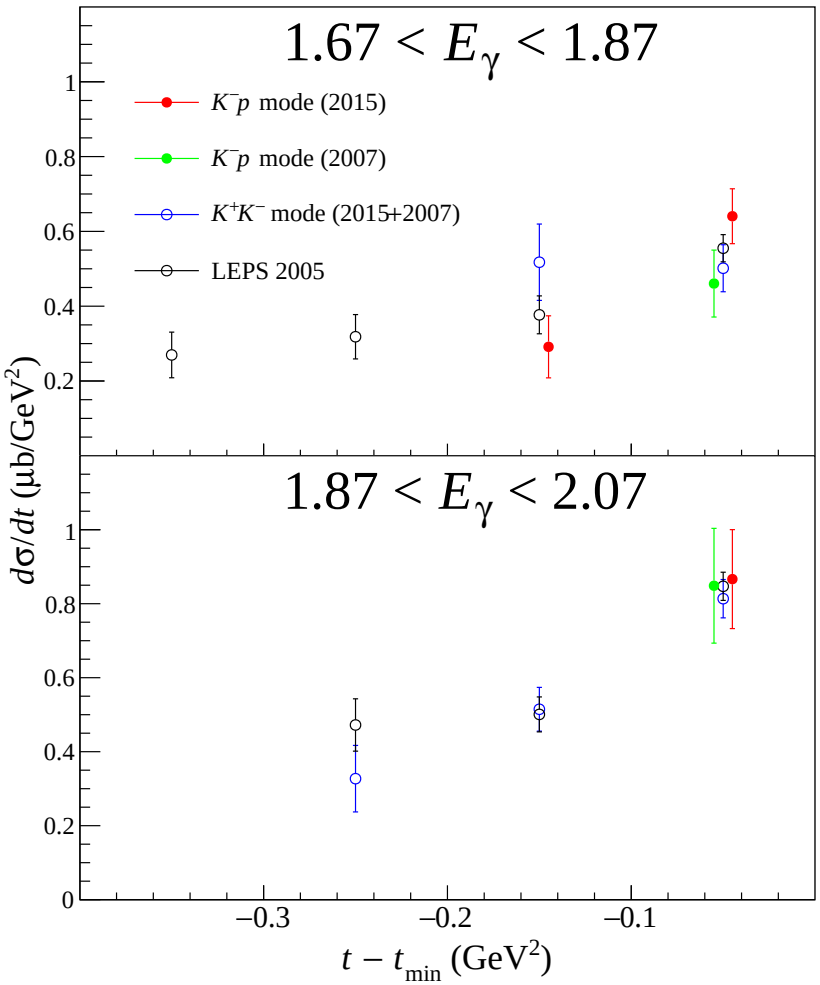

Fig. 3.24: $d\sigma/dt$ results. The red and green data points are shifted horizontally for clarity.

The uncertainty of the yield calculation for the K^+p mode is larger than that of the K^-p mode, due to the $\gamma p \to K^+Y$ channels. Therefore, we used only the K^-p mode for the validity check.

Cross sections for $\gamma p \to K^+Y$ channels

To confirm the validity of the number of photons N_γ and number of target protons per unit area N_{target}, we have also extracted the cross sections for the $\gamma p \to K^+Y$ ($Y = \Lambda, \Sigma^0$) reactions (see Fig. 3.6), and compared the results with LEPS 2006 results [66]. Figure 3.25 shows energy dependences of the Λ and Σ^0 production cross sections for each $\cos\theta_{\text{c.m.}}$ bin. The results are well consistent with LEPS 2006 results.

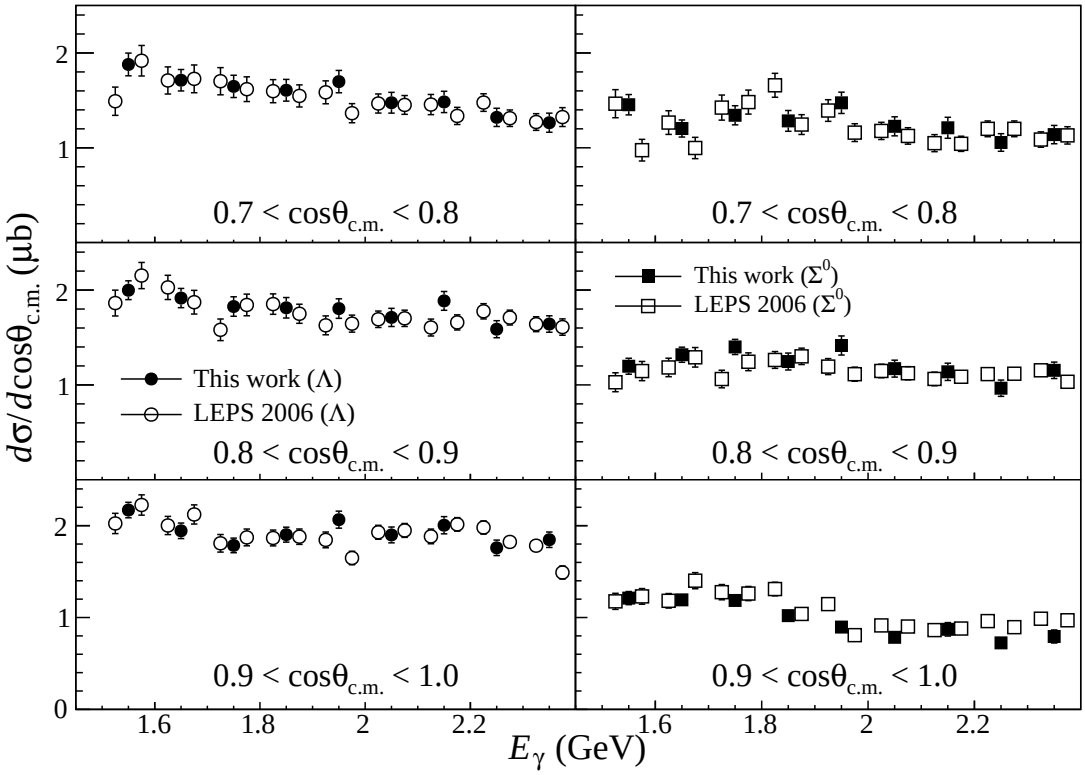

Fig. 3.25: Energy dependences of cross sections for the $\gamma p \to K^+\Lambda$ and $\gamma p \to K^+\Sigma^0$ reactions.

3.6.4 Photon polarization P_γ

The degree of linear polarization of the incident photon P_γ is necessary to extract some SDMEs ($\bar{\rho}^1_{1-1}$, Δ_{1-1}, $2\rho^1_{11} + \rho^1_{00}$). The polarization P_γ depends on E_γ as already shown in Fig. 2.3. For each E_γ-bin, the mean value of the polarization is calculated using the Compton spectrum to take into account the energy dependence in the E_γ bin. The formula is as follows:

$$P_\gamma = P_{\text{laser}} \times \frac{\int_{E_\gamma \text{ bin}} f(x)g(x)dx}{\int_{E_\gamma \text{ bin}} f(x)dx}, \tag{3.15}$$

where the function f represents the Compton spectrum (arbitrary unit), and the function g represents the polarization function shown in Fig. 2.3. For the laser polarization, $P_{\text{laser}} = 0.97$ is used, which is determined by the laser polarization measurements. Figure 3.26 shows results for $[2.17, 2.37]$, $[2.37, 2.57]$, and $[2.57, 2.77]$ GeV E_γ-bins.

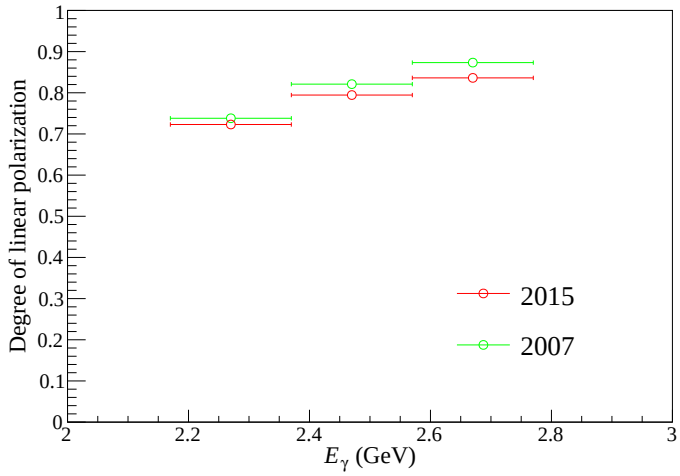

Fig. 3.26: Degree of linear polarization P_γ for each E_γ-bin.

The photon polarizations P_γ for all bins used in this work are summarized in Table 3.4.

Table 3.4: Photon polarizations P_γ for each bin.

E_γ-bin (GeV)	P_γ for 2007 data	P_γ for 2015 data
$[2.17, 2.37]$	0.7381	0.7230
$[2.37, 2.57]$	0.8210	0.7945
$[2.57, 2.77]$	0.8733	0.8362
$[2.37, 2.77]$	0.8493	0.8172

3.6.5 Validity checks using beam asymmetries for $\gamma p \to K^+ Y$ channels

The polarization of degree of the photon beam P_γ is used to determine some SDMEs such as $\bar{\rho}^1_{1-1}$. To confirm the validity of the obtained P_γ, we calculated the beam asymmetries Σ for the hyperon productions, and compared with the previous measurements. The definition of the beam asymmetry Σ is as follows:

$$\frac{d\sigma}{d\Omega} = \left(\frac{d\sigma}{d\Omega}\right)_{\text{unpol}} \left[1 - P_\gamma \Sigma \cos\left(2\varphi\right)\right], \tag{3.16}$$

where $(d\sigma/d\Omega)_{\text{unpol}}$ represents the differential cross section obtained by the unpolarized photon, and φ is the angle between the polarization vector of the incident photon and the production plane. Note that the beam asymmetry is the function of E_γ and the polar angle of the produced hyperon. Figure 3.27 shows the energy dependences of the beam asymmetries. Results of this work and LEPS 2006 results [66] are consistent within the statistical uncertainties.

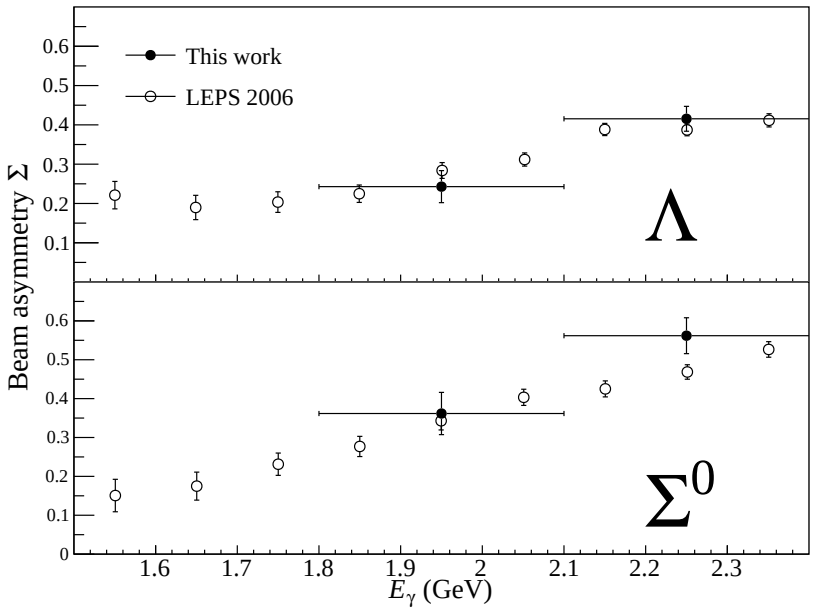

Fig. 3.27: Energy dependences of beam asymmetries. $\cos\theta^{K^+}_{\text{c.m.}} > 0.6$. The top figure is for the $\gamma p \to K^+\Lambda$ reaction, and the bottom figure is for the $\gamma p \to K^+\Sigma^0$ reaction. The open circles are taken from Ref. [66].

CHAPTER

FOUR

RESULTS

In this chapter, we show the differential cross sections $d\sigma/dt$ for the $\gamma p \to \phi p$ reaction in the energy range of $1.67 < E_\gamma < 2.87$ GeV and the t range of $-0.6 < t - t_{\rm min} < 0.0$ GeV^2. For each E_γ bin, the t-dependence of the differential cross sections is fitted with an exponential curve, and the t-slope factor B and $(d\sigma/dt)_{t=t_{\rm min}}$ are obtained. Then, the energy dependences of the t-slope factor B and $(d\sigma/dt)_{t=t_{\rm min}}$ are shown. Also, the SDMEs are shown using two types of the binning. One is for the energy dependence of the SDMEs at forward angles $t - t_{\rm min} > -0.05$ GeV^2 (the energy range $2.17 < E_\gamma < 2.77$ GeV is divided into 3 E_γ bins). The other is for the t dependence of the SDMEs with the wide E_γ bin $2.37 < E_\gamma < 2.77$ GeV. The t range $-0.5 < t - t_{\rm min} < 0.0$ GeV^2 is divided into 4 bins.

4.1 Differential Cross Section $d\sigma/dt$ and B, $(d\sigma/dt)_{t=t_{\rm min}}$ Parameters

Figure 4.1 shows the results of the differential cross sections. The binning is shown in Table 3.2. Since the acceptances for 2007 and 2015 are different (Fig. 3.17), the cross sections are obtained separately. For each E_γ bin, t-dependences show forward peaking structures, suggesting the dominance of t-channel processes.

We perform a χ^2 test to compare 2015 and 2007 results. From the χ^2/ndf, the significance $m\sigma$, which represents whether the deviation is statistically significant or not, is calculated to satisfy the following equation:

$$\int_{-\infty}^{\chi^2} f(x;n)dx = \frac{1}{\sqrt{2\pi}} \int_{-m}^{m} \exp\left(-\frac{x^2}{2}\right) dx, \tag{4.1}$$

where $f(x;n)$ represents the probability density function of the chi-square distribution with n degrees of freedom. The 2015 and 2007 results are consistent within statistical uncertainties as shown in Fig. 4.1 (in parentheses).

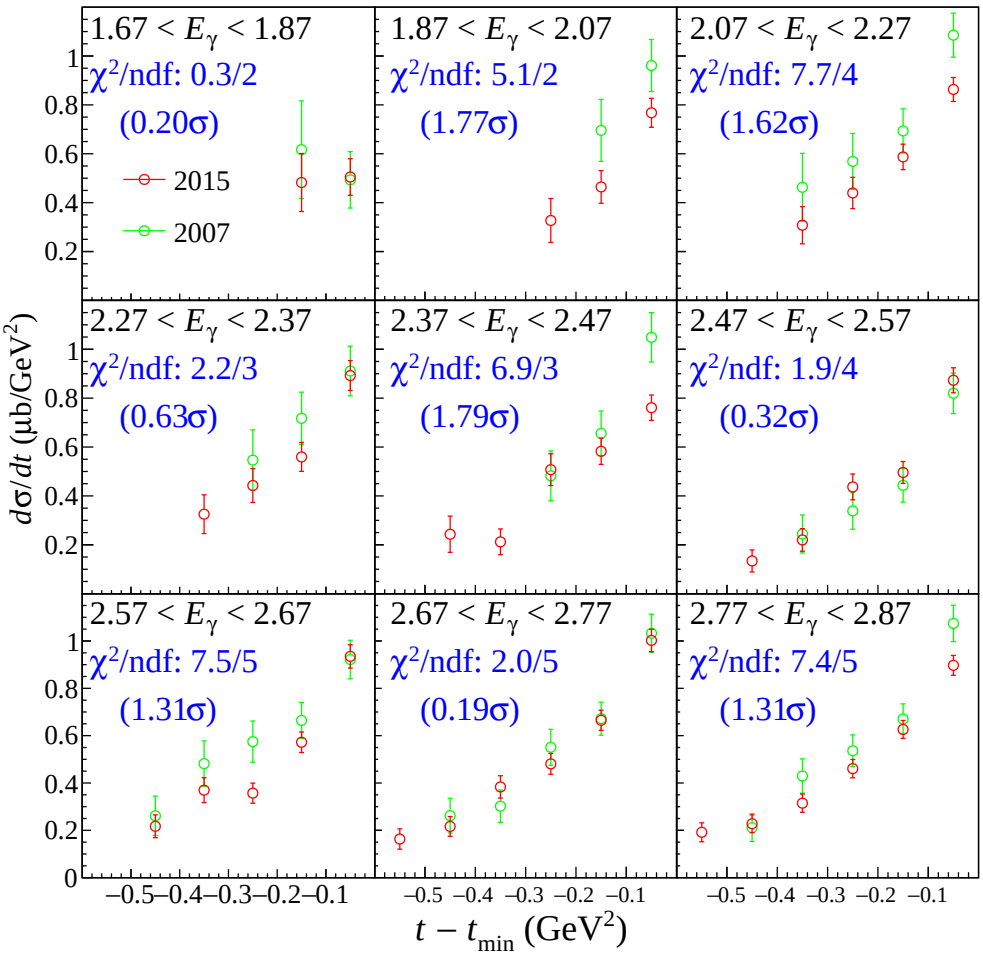

Fig. 4.1: t dependence of the differential cross sections $d\sigma/dt$ for each E_γ bin. 2015 and 2007 results are compared. See text for details.

The combined (2007+2015) cross sections $d\sigma/dt$ are extracted by calculating the weighted means. The results are shown in Fig. 4.2. The cross sections (2007+2015) for low E_γ region ($E_\gamma < 2.37$ GeV) are compared with the LEPS 2005 results [10], and found to be consistent within statistical errors.

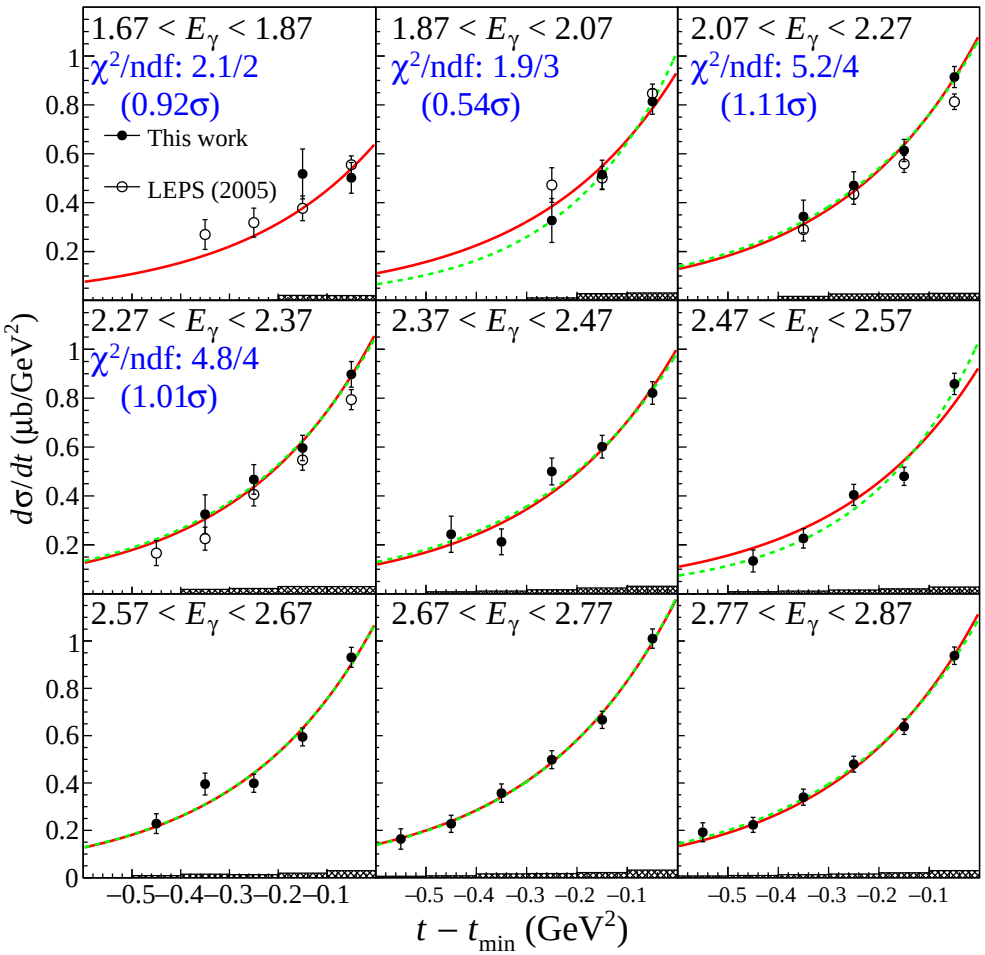

Fig. 4.2: $d\sigma/dt$ vs $t - t_{\rm min}$. The green dashed curves are the fitting results with the free B parameters. The red solid curves are the fitting results with the fixed B ($B = 3.57$ GeV^{-2}). The hatched histograms represent systematic errors.

The obtained differential cross sections are fitted by Eq. (1.20) to extract the t-slope factor B and $(d\sigma/dt)_{t=t_{\rm min}}$ (the green dashed curves in Fig. 4.2). Figure 4.3 shows the energy dependence of the t-slope factor B[1]. The results are consistent with LEPS 2005 results [10] within statistical uncertainties in the overlapping region.

[1] We do not use the lowest energy bin $1.67 < E_\gamma < 1.87$ GeV, since we have only two data points as shown in Fig. 4.2.

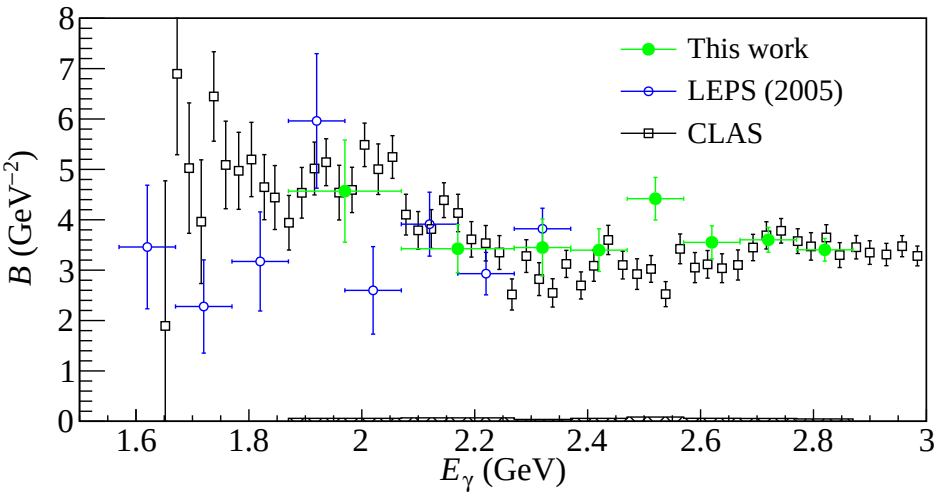

Fig. 4.3: Energy dependence of t-slope factor B, compared to the previous data. The horizontal error bars indicate bin size. The open squares represent the CLAS results for the charged mode with Λ^* cuts included [17]. The hatched histogram represents systematic errors for this work.

Also, the results show no strong energy dependence of B beyond statistical errors, and the average value of B of this work is 3.57 ± 0.12 GeV^{-2}. Comparing the combined LEPS results with the CLAS results, the average B value of LEPS results is smaller than that of CLAS results by 21.7% in the photon energy range of $1.5 < E_\gamma < 2.9$ GeV with the statistical significance of 3.2σ, on the other hand, the LEPS results is larger than the CLAS result by 9.7% in $2.2 < E_\gamma < 2.9$ GeV with 2.4σ.

The fitting curves when the t-slope factor B is fixed to the average value are shown in Fig. 4.2 as red solid curves. Figure 4.4 shows the $(d\sigma/dt)_{t=t_{\rm min}}$ obtained in the two ways. Comparing with the CLAS results, the LEPS measurements show smaller $(d\sigma/dt)_{t=t_{\rm min}}$ below $E_\gamma = 2.2$ GeV, and the energy dependence in the nonmonotonic region is more moderate.

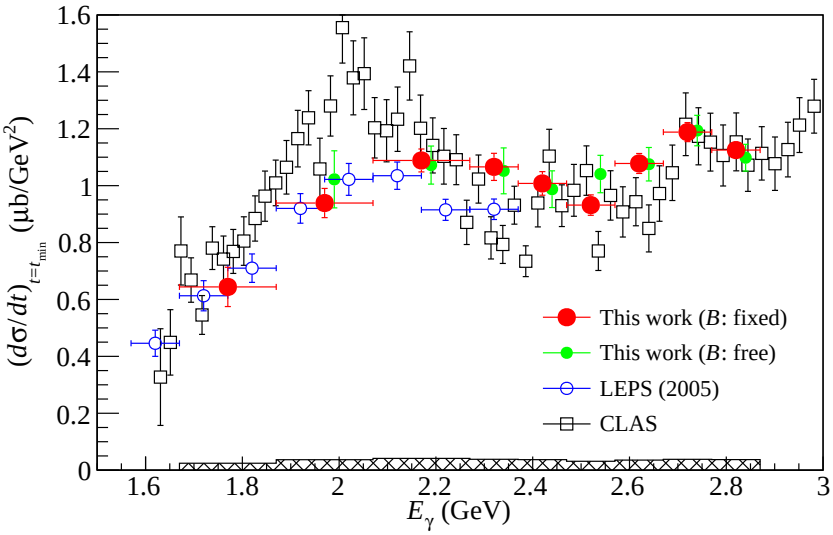

Fig. 4.4: Energy dependence of the $(d\sigma/dt)_{t=t_{\rm min}}$. The red solid circles represent the results with fixing B to 3.57 GeV^2. The horizontal error bars indicate bin size. The hatched histograms represent systematic errors. The green open circles represent the results with B as floating parameters. The green data points are shifted horizontally for clarity.

4.2 Spin Density Matrix Element (SDME)

The SDMEs are extracted using the integrated one-dimensional decay angular distributions [Eqs. (1.33-1.37)]. The systematic errors of the SDMEs are small, since the SDMEs are free from the photon number calculation.

The acceptance-corrected decay angular distributions are fitted to extract SDMEs. We have four data sets 2015 vertical, 2015 horizontal, 2007 vertical, and 2007 horizontal (Table 2.4). As for the angular distributions which do not depend on P_γ [$W(\cos\theta)$ and $W(\varphi)$], the four data sets are summed after the acceptance correction. As for the angular distributions which depend on P_γ [$W(\varphi-\Phi)$, $W(\varphi+\Phi)$, and $W(\Phi)$], only the horizontal and vertical data sets are summed, because P_γ (or the laser wavelengths) are different between 2007 and 2015 data. The simultaneous fittings for 2007 and 2015 data sets were performed for the P_γ-dependent angular distributions, to extract the SDMEs as shown in Figs. 4.5-4.11.

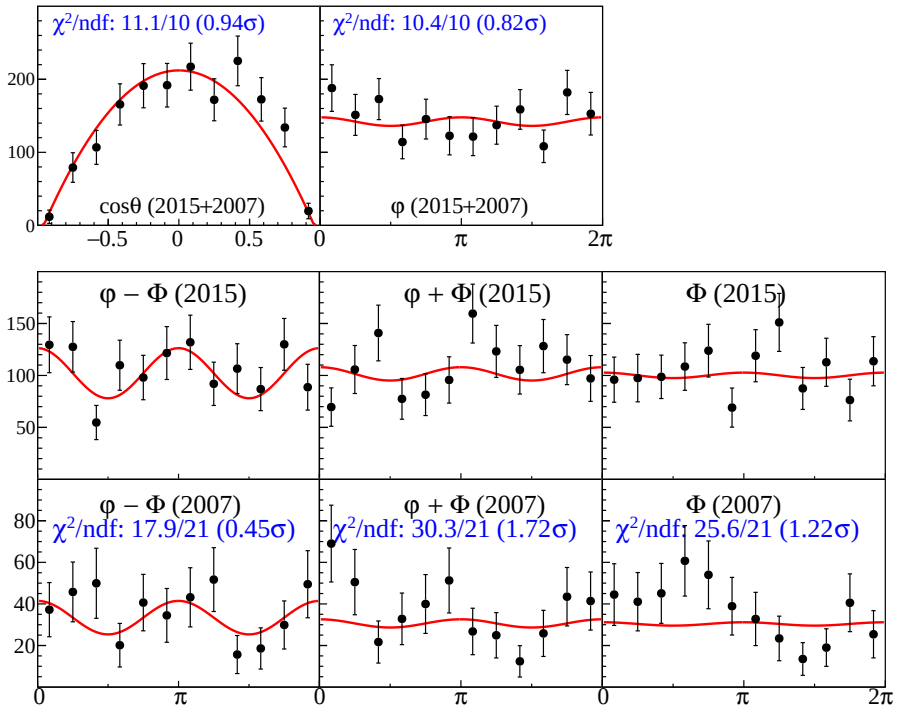

Fig. 4.5: Acceptance-corrected angular distributions for $t - t_{\text{min}} > -0.05$ GeV^2 and $2.17 < E_\gamma < 2.37$ GeV. The red curves are the fitting results.

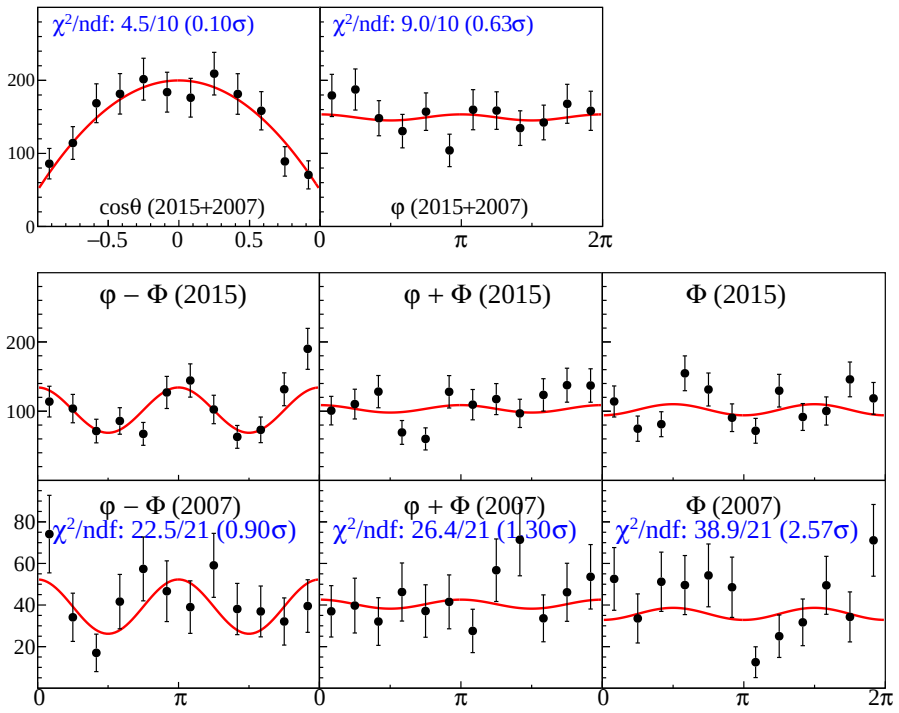

Fig. 4.6: Acceptance-corrected angular distributions for $t - t_{\text{min}} > -0.05$ GeV^2 and $2.37 < E_\gamma < 2.57$ GeV. The red curves are the fitting results.

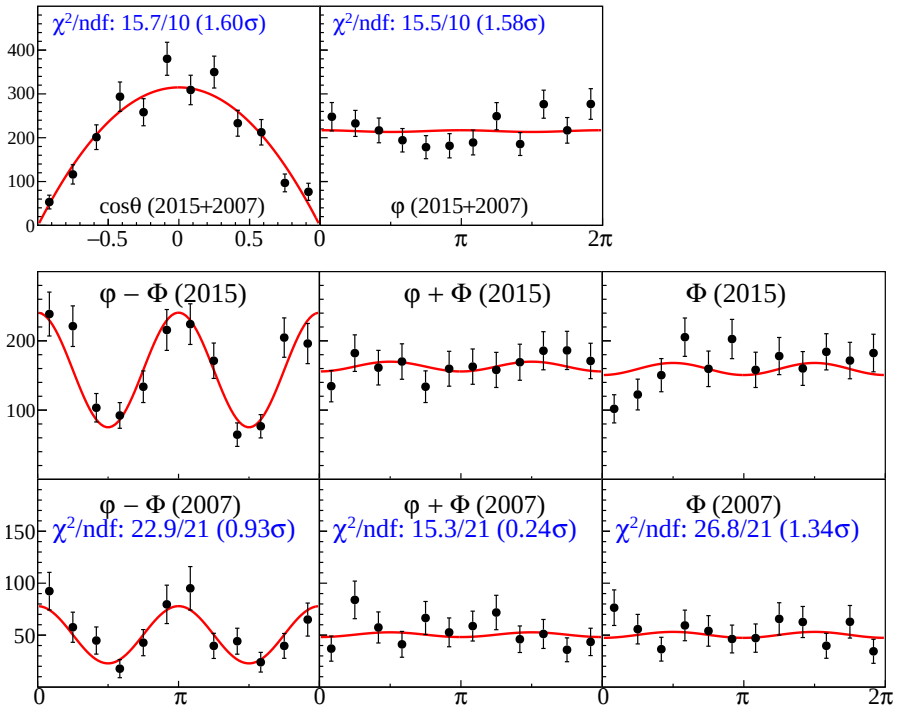

Fig. 4.7: Acceptance-corrected angular distributions for $t - t_{\text{min}} > -0.05$ GeV^2 and $2.57 < E_\gamma < 2.77$ GeV. The red curves are the fitting results.

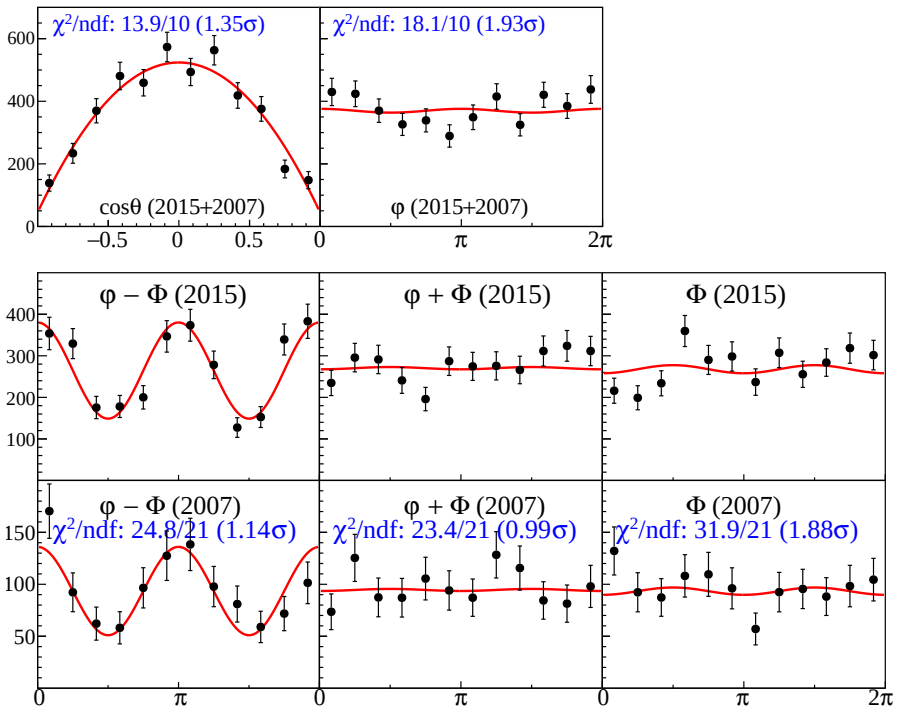

Fig. 4.8: Acceptance-corrected angular distributions for $-0.05 < t - t_{\text{min}} < 0.0$ GeV^2 and $2.37 < E_\gamma < 2.77$ GeV. The red curves are the fitting results.

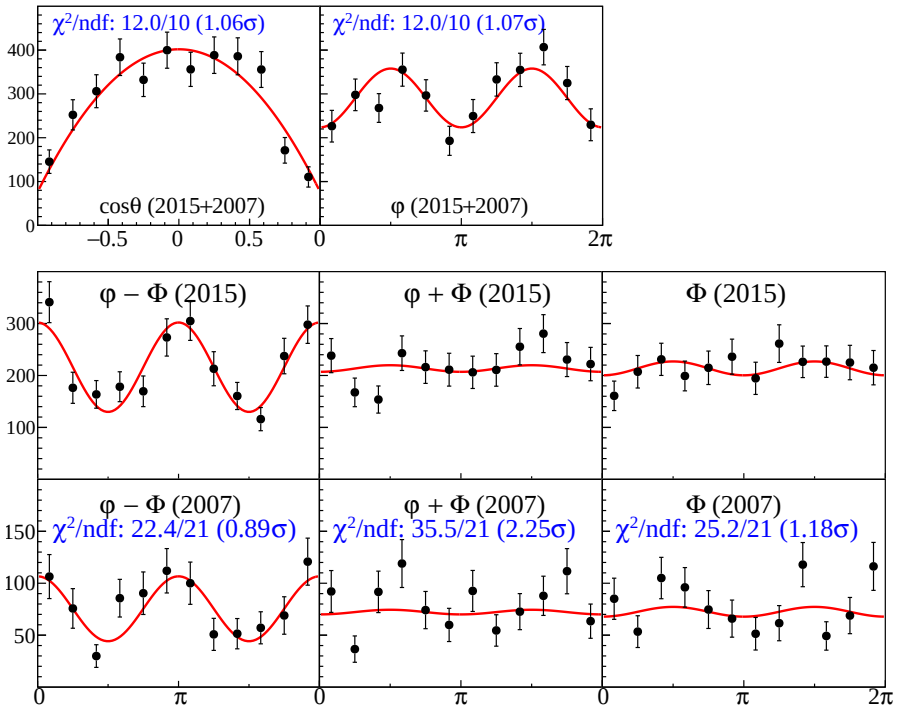

Fig. 4.9: Acceptance-corrected angular distributions for $-0.1 < t - t_{\text{min}} < -0.05$ GeV^2 and $2.37 < E_\gamma < 2.77$ GeV. The red curves are the fitting results.

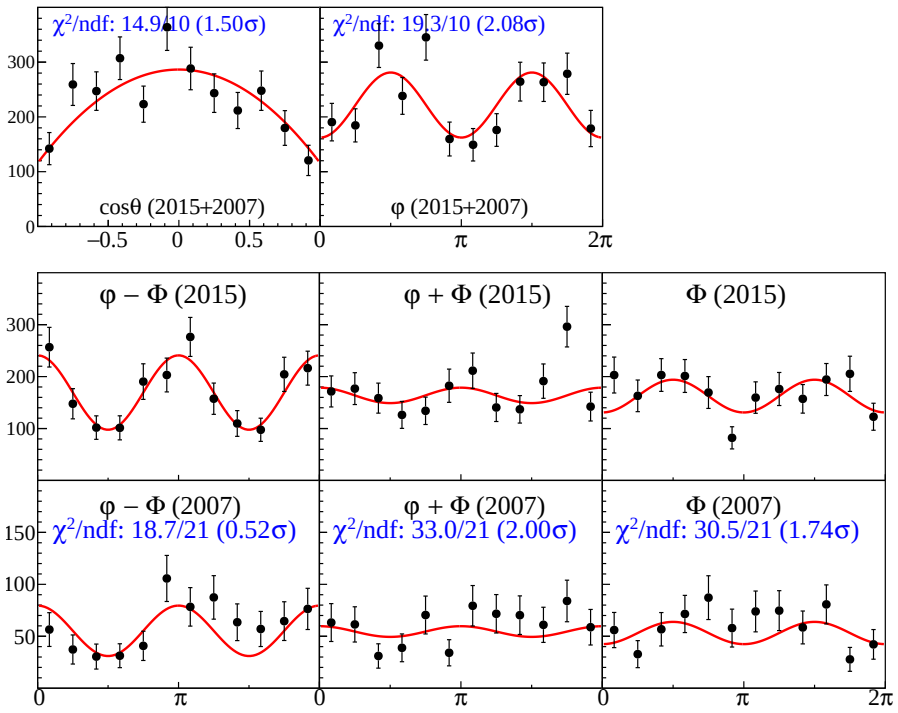

Fig. 4.10: Acceptance-corrected angular distributions for $-0.15 < t - t_{\text{min}} < -0.1$ GeV^2 and $2.37 < E_\gamma < 2.77$ GeV. The red curves are the fitting results.

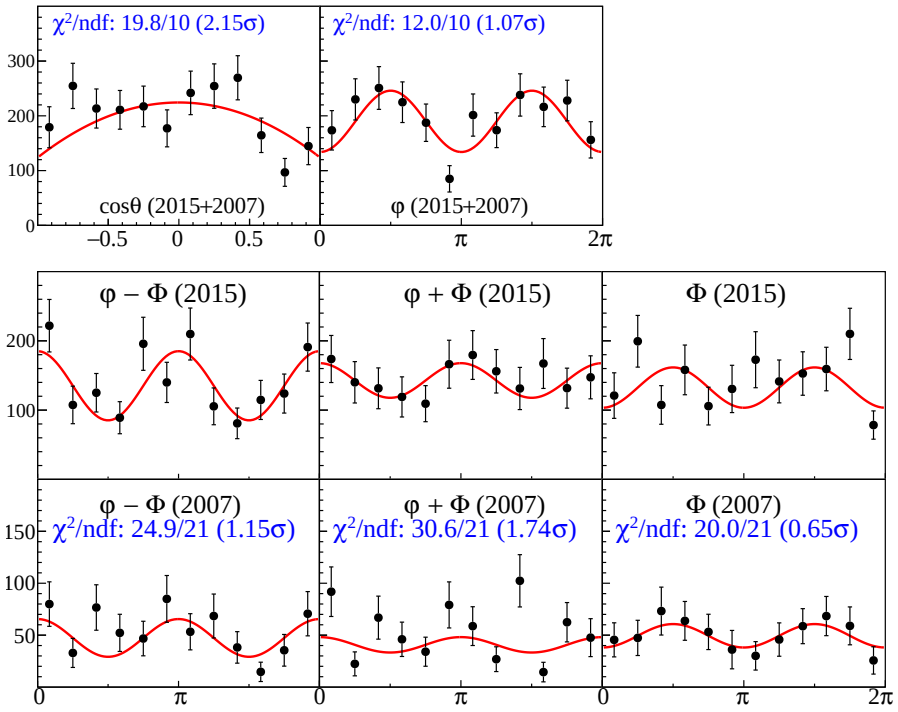

Fig. 4.11: Acceptance-corrected angular distributions for $-0.2 < t - t_{\text{min}} < -0.15$ GeV^2 and $2.37 < E_\gamma < 2.77$ GeV. The red curves are the fitting results.

The SDME results are shown in Fig. 4.12 and Fig. 4.13. Figure 4.12 shows the energy (E_γ) dependence, and Figure 4.13 shows the angular (t) dependence. The results are consistent with LEPS 2010 results [38] in the overlapping energy region. Note that Reρ^0_{1-1} and the photon beam asymmetry $2\rho^1_{11} + \rho^1_{00}$ must go to zero at zero degrees ($t = t_{\text{min}}$) by definition, and the measured values are consistent with zero within the statistical uncertainty.

The SDMEs ρ^0_{00} and Reρ^0_{1-1} in the most forward bin are consistent with zero within the statistical uncertainty, suggesting the helicity conservation. Therefore, the SDME $\bar{\rho}^1_{1-1}$ can be used as an indicator of the t-channel natural- and unnatural- parity exchanges. The values are $\bar{\rho}^1_{1-1} = 0.2 \sim 0.3$ as shown in Fig. 4.12, indicating that the Pomeron-exchange process is dominant ($70 \sim 80\%$).

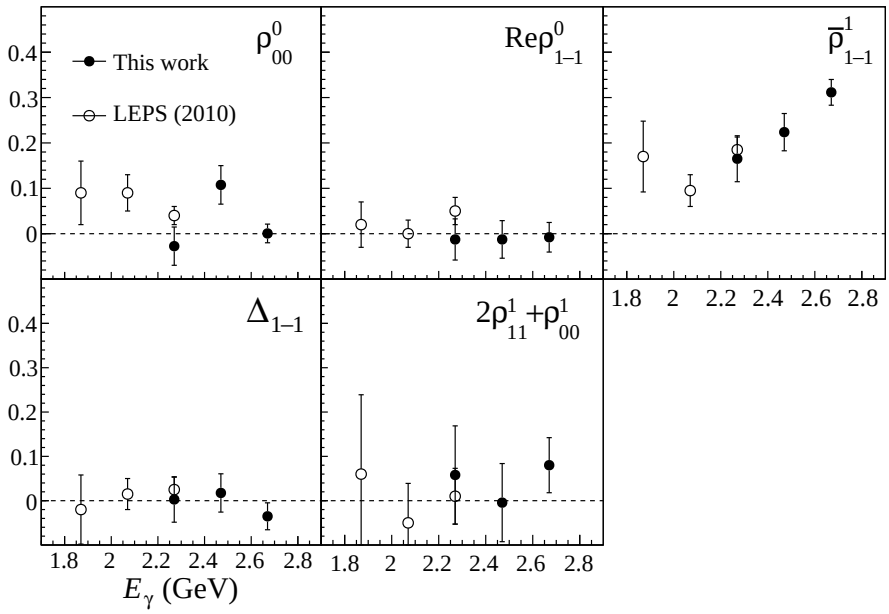

Fig. 4.12: E_γ vs SDME results. The t range is $t - t_{\mathrm{min}} > -0.05$ GeV^2. The results are consistent with LEPS 2010 results [38] in the overlapping energy region.

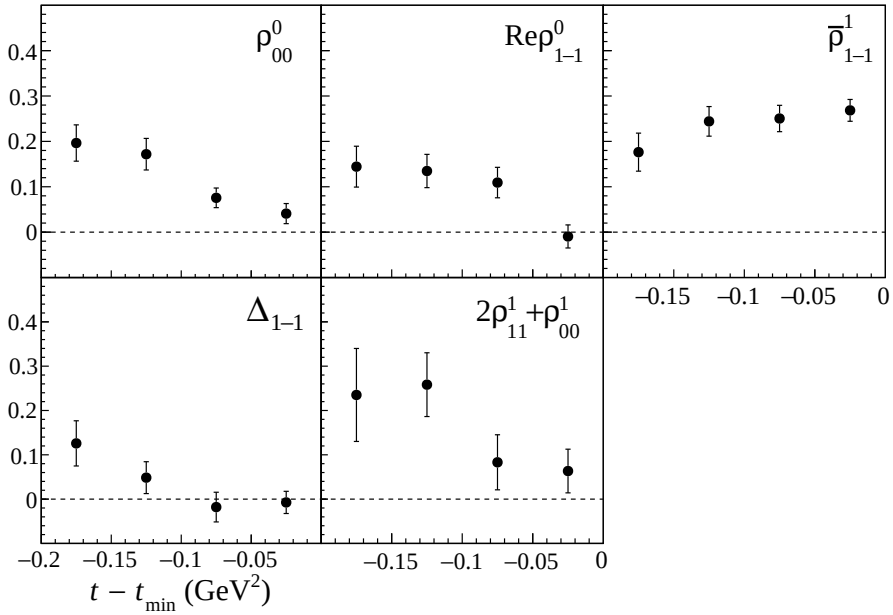

Fig. 4.13: t vs SDME results. The E_γ range is $2.37 < E_\gamma < 2.77$ GeV.

Results in the helicity system

Figure 4.14 shows the t dependence of SDMEs in the helicity frame at $2.37 < E_\gamma < 2.77$ GeV. Since the helicity frame and Gottfried-Jackson frame are the same in the case of the scattering at zero degrees, two results should be the same at zero degrees. Actually, in the most forward t bin, the results in the helicity frame are consistent with the SDMEs in the Gottfried-Jackson frame (Fig. 4.13).

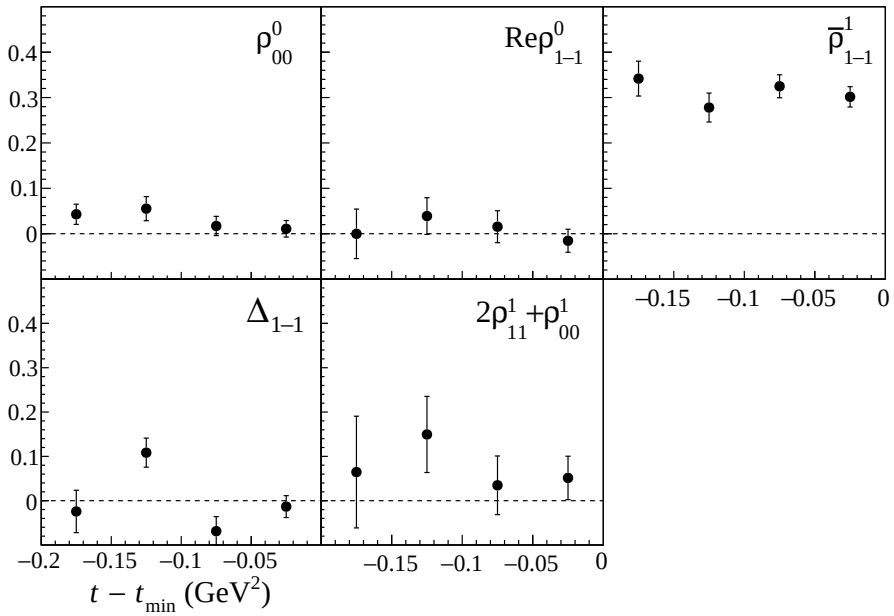

Fig. 4.14: t vs SDME results in the helicity system. The E_γ range is $2.37 < E_\gamma < 2.77$ GeV.

CHAPTER

FIVE

DISCUSSION

In this chapter, we discuss several processes to explain the results. First, the Pomeron, π^0 and η exchanges in the t-channel are considered. After that, the $K^+\Lambda(1520)$ rescattering process will be considered to explain the nonmonotonic structure.

5.1 Pomeron$+\pi^0+\eta$ Amplitude Calculation

In this section, we introduce the Pomeron$+\pi^0+\eta$ model, following Titov's approach [18]. In this model, the Pomeron, π^0, and η are exchanged in the t-channel. The Pomeron exchange amplitude is calculated in the framework of Regge theory. On the other hand, the π^0 and η exchange amplitudes are calculated using an effective Lagrangian approach.

5.1.1 Pomeron exchange amplitude

We use the Donnachie-Landshoff model [67, 68, 69] to calculate the Pomeron exchange amplitude in the following form ([18, 47][1])

$$I^{\mathbb{P}}_{fi} = -M(s,t)\varepsilon^*_\mu(q,\lambda_\phi)\bar{u}(p',m_f)h^{\mu\nu}_{\mathbb{P}}u(p,m_i)\varepsilon_\nu(k,\lambda_\gamma), \tag{5.1}$$

where $\varepsilon(k,\lambda_\gamma)$ [$\varepsilon(q,\lambda_\phi)$] is the polarization vector of the incident photon (outgoing ϕ meson) with momentum k (q) and spin projection λ_γ (λ_ϕ), and $u(p,m_i)$ [$u(p',m_f)$] is the Dirac spinor of the nucleon with momentum p (p') and spin projection m_i (m_f). The scalar function $M(s,t)$ is described by the following Regge parametrization:

$$M(s,t) = C_{\mathbb{P}}F_N(t)F_\phi(t)\left(\frac{s}{s_{\mathbb{P}}}\right)^{\alpha(t)-1}\exp\left(-\frac{i\pi}{2}\alpha(t)\right). \tag{5.2}$$

The isoscalar electromagnetic form factor of the nucleon F_N and the form factor for the ϕ-photon-Pomeron coupling F_ϕ take the following forms:

$$F_N(t) = \frac{4m_N^2 - a_N^2 t}{(4m_N^2 - t)(1-t/t_0)^2}, \tag{5.3}$$

$$F_\phi(t) = \frac{2\mu_0^2}{(1-t/m_\phi^2)(2\mu_0^2 + m_\phi^2 - t)}, \tag{5.4}$$

[1]The sign convention in Ref. [18] is the same as that in Ref. [47]. The definitions of the strength factor $C_{\mathbb{P}}$ are different by factor $s_{\mathbb{P}}$. We use the definition of $C_{\mathbb{P}}$ in Ref. [47] which has dimension GeV^{-2}. The $C_{\mathbb{P}}$ defined in Ref. [18] is dimensionless.

where m_N is the nucleon mass and m_ϕ is the ϕ-meson mass. The parameters used in Eq. (5.2) are listed in Table 5.1.

Table 5.1: Parameters used in the scalar function $M(s,t)$.

$s_{\mathbb{P}}$	4 GeV^2	Refs. [47, 18, 39]
$\alpha(t)$	$1.08 + 0.25t$	Pomeron trajectory
a_N	2	Ref. [39]
t_0	0.7 GeV^2	Refs. [18, 39]
μ_0^2	1.1 GeV^2	Refs. [18, 39]
$C_{\mathbb{P}}$	0.7566 GeV^{-2}	Pomeron strength factor [47]

The vertex function $h_{\mathbb{P}}$ has the following form [18]:

$$h_{\mathbb{P}}^{\mu\nu} = \not{k}\left(g^{\mu\nu} - \frac{q^\mu q^\nu}{q^2}\right) - \gamma^\nu\left(k^\mu - q^\mu\frac{k\cdot q}{q^2}\right) - \left(q^\nu - \frac{p^\nu + p'^\nu}{2}\frac{k\cdot q}{\frac{p+p'}{2}\cdot k}\right)\left(\gamma^\mu - \frac{\not{q} q^\mu}{q^2}\right), \tag{5.5}$$

where p and p' represent the four-momenta of the incoming nucleon and outgoing nucleon, respectively. In this model, the scalar function $M(s,t)$ contains the information about the energy dependence of the exchange of the Pomeron trajectory [Eq. (1.13)], while the vertex function $h_{\mathbb{P}}$ contains the information about the angle dependence.

The invariant amplitudes $I^{\mathbb{P}}_{\lambda_\phi,\lambda_{p'};\lambda_\gamma,\lambda_p}$ at $t = t_{\text{min}}$ are shown in Fig. 5.1. The helicity-conserving amplitude such as $I^{\mathbb{P}}_{1,-1/2;1,-1/2}$ gives the dominant contributions. Its magnitude increases with the energy E_γ. Also, the helicity-flip amplitude $I^{\mathbb{P}}_{0,1/2;1,-1/2}$ has non-zero value near the threshold, though it converges to zero when the energy increases. Note that the $\exp[i\pi\alpha(t)/2]$ factor in Eq. (5.2) makes the Pomeron exchange amplitude predominantly imaginary as is also seen in Fig. 5.1.

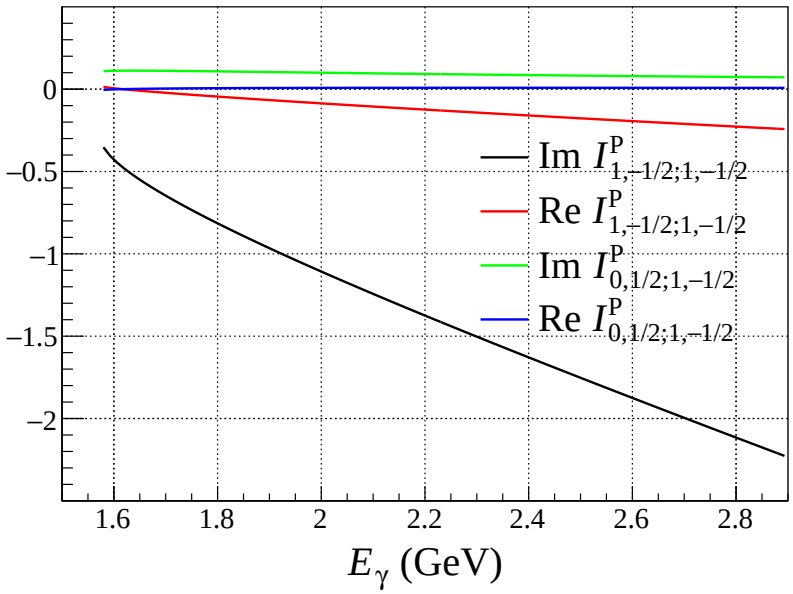

Fig. 5.1: Non-zero Pomeron exchange amplitudes $I^{\mathbb{P}}_{1,-1/2;1,-1/2}$ and $I^{\mathbb{P}}_{0,1/2;1,-1/2}$ at zero degrees ($t = t_{\text{min}}$). Parameter set in Ref. [47] is used. The function shapes do not change much by using the parameter set in Ref. [18].

5.1.2 Pseudoscalar meson exchange amplitude

Pseudoscalar meson ($\varphi = \pi^0,\ \eta$) exchanges in the t-channel contribute to the ϕ photoproduction at forward angles. We use the following effective interaction Lagrangians (Refs. [18, 47, 37, 70, 71, 46][2]):

$$\mathcal{L}_{\phi\gamma\varphi} = \frac{e g_{\phi\gamma\varphi}}{m_\phi} \varepsilon^{\mu\nu\alpha\beta} \partial_\mu \phi_\nu \partial_\alpha A_\beta \varphi \tag{5.6}$$

$$\mathcal{L}_{\varphi NN} = \frac{g_{\varphi NN}}{2m_N} \bar{N} \gamma^\mu \gamma_5 N \partial_\mu \varphi \tag{5.7}$$

where ϕ_ν, A_β, and N denote ϕ-meson, photon, and nucleon fields, respectively. Then, the t-channel pseudoscalar-meson exchange amplitude takes the following form (Refs. [18, 47, 37][3]):

$$I_{fi}^{\mathrm{PS}} = -\sum_{\varphi=\pi^0,\eta} \frac{i F_{\varphi NN}(t) F_{\phi\gamma\varphi}(t)}{t - m_\varphi^2} \frac{e g_{\phi\gamma\varphi} g_{\varphi NN}}{m_\phi} \bar{u}(p', m_f) \gamma_5 u(p, m_i) \varepsilon^{\mu\nu\alpha\beta} q_\mu \varepsilon_\nu^*(q, \lambda_\phi) k_\alpha \varepsilon_\beta(k, \lambda_\gamma) \tag{5.8}$$

$$= -\sum_{\varphi=\pi^0,\eta} \frac{i F_{\varphi NN}(t) F_{\phi\gamma\varphi}(t)}{t - m_\varphi^2} \frac{e g_{\phi\gamma\varphi}}{m_\phi} \frac{g_{\varphi NN}}{2m_N} \bar{u}(p', m_f) (\not{k} - \not{q}) \gamma_5 u(p, m_i) \varepsilon^{\mu\nu\alpha\beta} q_\mu \varepsilon_\nu^*(q, \lambda_\phi) k_\alpha \varepsilon_\beta(k, \lambda_\gamma) \tag{5.9}$$

where k and q represent the four-momenta of the incoming photon and outgoing ϕ meson, respectively. $F_{\varphi NN}$ and $F_{\phi\gamma\varphi}$ are the monopole-type form factors, defined as

$$F_{\varphi NN}(t) = \frac{\Lambda_{\varphi NN}^2 - m_\varphi^2}{\Lambda_{\varphi NN}^2 - t}, \tag{5.10}$$

$$F_{\phi\gamma\varphi}(t) = \frac{\Lambda_{\phi\gamma\varphi}^2 - m_\varphi^2}{\Lambda_{\phi\gamma\varphi}^2 - t}. \tag{5.11}$$

The coupling constants and cut-off masses are listed in Table 5.2.

Table 5.2: Parameters used in the meson exchange amplitude [Eq. (5.8)].

$g_{\phi\gamma\pi}$	-0.141	$\phi\gamma\pi$ coupling constant [47, 18]
$g_{\phi\gamma\eta}$	-0.707	$\phi\gamma\eta$ coupling constant [47, 18]
$g_{\pi NN}$	13.26	πNN coupling constant [47, 18]
$g_{\eta NN}$	3.527	ηNN coupling constant [47, 18]
$\Lambda_{\pi NN}$	0.7 GeV	cutoff parameter [47]
$\Lambda_{\eta NN}$	1 GeV	cutoff parameter [47]
$\Lambda_{\phi\gamma\pi}$	0.77 GeV	cutoff parameter [47]
$\Lambda_{\phi\gamma\eta}$	0.9 GeV	cutoff parameter [47]

The coupling constants of $\phi\gamma\pi^0$ and $\phi\gamma\eta$ vertices are determined through the widths of radiative decays $\phi \to \gamma\pi^0$ and $\phi \to \gamma\eta$ [52]. The πNN coupling is determined by πN partial wave

[2] As for $\mathcal{L}_{\varphi NN}$, our formula is the same as that of Refs. [47, 37, 71, 46] (axial vector coupling). Refs. [18, 70] use so-called pseudoscalar coupling, and this Lagrangian leads to the same amplitude, due to the Dirac equation.

[3] We use the exact same formula as that of Ref. [18]. The sign convention is the same as that of that of Ref. [37], and different from Ref. [47]. Be careful that factor $\frac{1}{2m_N}$ is omitted in Eq. (9) of Ref. [47].

analysis [72]. The ηNN coupling varies in literature [37], however, the η exchange amplitude is small due to its large mass compared with the pion mass, and the effect to the cross section is not large.

Figure 5.2 shows the invariant amplitude $I^{\mathrm{PS}}_{\lambda_\phi,\lambda_{p'};\lambda_\gamma,\lambda_p}$ at $t = t_{\mathrm{min}}$. These amplitudes are purely real, and only the helicity-conserving amplitude has non-zero value at zero degrees. The η exchange amplitude is small compared with the π^0 exchange amplitude, and when energy increases, it falls to zero rapidly. The π^0 exchange amplitude does not fall in the LEPS E_γ region, and contributes to the ϕ photoproduction to some extent.

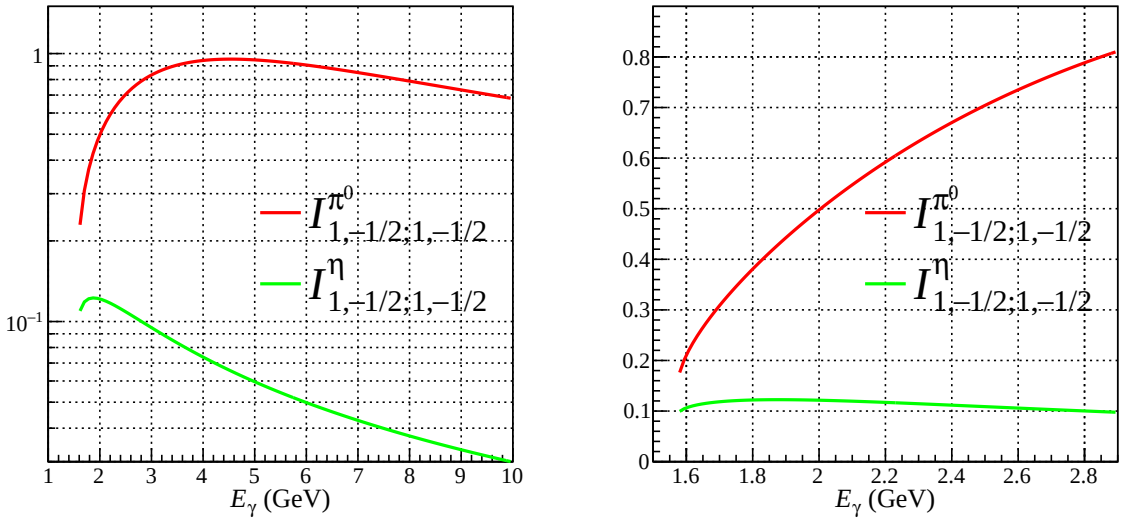

Fig. 5.2: Left: Pseudoscalar meson exchange amplitudes $I^{\mathrm{PS}}_{1,-1/2;1,-1/2}$ at zero degrees [47]. The other spin-flip amplitudes are zero. Right: Zoom-in version of the left one.

5.1.3 Determination of the Pomeron strength factor $C_{\mathbb{P}}$

Since little is known about the Pomeron coupling with the strange quarks, the Pomeron strength factor $C_{\mathbb{P}}$ contains the large uncertainty. Therefore, we determined the strength factor using our $(d\sigma/dt)_{t=t_{\mathrm{min}}}$ results. It is expected that when the energy E_γ increases, the number of processes, which contribute to the $\gamma p \to \phi p$ reaction, decreases and the simple Pomeron model works. Therefore, we determined the Pomeron strength factor $C_{\mathbb{P}}$ using our highest-E_γ data points. The three highest-E_γ data points are used, and $C_{\mathbb{P}} = 0.649(7)$ GeV^{-2} is obtained by a fit, which is 14% smaller than that of Ref. [47]. Here, the fitting curve is the Pomeron+π^0 + η theoretical curve with the floating $C_{\mathbb{P}}$ parameter, as shown in Fig. 5.3. Other parameters such as the pseudoscalar exchange amplitudes are fixed. We use the three points because χ^2/ndf is closest to one when choosing the three data points. The fitting result does not change more than 1.2% when using between two and seven of the highest-E_γ data points.

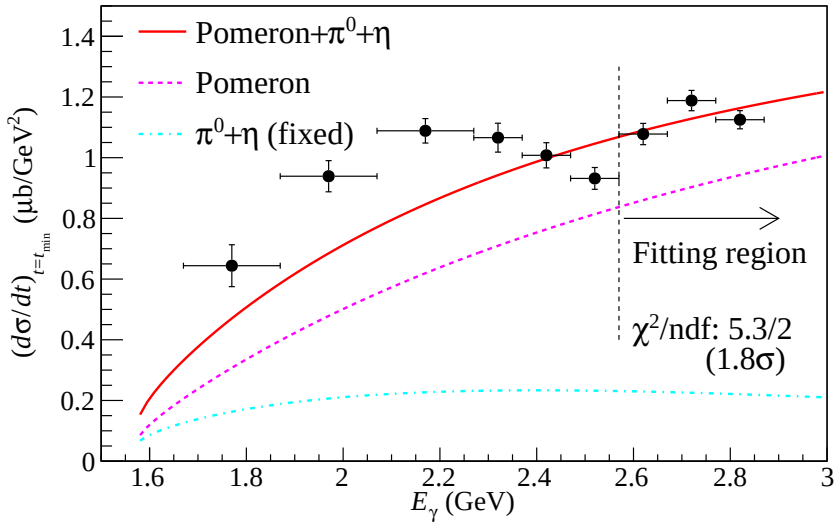

Fig. 5.3: The $C_{\mathbb{P}}$ determination. The red solid curve is the fitting result with the Pomeron strength factor $C_{\mathbb{P}}$ as a floating parameter.

5.1.4 $(d\sigma/dt)_{t=t_{min}}$ and SDME

The energy dependence of $(d\sigma/dt)_{t=t_{min}}$ when the t-slope factor B is fixed to the average value is shown in Fig. 5.4. The theoretical curves with the Pomeron strength factor determined by this work are also shown. Comparing with theoretical calculations, the data shows a $20 - 30\%$ excess below $E_\gamma = 2.27$ GeV, suggesting the existence of other processes near threshold.

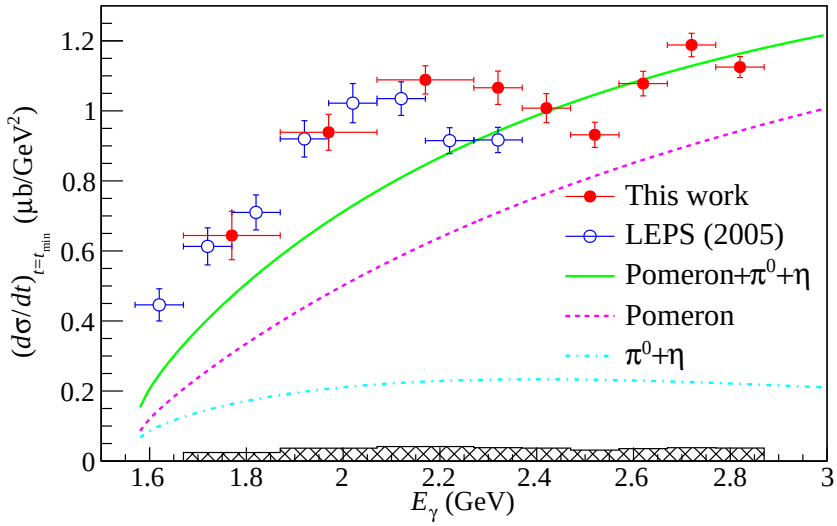

Fig. 5.4: Energy dependence of $(d\sigma/dt)_{t=t_{min}}$. The red solid circles are the results of the present work. The error bars represent statistical errors. The hatched histogram represents systematic errors. The green solid curve represents the theoretical calculation with the Pomeron strength factor determined by the present measurements. The magenta and cyan dashed curves represent the contributions of Pomeron and pseudoscalar mesons respectively.

The t dependences of the spin-density matrix elements in $2.37 < E_\gamma < 2.77$ GeV are shown in Fig. 5.5. The red solid curves represent the theoretical calculations at $E_\gamma = 2.57$ GeV using the Pomeron strength factor determined by the cross sections ($C_{\mathbb{P}} = 0.649$ GeV^{-2}). The green dashed curves represent the calculations with $C_{\mathbb{P}} = 0.7566$ GeV^{-2} [47]. Now $\bar{\rho}^1_{1-1}$ is the most important spin-density matrix element, which is sensitive to the ratio of t-channel natural and unnatural parity exchanges, and the theoretical curve using the Pomeron strength factor determined here is closer to the measurements of $\bar{\rho}^1_{1-1}$ than the curve using the strength factor in Ref. [47]. In the large scattering angle region $t - t_{\rm min} < -0.1$ GeV^2, Δ_{1-1} and the beam asymmetry $2\rho^1_{11} + \rho^1_{00}$ are slightly larger than the theoretical calculations. In the forward region $t - t_{\rm min} > -0.1$ GeV^2, the theoretical model (Pomeron+$\pi^0 + \eta$) well reproduces the measured SDMEs.

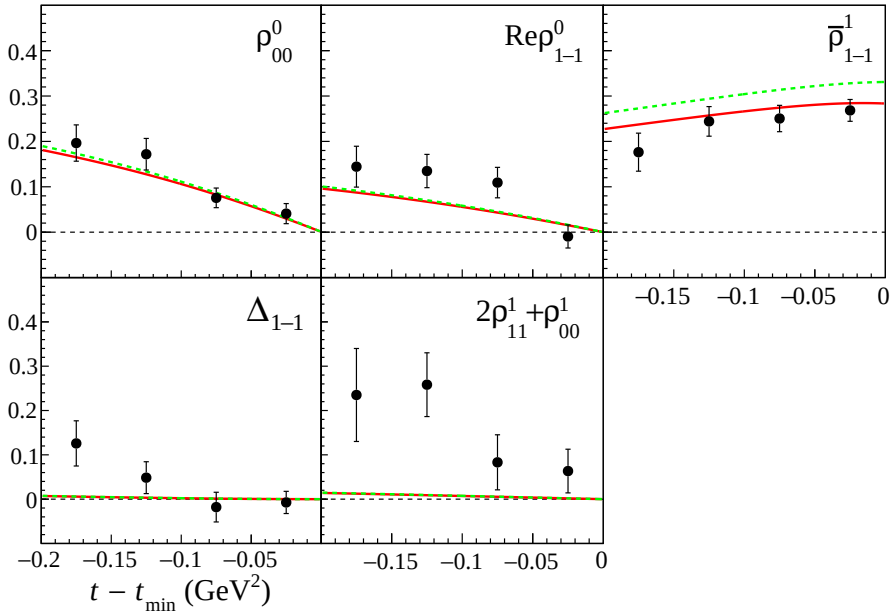

Fig. 5.5: t dependence of spin-density matrix elements in the Gottfried-Jackson frame. The energy range is $2.37 < E_\gamma < 2.77$ GeV. The red solid curves represent the theoretical calculations at $E_\gamma = 2.57$ GeV with the Pomeron strength factor $C_{\mathbb{P}}$ determined by this work. The green dashed curves represent the same model with $C_{\mathbb{P}} = 0.7566$ GeV^{-2} [47].

Figure 5.6 shows E_γ dependences of the spin-density matrix elements in the forward region $t - t_{\rm min} > -0.05$ GeV^2. As for $\bar{\rho}^1_{1-1}$, the data points in the high energy region $E_\gamma > 2.37$ GeV are well described by the Pomeron and pseudoscalar exchange model, and the data point in $1.97 < E_\gamma < 2.17$ GeV significantly deviates from the model prediction with a statistical significance of 3.4σ. This fact suggests that additional amplitudes or interferences between the Pomeron exchange and other processes appear near threshold. If the interference effect can be ignored, the additional process is the unnatural parity exchange process other than π^0 and η exchanges.

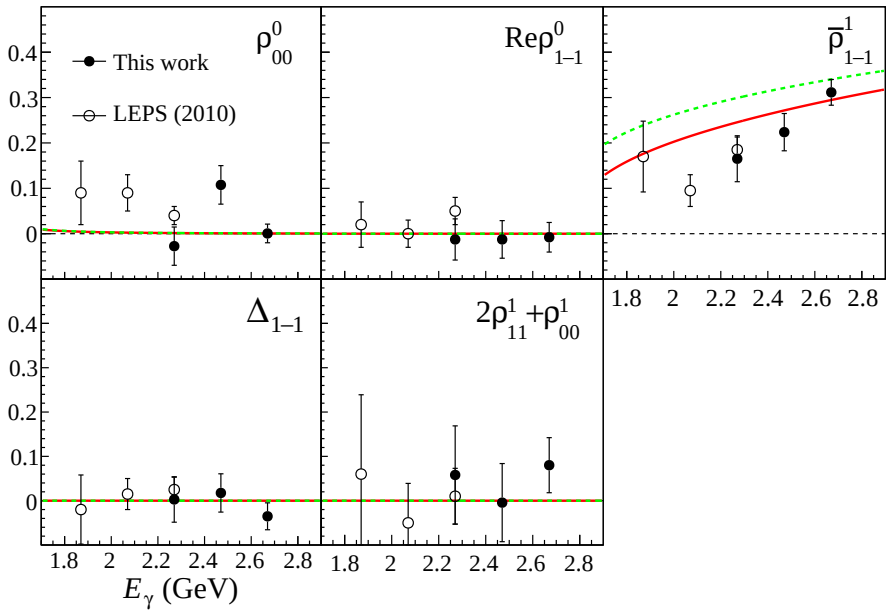

Fig. 5.6: E_γ dependence of spin-density matrix elements in the Gottfried-Jackson frame. The t range is $t - t_{\mathrm{min}} > -0.05$ GeV^2. The open circles represent the previous LEPS results [10]. The red solid curves represent the theoretical calculations at zero degrees ($t = t_{\mathrm{min}}$) with the Pomeron strength factor $C_{\mathbb{P}}$ determined by this work. The green dashed curves represent the same model with $C_{\mathbb{P}} = 0.7566$ GeV^{-2} [47].

As for t-slope factor B, further studies are necessary to reproduce our results. Especially, the form factor of the Pomeron-γ-ϕ contains large uncertainties, and needs to be adjusted.

5.2 $K^+\Lambda(1520)$ Rescattering Process

In this section, we calculate the amplitude of $\gamma p \to K^+\Lambda(1520) \to \phi p$ rescattering process in an effective Lagrangian approach.

5.2.1 Formalism

Using the Cutkosky rule [Eq. (1.7)], the imaginary part of the rescattering amplitude $I^{\mathrm{rescatt.}}$ is written as follows [47][4]:

$$\mathrm{Im}I^{\mathrm{rescatt.}} = \frac{r}{8\pi\sqrt{s}} \int \frac{d\Omega}{4\pi} I_L(\gamma p \to K^+\Lambda^*) I_R^\dagger(K^+\Lambda^* \to \phi p), \tag{5.12}$$

where r is the magnitude of the 3-momentum of the outgoing K^+ of the first scattering in the center-of-mass frame. Note that this K^+ is on mass shell. Other rescattering channels such as $\gamma p \to \pi N \to \phi p$ are ignored, since Ryu *et al.* shows they give small contributions [47]. The real part of the scattering amplitude is also ignored in the same manner as Ryu *et al.*. Figure 5.7

[4]The sign convention of the invariant amplitude $\mathcal{M}$ in Ref. [47] is different from the invariant amplitude I in Ref. [18]. $\mathcal{M} = -I$.

shows the Feynman diagrams for the $K^+\Lambda(1520)$ rescattering process. As shown in the figure, the left-hand (right-hand) side amplitude $I_L(\gamma p \to K^+\Lambda^*)$ [$I_R(K^+\Lambda^* \to \phi p)$] is calculated by summing up the three different types of the tree level diagrams (s-channel, t-channel, and contact-term contributions).

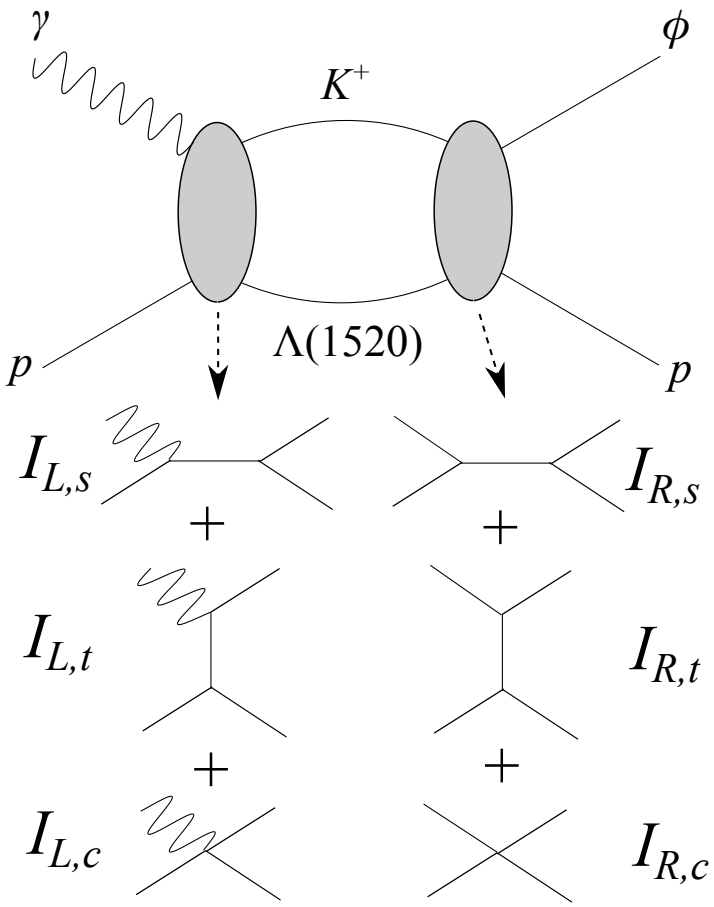

Fig. 5.7: Feynman diagrams for the $\gamma p \to K^+\Lambda(1520) \to \phi p$ rescattering process.

To take into account the higher order effects, the form factors F_L and F_R are introduced as follows:

$$I_L(\gamma p \to K^+\Lambda^*) = (I_{L,s} + I_{L,t} + I_{L,c})F_L(s,t), \tag{5.13}$$
$$I_R(K^+\Lambda^* \to \phi p) = (I_{R,s} + I_{R,t} + I_{R,c})F_R(s,t), \tag{5.14}$$

where $I_{L,s}$ ($I_{R,s}$), $I_{L,t}$ ($I_{R,t}$), and $I_{L,c}$ ($I_{R,c}$) represent the s-channel, the t-channel, and the contact-term amplitudes of the $\gamma p \to K^+\Lambda(1520)$ [$K^+\Lambda(1520) \to \phi p$] reaction, respectively. The form factors are parametrized in a gauge-invariant manner:

$$F_R(s,t) = \left(\frac{n_1\Lambda_1^4}{n_1\Lambda_1^4 + (s-m_p^2)^2}\right)^{n_1}\left(\frac{n_2\Lambda_2^4}{n_2\Lambda_2^4 + t^2}\right)^{n_2}, \tag{5.15}$$
$$F_L(s,t) = \left(\frac{n_3\Lambda_3^4}{n_3\Lambda_3^4 + (s-m_p^2)^2}\right)^{n_3}\left(\frac{n_4\Lambda_4^4}{n_4\Lambda_4^4 + t^2}\right)^{n_4}. \tag{5.16}$$

To calculate the amplitudes, we use the following effective interaction Lagrangian densities for

the $\gamma p \to K^+\Lambda(1520) \to \phi p$ reaction [47, 73, 74, 75, 76, 77, 78, 79]:

$$\mathcal{L}_{\gamma KK} = -ie\left[\left(\partial^\mu K^-\right)K^+ - \left(\partial^\mu K^+\right)K^-\right]A_\mu, \tag{5.17}$$

$$\mathcal{L}_{\gamma NN} = -e\bar{N}\left[\left(\gamma^\mu - \frac{\kappa_p}{2m_p}\sigma^{\mu\nu}\partial_\nu\right)A_\mu\right]N, \tag{5.18}$$

$$\mathcal{L}_{\gamma KN\Lambda^*} = -ie\frac{g_{KN\Lambda^*}}{m_K}\bar{N}\gamma_5 A_\mu K^+\Lambda^{*\mu}, \tag{5.19}$$

$$\mathcal{L}_{KN\Lambda^*} = \frac{g_{KN\Lambda^*}}{m_K}\bar{N}\gamma_5\left(\partial_\mu K^+\right)\Lambda^{*\mu}, \tag{5.20}$$

$$\mathcal{L}_{\phi KK} = -ig_{\phi KK}\left[\left(\partial^\mu K^-\right)K^+ - \left(\partial^\mu K^+\right)K^-\right]\phi_\mu, \tag{5.21}$$

$$\mathcal{L}_{\phi NN} = -g_{\phi NN}\bar{N}\left[\left(\gamma^\mu - \frac{\kappa_\phi}{2m_p}\sigma^{\mu\nu}\partial_\nu\right)\phi_\mu\right]N, \tag{5.22}$$

$$\mathcal{L}_{\phi KN\Lambda^*} = -ig_{\phi KK}\frac{g_{KN\Lambda^*}}{m_K}\bar{N}\gamma_5\phi_\mu K^+\Lambda^{*\mu}, \tag{5.23}$$

where K and Λ^* denote the kaon and $\Lambda(1520)$ fields, respectively. Then, the amplitudes can be written as follows [47]:

$$I_{L,s} = -i\frac{eg_{KN\Lambda^*}}{m_K}\bar{u}^\mu(p_2)k_{2\mu}\gamma_5\frac{\not{q}_s + m_p}{q_s^2 - m_p^2}\not{\varepsilon}_\gamma u(p_1) + i\frac{eg_{KN\Lambda^*}}{m_K}\frac{\kappa_p}{2m_p}\bar{u}^\mu(p_2)k_{2\mu}\gamma_5\frac{\not{q}_s + m_p}{q_s^2 - m_p^2}\not{\varepsilon}_\gamma\not{k}_1 u(p_1), \tag{5.24}$$

$$I_{L,t} = i\frac{2eg_{KN\Lambda^*}}{m_K}\bar{u}^\mu(p_2)\frac{q_{t,\mu}k_2\cdot\varepsilon_\gamma}{q_t^2 - m_K^2}\gamma_5 u(p_1), \tag{5.25}$$

$$I_{L,c} = i\frac{eg_{KN\Lambda^*}}{m_K}\bar{u}^\mu(p_2)\varepsilon_{\gamma,\mu}\gamma_5 u(p_1), \tag{5.26}$$

$$I_{R,s} = i\frac{g_{KN\Lambda^*}g_{\phi NN}}{m_K}\bar{u}(p_2)\not{\varepsilon}^*_\phi\frac{\not{q}_s + m_p}{q_s^2 - m_p^2}\gamma_5 k_{1,\mu}u^\mu(p_1) - i\frac{g_{KN\Lambda^*}g_{\phi NN}}{m_K}\frac{\kappa_\phi}{2m_p}\bar{u}(p_2)\not{k}_2\not{\varepsilon}^*_\phi\frac{\not{q}_s + m_p}{q_s^2 - m_p^2}\gamma_5 k_{1,\mu}u^\mu(p_1), \tag{5.27}$$

$$I_{R,t} = i\frac{g_{KN\Lambda^*}g_{\phi KK}}{m_K}\frac{2k_1\cdot\varepsilon^*_\phi}{q_t^2 - m_K^2}\bar{u}(p_2)\gamma_5 q_{t,\mu}u^\mu(p_1), \tag{5.28}$$

$$I_{R,c} = i\frac{g_{KN\Lambda^*}g_{\phi KK}}{m_K}\bar{u}(p_2)\gamma_5\varepsilon^*_{\phi,\mu}u^\mu(p_1), \tag{5.29}$$

where k_1 is the 4-momentum of the incoming meson (or photon), and k_2 is the 4-momentum of the outgoing meson. p_1 (p_2) is the 4-momentum of the incoming (outgoing) baryon. $q_s = k_1 + p_1$ and $q_t = k_1 - k_2$. u^μ (u with a contravariant index μ) represents a Rarita-Schwinger vector-spinor for the $\Lambda(1520)$ (spin-3/2) field [51].

Table 5.3 shows the parameters used in the present work, which are taken from Ref. [47].

Table 5.3: The coupling constants and anomalous magnetic moments used in the calculation of the rescattering process.

$g_{KN\Lambda^*}$	11	$KN\Lambda(1520)$ coupling constant [80]
$g_{\phi NN}$	0.25	ϕNN coupling constant
$g_{\phi KK}$	4.7	ϕKK coupling constant
κ_p	1.79	anomalous magnetic moment [52]
κ_ϕ	0.2	anomalous magnetic moment [81]

5.2.2 Form factor for the $\gamma p \to K^+\Lambda(1520)$ reaction

As shown in Fig. 5.8, the form factor $F_L(s,t)$ for the $\gamma p \to K^+\Lambda(1520)$ reaction [Eq. (5.16)] is determined using the energy dependence of the total cross section measured by CLAS Collaboration [82].

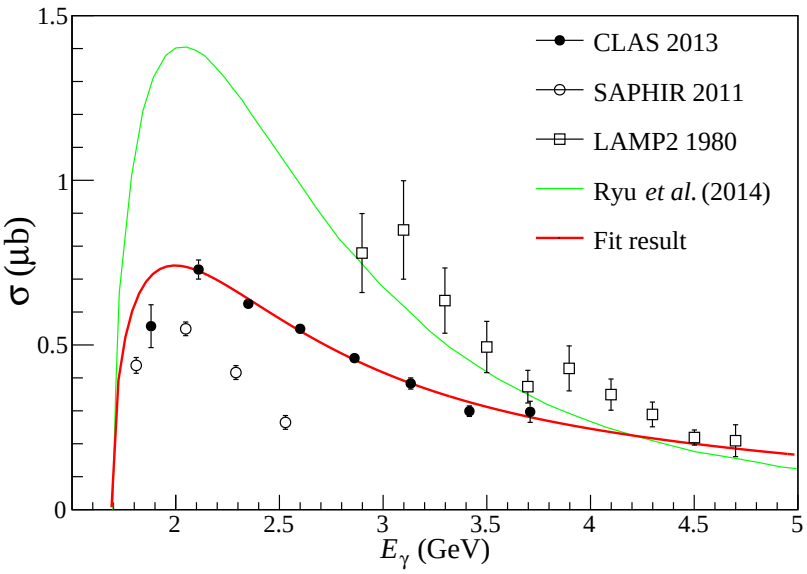

Fig. 5.8: Total cross section for the $\gamma p \to K^+\Lambda(1520)$ reaction. The solid circles represent the CLAS results [82], and the open circles are the SAPHIR results [83]. The open squares represent the LAMP2 results [84]. The green solid curve is taken from Ref. [47].

The obtained parameters are listed in Table 5.4.

Table 5.4: Cut-off parameters used in Eq. (5.16).

n_3	0.6
n_4	8
Λ_3	1.16 GeV
Λ_4	2.74 GeV

The result of Ryu *et al.* is overlaid in Fig. 5.8 for reference. Because they use the SAPHIR 2011 data to tune the form factor $F_L(s,t)$, two calculation results are rather different.

5.2.3 Numerical results

Since there are no experimental data for the $K^+\Lambda(1520) \to \phi p$ reaction, the form factor $F_R(s,t)$ [Eq. (5.15)] is determined using the energy dependence of $(d\sigma/dt)_{t=t_{\rm min}}$ for the $\gamma p \to \phi p$ reaction, which is obtained by this work. In addition to n_1, n_2, Λ_1, and Λ_2 in Eq. (5.15), the Pomeron strength factor $C_{\mathbb{P}}$ is redetermined by a fit. Figure 5.9 shows the fitting results. Note that we do not use a Pomeron suppression factor, which Ryu *et al.* have

used [47] (see Fig. 1.25). By introducing the $K^+\Lambda(1520)$ rescattering effect, the excess around $E_\gamma = 2$ GeV is reproduced in some degree.

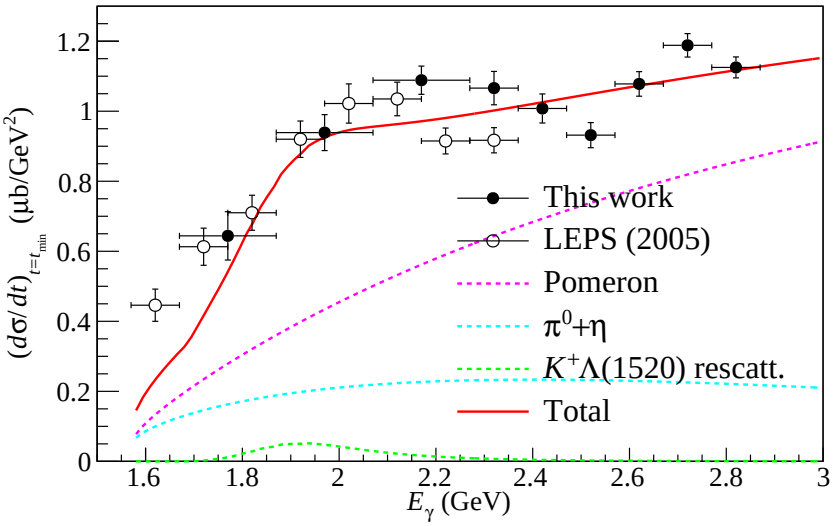

Fig. 5.9: Energy dependence of $(d\sigma/dt)_{t=t_{\rm min}}$. The red solid curve represents the theoretical calculation with the $K^+\Lambda(1520)$ rescattering effect included.

The fitting results are shown in Table 5.5.

Table 5.5: Cut-off parameters in Eq. (5.15) and redetermined Pomeron strength factor $C_{\mathbb{P}}$.

n_1	5
n_2	15
Λ_1	2.81 GeV
Λ_2	0.504 GeV
$C_{\mathbb{P}}$	0.618 GeV^{-2}

The results of spin-density matrix elements at $t = t_{\rm min}$ are shown in Fig. 5.10.

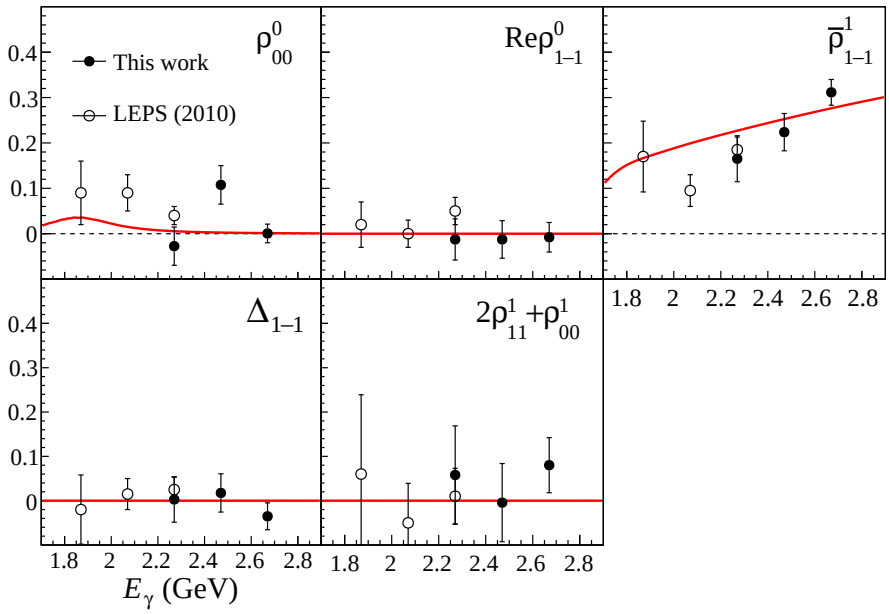

Fig. 5.10: E_γ dependence of spin-density matrix elements in the Gottfried-Jackson frame. The red solid curves represent the theoretical calculations at $t = t_{\mathrm{min}}$ including the $K^+\Lambda(1520)$ rescattering effect.

As for $\bar{\rho}^1_{1-1}$, the $K^+\Lambda(1520)$ rescattering process gives almost zero, while the Pomeron exchange amplitude gives $+0.5$. Therefore, the calculation result is smaller than that of Pomeron$+\pi^0+\eta$ model (Fig. 5.6), although the difference is very small. Furthermore, the theoretical curve still overestimates the data point for $1.97 < E_\gamma < 2.17$ GeV bin.

Even though the uncertainty about the from factor of the $K^+\Lambda(1520) \to \phi p$ reaction is large, and we ignored the real part of the amplitude, the rescattering could explain the $E_\gamma = 2$ GeV excess without any artificial Pomeron suppression factor. To confirm whether the $K^+\Lambda(1520)$ rescattering effect is significant or not, the ϕ photoproduction from the neutron gives valuable information. The contribution of the rescattering process $\gamma n \to K^0\Lambda(1520) \to \phi n$ is considered to be smaller than that of the $\gamma p \to K^+\Lambda(1520)$, since the cross section for the photoproduction of $\Lambda(1520)$ from the neutron is smaller than that from the proton [85].

5.3 Natural-Parity Exchange Contributions Extracted from γ^4He $\to \phi^4$He Reaction

As described in section 1.3.3, the γ^4He $\to \phi^4$He reaction can be used as a filter of natural-parity exchange processes. From the measurement of the γ^4He reaction, Hiraiwa *et al.* evaluated the contribution of the natural-parity exchange processes to the γp reaction $(d\sigma/dt)^{\mathrm{NP}}_{t=t_{\mathrm{min}}}$ using three different models (model-1, model-2, and model-3) [42].

In the model-1, the energy dependence of the $(d\sigma/dt)^{\mathrm{NP}}_{t=t_{\mathrm{min}}}$ is as follows:

$$\left(\frac{d\sigma}{dt}\right)^{\mathrm{NP}}_{t=t_{\mathrm{min}}} \propto \left(\frac{k_\phi}{k_\gamma}\right)^2, \tag{5.30}$$

where k_ϕ (k_γ) is the 3-momentum of the ϕ meson (incident photon) in the center-of-mass frame. In the model-2, a conventional Pomeron model in Ref. [39] is used. In the model-3, the energy dependence of the Pomeron exchange process is modified to make a threshold enhancement, which is equivalent to the conventional Pomeron exchange contribution plus an additional daughter Pomeron exchange contribution. For each model, the overall strength is determined to fit the energy dependence of $(d\sigma/dt)_{t=t_{\rm min}}$ for the γ^4He $\to \phi^4$He reaction. The results are shown in Fig. 5.11. The conversion between $(d\sigma/dt)_{t=t_{\rm min}}$ for the γ^4He $\to \phi^4$He reaction and $(d\sigma/dt)^{\rm NP}_{t=t_{\rm min}}$ is performed using the charge form factor of helium-4 [42, 86].

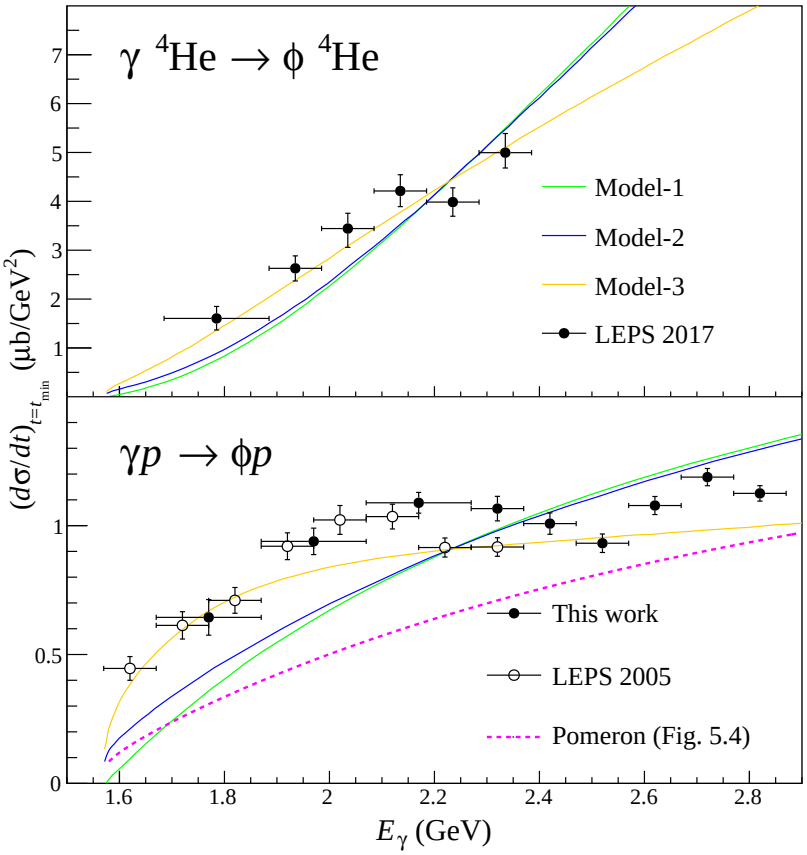

Fig. 5.11: E_γ dependence of $(d\sigma/dt)_{t=t_{\rm min}}$ for γ^4He $\to \phi^4$He reaction (top) [42] and $\gamma p \to \phi p$ reaction (bottom) [10]. The magenta dashed curve represents the Pomeron contribution determined by this work (Fig. 5.4).

The model-1 and model-2 produce the similar results, and they overestimate the $(d\sigma/dt)_{t=t_{\rm min}}$ for the γp reaction above $E_\gamma = 2.37$ GeV, though they contain only natural-parity exchange processes. On the other hand, they underestimate the $(d\sigma/dt)_{t=t_{\rm min}}$ below $E_\gamma = 2.17$ GeV. These observations are difficult to explain without introducing complicated energy-dependent interference effects between natural- and unnatural-exchange processes. Out of these models, the model-3 describes the γ^4He reaction well. As for the γp reaction, the $(d\sigma/dt)^{\rm NP}_{t=t_{\rm min}}$ of the model-3 well reproduces the $(d\sigma/dt)_{t=t_{\rm min}}$ results near threshold, suggesting that the unnatural-parity exchange processes interfere with the additional daughter Pomeron exchange process destructively. In the higher energy region above $E_\gamma > 2.37$ GeV, the model-3 overestimates the Pomeron contribution determined by this work, which is difficult to explain without the modification of the Pomeron exchange amplitude. It is not trivial that the method to convert the

cross section for the γ^4He reaction to that for the γp reaction works well, and further studies are needed in order to explain the γp and γ^4He reactions consistently. Especially, the cross section measurements of the $\gamma^4\text{He} \to \phi^4\text{He}$ above $E_\gamma = 2.37$ GeV is important to distinguish models (Fig. 5.11).

The predominantly imaginary Pomeron-exchange amplitude at low energies is not trivial, and it is also possible that the Pomeron-exchange amplitude interferes with other amplitudes near threshold. To pin down the interference effects, ϕ photoproduction from the deuteron is helpful in addition to the coherent production from the ^{4}He. The coherent production from the deuteron can be used to extract η and Pomeron exchange contributions, and the ratio of the production rate of neutrons to that of protons in incoherent production can be used to disentangle the π^0, η and Pomeron exchange amplitudes. Precise measurements of these reactions and an understanding of the Pomeron-exchange amplitude at lower energies are desired.

CHAPTER

SIX

SUMMARY

We have measured the $\gamma p \to \phi p$ reaction at $E_\gamma = 1.5 - 2.9$ GeV to study the nonmonotonic structure around $E_\gamma = 2.1$ GeV in the energy dependence of $(d\sigma/dt)_{t=t_{\rm min}}$. The experiment was performed at SPring-8/LEPS, using a linearly polarized backward-Compton-scattering photon beam. 8.0×10^{11} photons at $E_\gamma = 1.5 - 2.9$ GeV were injected into an LH_2 target (1.18 g/cm^2), and produced charged hadrons were detected by the LEPS spectrometer covering forward angles (± 0.4 rad in horizontal direction, ± 0.2 rad in vertical direction). The K^+K^- decay mode was used to study the ϕ meson.

We have analyzed the K^+K^- detected events, and the recoil proton was identified using the missing mass distribution $M(\gamma, K^+K^-)$. The K^+K^- invariant mass distribution showed a clear peak corresponding to the ϕ meson on top of the background. The background was subtracted using the ϕp, $K^+\Lambda(1520)$, and nonresonant K^+K^-p templates obtained from the Monte Carlo simulation.

The number of ϕ mesons was obtained by counting events in $1.005 < M(K^+K^-) < 1.035$ GeV/c^2, where $M(K^+K^-)$ is the background subtracted K^+K^- invariant mass distribution. The acceptance correction was performed using the Monte Carlo simulation, and the differential cross section $d\sigma/dt$ and spin-density matrix elements were extracted. The cross section results show the forward peaking structure suggesting the dominance of the t-channel processes, and the t-slope factor B and $(d\sigma/dt)_{t=t_{\rm min}}$ were obtained with an exponential curve fitting. The energy dependence of the $(d\sigma/dt)_{t=t_{\rm min}}$ is different from that of CLAS measurements. Comparing with the CLAS results, the LEPS measurements show smaller $(d\sigma/dt)_{t=t_{\rm min}}$ below $E_\gamma = 2.2$ GeV, and the energy dependence in the nonmonotonic region is more moderate. Also, the energy dependence of the t-slope factor B shows a different behavior from the CLAS results. The LEPS results show no strong energy dependence, and are 21.7% smaller below $E_\gamma = 2.1$ GeV with a statistical significance of 3.2σ and 9.7% larger in $2.2 < E_\gamma < 2.9$ GeV with 2.4σ. The LEPS spectrometer covers forward angles and the CLAS spectrometer covers larger angles, therefore it is possible that different processes dominate the reaction.

The spin-density matrix elements are extracted from the decay angular distributions of ϕ mesons, and the dominance of the Pomeron-exchange process ($\sim 80\%$) is confirmed. This is the first measurement of the SDMEs ρ^1 and ρ^2 above 2.37 GeV. They show the moderate energy and t dependences. The SDME $\bar{\rho}^1_{1-1}$, which indicates the ratio of the t-channel natural parity exchange to the unnatural parity exchange, shows the monotonically increasing energy dependence. This observation indicates that the contribution of the Pomeron exchange process increases relative to the other processes.

We used a t-channel Pomeron, π^0, and η exchange model to compare with our results. We

determined the Pomeron strength factor using our cross section results, and confirmed that the $(d\sigma/dt)_{t=t_{\rm min}}$ and SDMEs are consistently described by the Pomeron+π^0 + η model in the E_γ region above 2.37 GeV. As for the t-dependence of the differential cross section, we have to do further parameter adjustments to reproduce the data points, especially tuning of the form factor of the Pomeron-γ-ϕ vertex. In the lower E_γ region, an excess over the model prediction is observed in the energy dependence of $(d\sigma/dt)_{t=t_{\rm min}}$. In the same region, the SDME $\bar{\rho}^1_{1-1}$ is also overestimated. These observations suggest that additional processes or interference effects between Pomeron exchange process and other processes appear near the threshold region. In any case, the process which makes the excess should not bring substantial changes to SDMEs or t-slope factor B.

While this work has revealed that the $\gamma p \to \phi p$ reaction is well explained by the t-channel Pomeron+π^0 + η model above $E_\gamma = 2.37$ GeV, its processes in the lower energy region are still controversial. We tried to explain the excess of $(d\sigma/dt)_{t=t_{\rm min}}$ by introducing a $K^+\Lambda(1520)$ rescattering effect, using an effective Lagrangian approach. By adjusting unknown parameters related to $K^+\Lambda(1520) \to \phi p$ reaction, the excess can be reproduced without modifications of the Pomeron exchange amplitude at low energies. For the further study, a meticulous comparison of the ϕ photoproduction from the proton and the neutron gives valuable information to judge the $K^+\Lambda(1520)$ rescattering contribution.

To pin down the Pomeron behavior at low energies, precise and wide-energy-range measurements of the several reactions such as $\gamma d \to \phi pn$, $\gamma d \to \phi d$, and $\gamma\,^4\mathrm{He} \to \phi\,^4\mathrm{He}$ are essential, in addition to the development of the theoretical approach to associate these reactions with the $\gamma p \to \phi p$ reaction.

ACKNOWLEDGMENTS

I would like to express my deepest gratitude to Prof. Masayuki Niiyama. He has advised and supported me at every stage of this work, with his deep understanding of hadron physics. He is the most rational person I've ever met, and definitely, he has influenced me the most in my life.

I am very grateful to Prof. Tomofumi Nagae, who is the leader of our Experimental Nuclear and Hadronic Physics Laboratory in Kyoto University. He has encouraged me at all times, and gave me a lot of advice to improve this thesis.

I want to thank Prof. Takashi Nakano for fruitful discussions with him. He gave me many outstanding ideas with his brilliant insight for physics.

I would like to offer my special thanks to Mr. Yuki Nozawa. He kindly showed me how to calibrate the LEPS detectors. Also, I enjoyed talking with him many times.

I appreciate Prof. Masaru Yosoi. He has greatly high ability to solve problems, and often helped me when I encountered troubles during the experiment.

I would like to express my appreciation to Prof. Takatsugu Ishikawa. I have learned many experimental techniques and attitudes toward the physics experiment from him.

I thank Prof. Atsushi Hosaka, Dr. Huiyoung Ryu, and Prof. Hideko Nagahiro for meaningful discussions about the amplitude calculations. My thanks go as well to Prof. Kazunori Itakura for his excellent lecture on Regge theory.

I am indebted to all the members of the SPring-8/LEPS collaboration. But for their efforts, this work would not have been accomplished. Especially, Prof. Wen-Chen Chang, who is an expert of the ϕ-meson photoproduction, gave me a lot of useful advice. Also, I am particularly grateful to Prof. Norihito Muramatsu, Prof. Kenneth Hicks, Prof. Hideki Kohri, Mr. Toshihiko Hiraiwa, Prof. Sunyoung Ryu, Mr. Yukiyoshi Kon, Prof. Mizuki Sumihama, Prof. Tomoaki Hotta, Prof. Manabu Miyabe, Prof. Yuji Kato, Prof. Atsushi Tokiyasu, Prof. Takeshi Ohta, Ms. Natsuki Tomida, Mr. Toshikazu Hashimoto, Mr. Hirotomo Hamano, Mr. Shintaro Tanaka, Mr. Hitoshi Katsuragawa, Ms. Yuka Yanai, Mr. Ryo Kobayakawa, and Mr. Ken Watanabe.

I spent an enjoyable time in the Experimental Nuclear and Hadronic Physics Laboratory, and thank all the group members. Thanks to Prof. Takahiro Kawabata, I could work in a comfortable environment. Also, I am lucky to have good and unique colleagues: Mr. Toshikazu Hashimoto, Mr. Shunsuke Kanatsuki, and Mr. Hiroyuki Ekawa.

Last but not least, I would like to thank my father and grandfather who inspired me to aim to become a scientist: Prof. Tadashi Mizutani and Prof. Sumio Sakka.

APPENDIX

A

TEMPLATE FITTING RESULTS FOR YIELD CALCULATION

The template fitting results for the yield calculation are shown in Figs. A.1-A.18. 2007 and 2015 data are separately fitted because the acceptances are different. See section 3.4.1 for details.

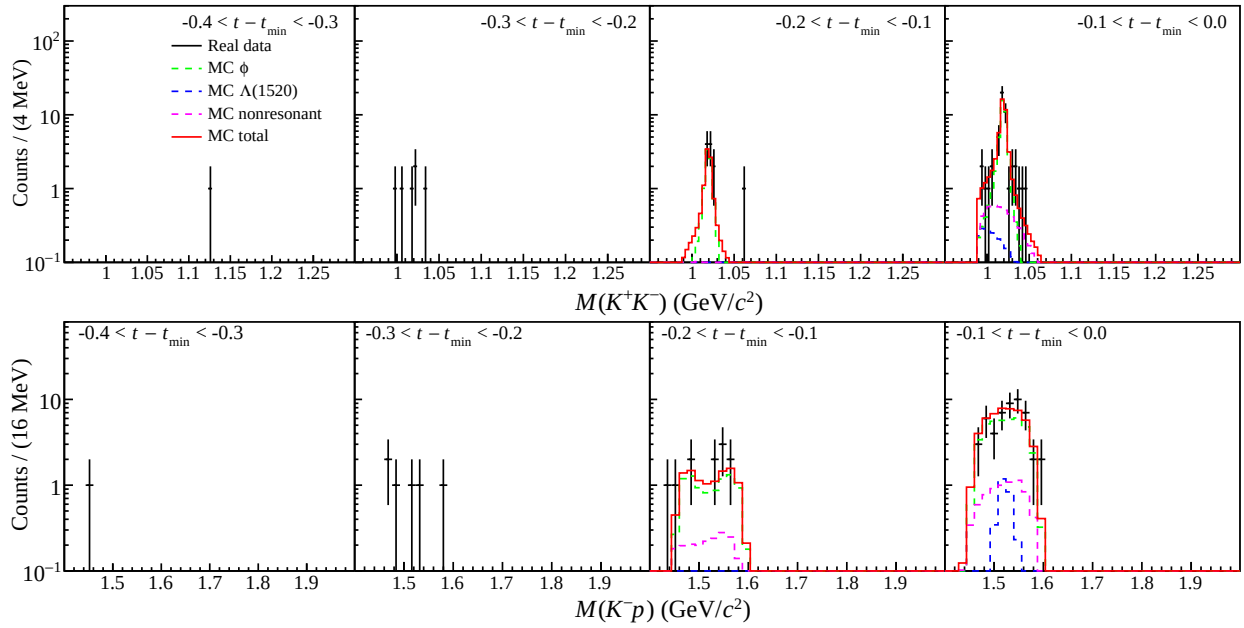

Fig. A.1: $1.67 < E_\gamma < 1.87$ GeV (2015)

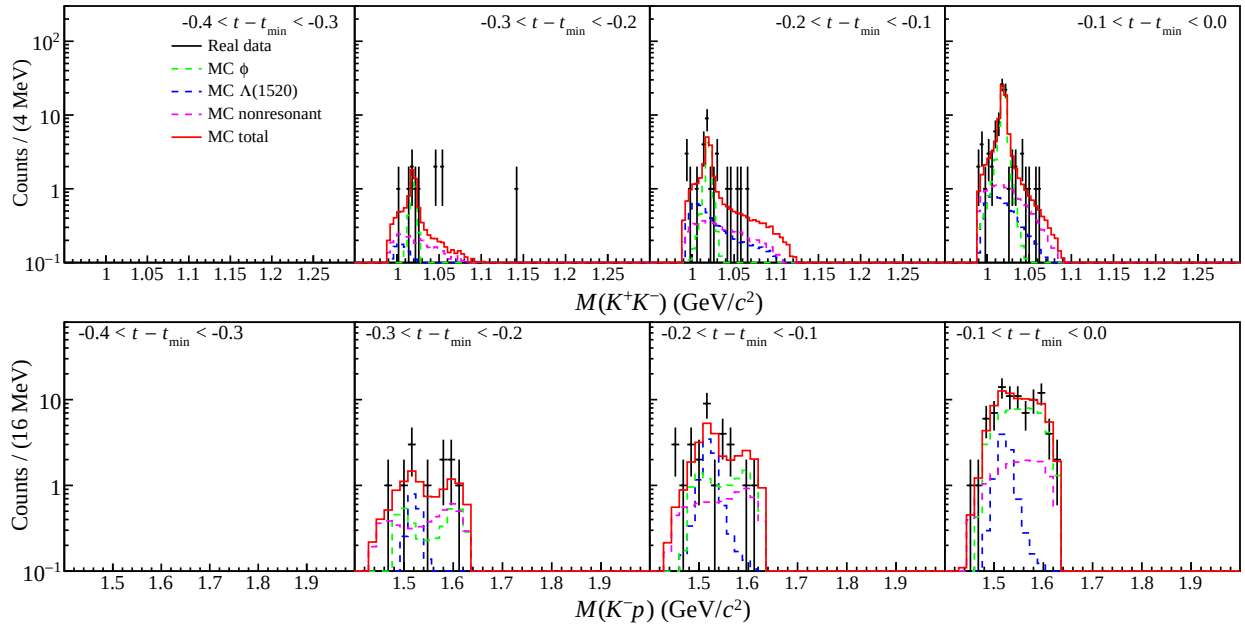

Fig. A.2: $1.87 < E_\gamma < 2.07$ GeV (2015)

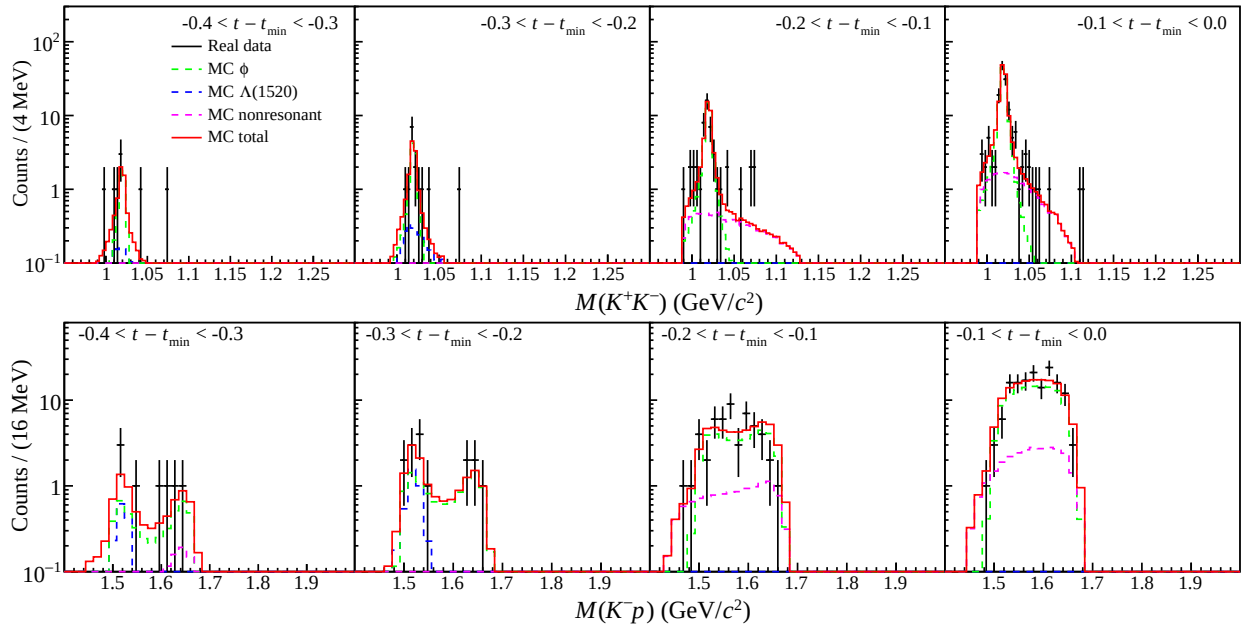

Fig. A.3: $2.07 < E_\gamma < 2.27$ GeV (2015)

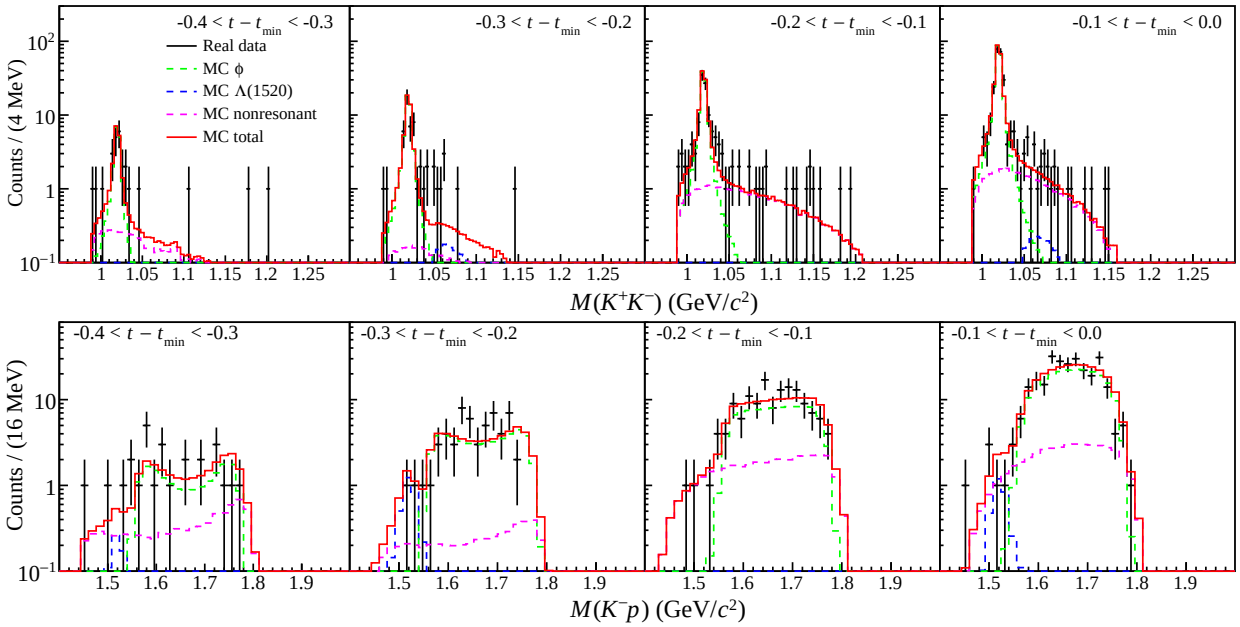

Fig. A.4: $2.27 < E_\gamma < 2.37$ GeV (2015)

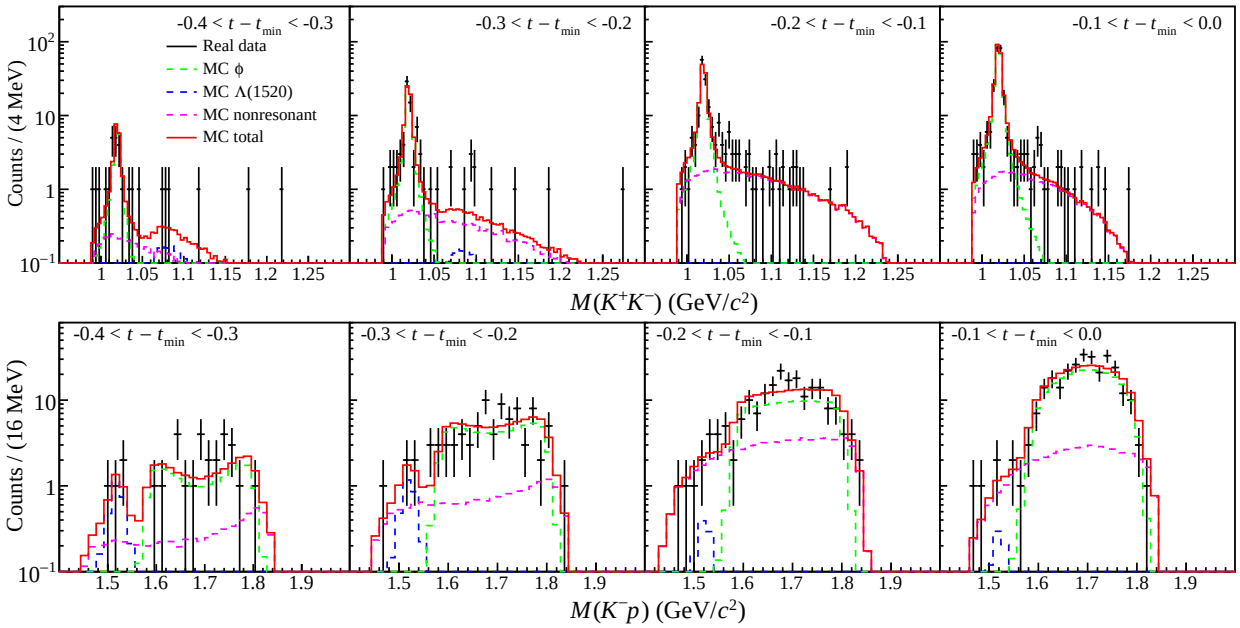

Fig. A.5: $2.37 < E_\gamma < 2.47$ GeV (2015)

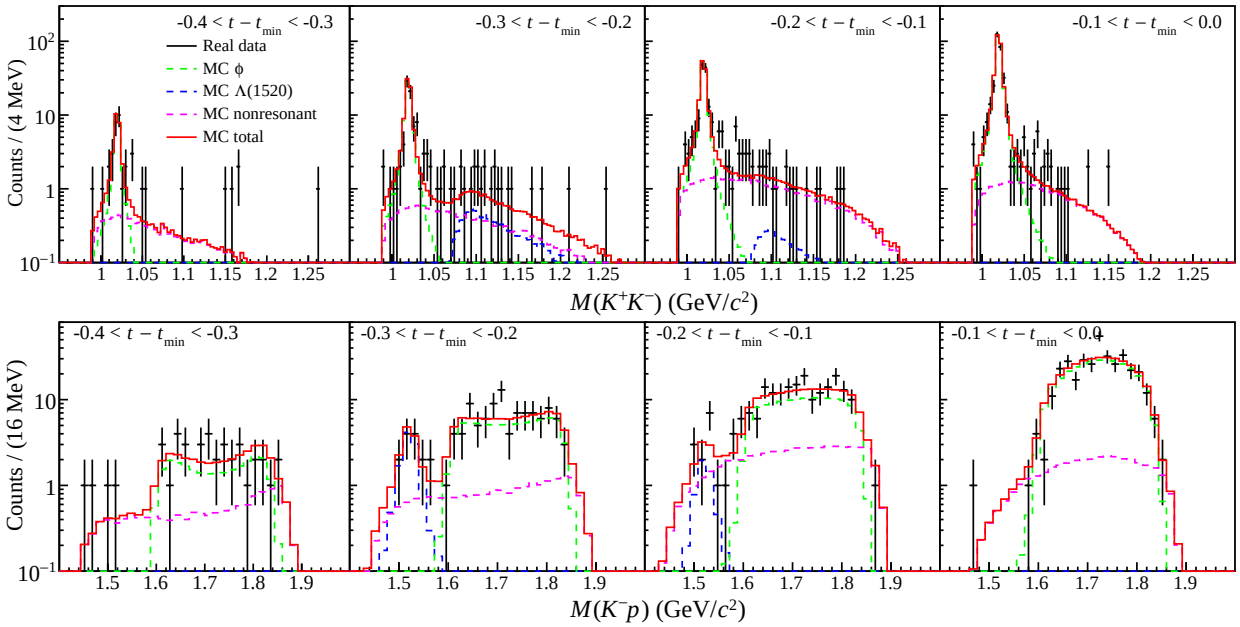

Fig. A.6: $2.47 < E_\gamma < 2.57$ GeV (2015)

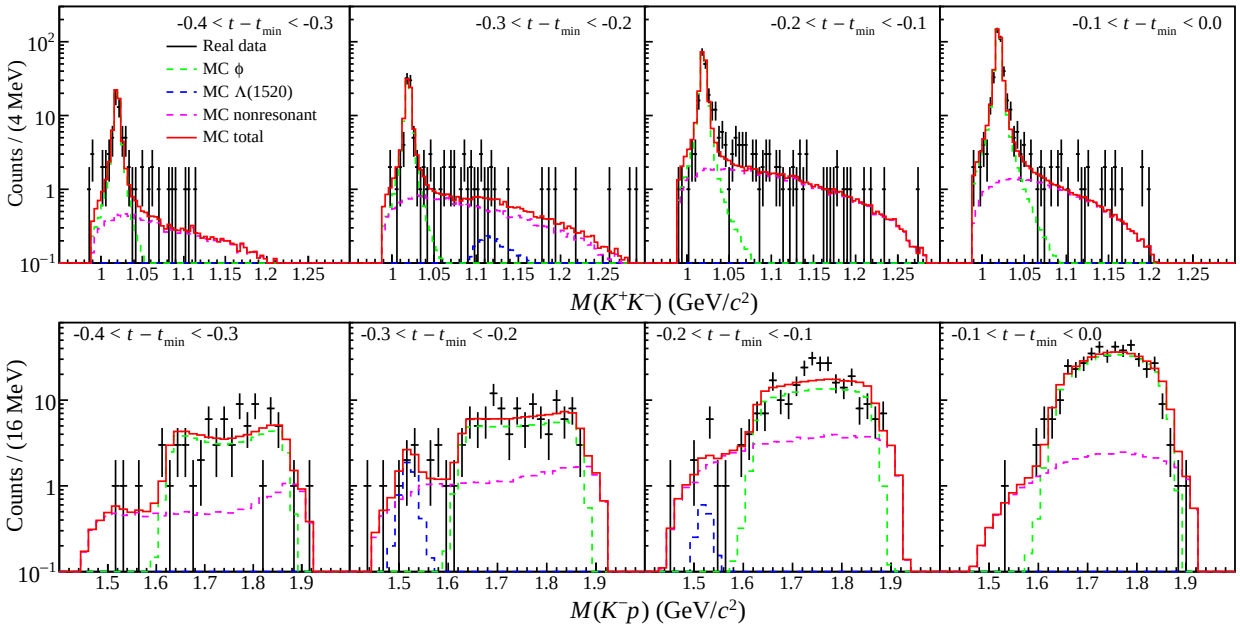

Fig. A.7: $2.57 < E_\gamma < 2.67$ GeV (2015)

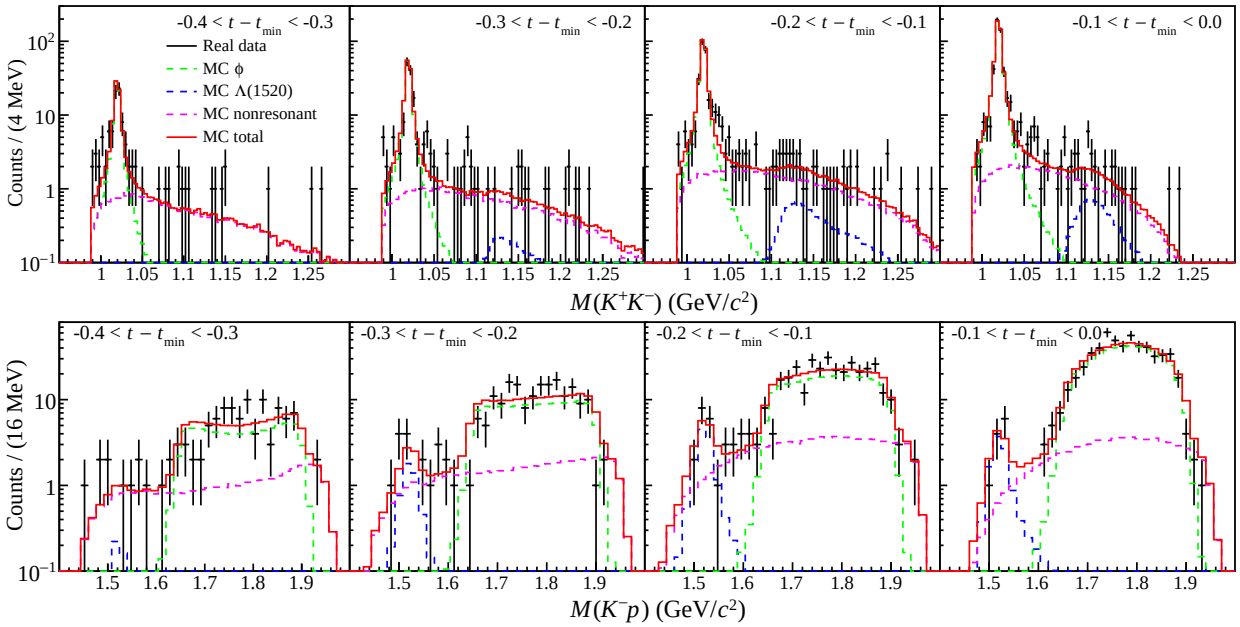

Fig. A.8: $2.67 < E_\gamma < 2.77$ GeV (2015)

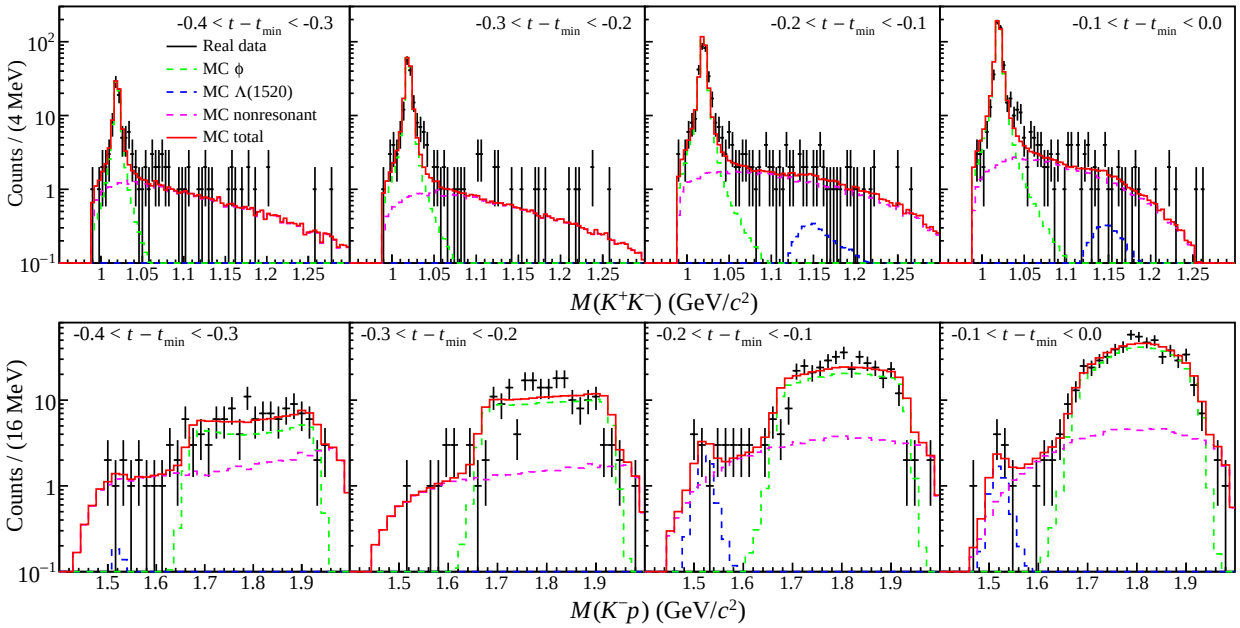

Fig. A.9: $2.77 < E_\gamma < 2.87$ GeV (2015)

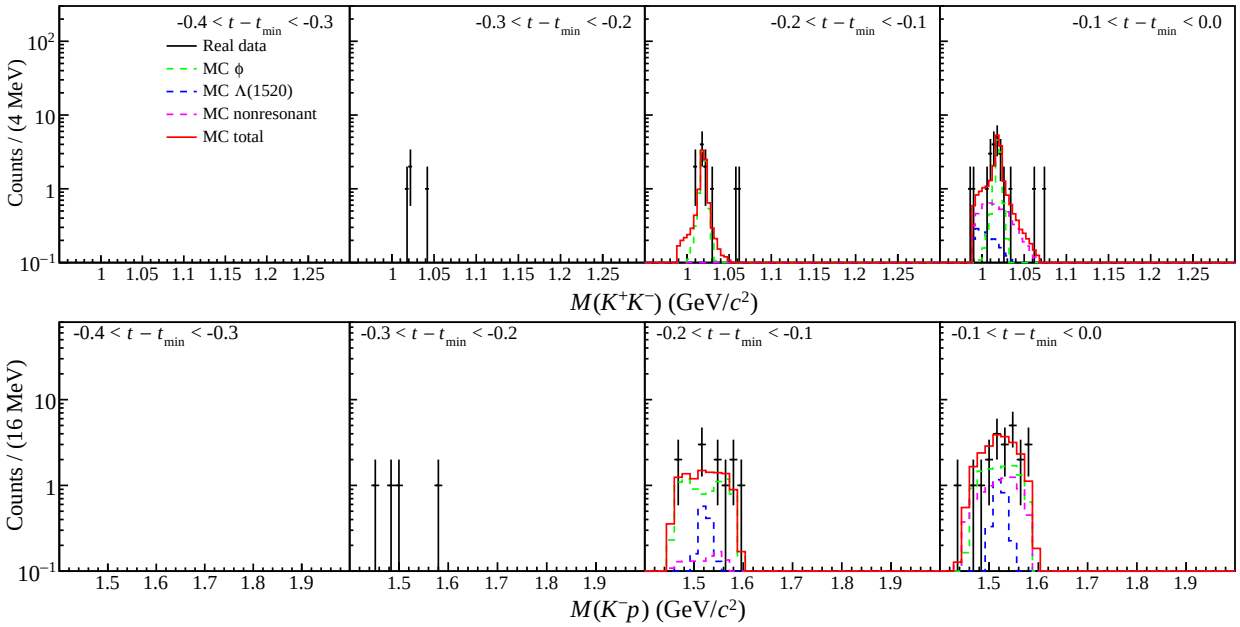

Fig. A.10: $1.67 < E_\gamma < 1.87$ GeV (2007)

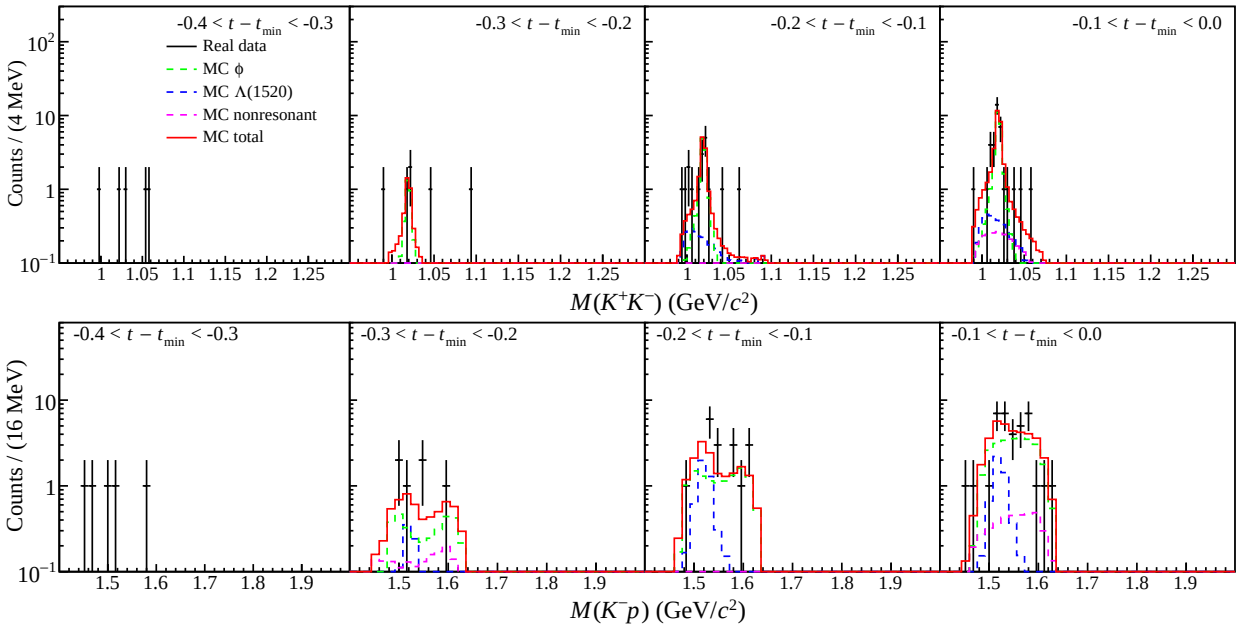

Fig. A.11: $1.87 < E_\gamma < 2.07$ GeV (2007)

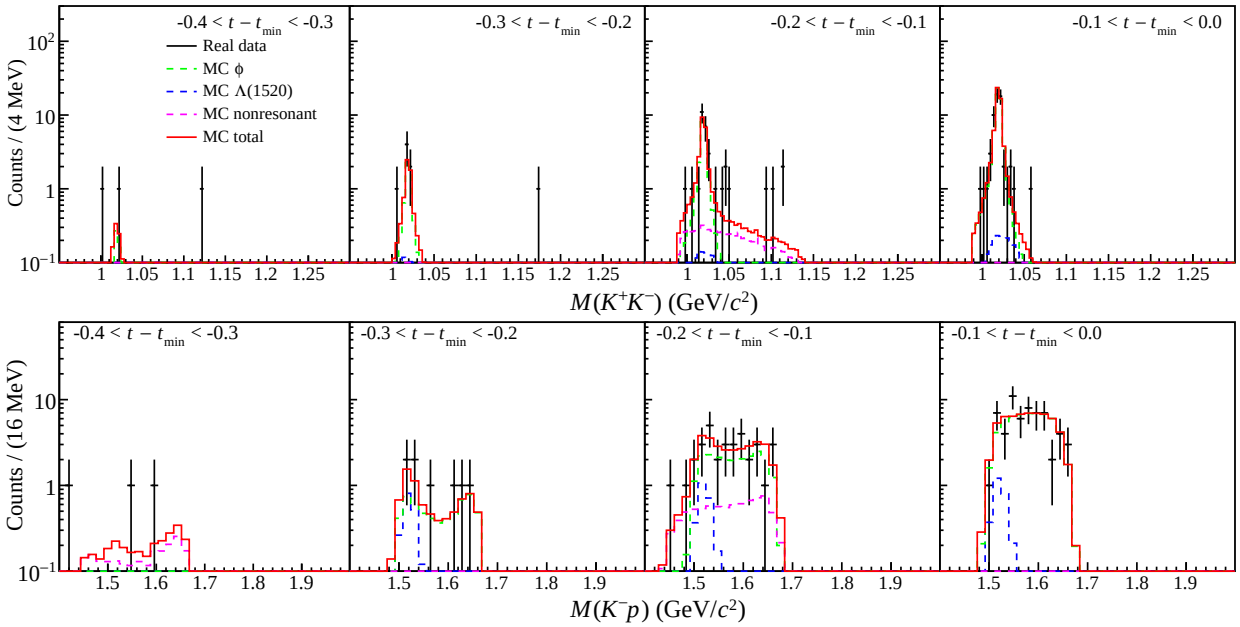

Fig. A.12: $2.07 < E_\gamma < 2.27$ GeV (2007)

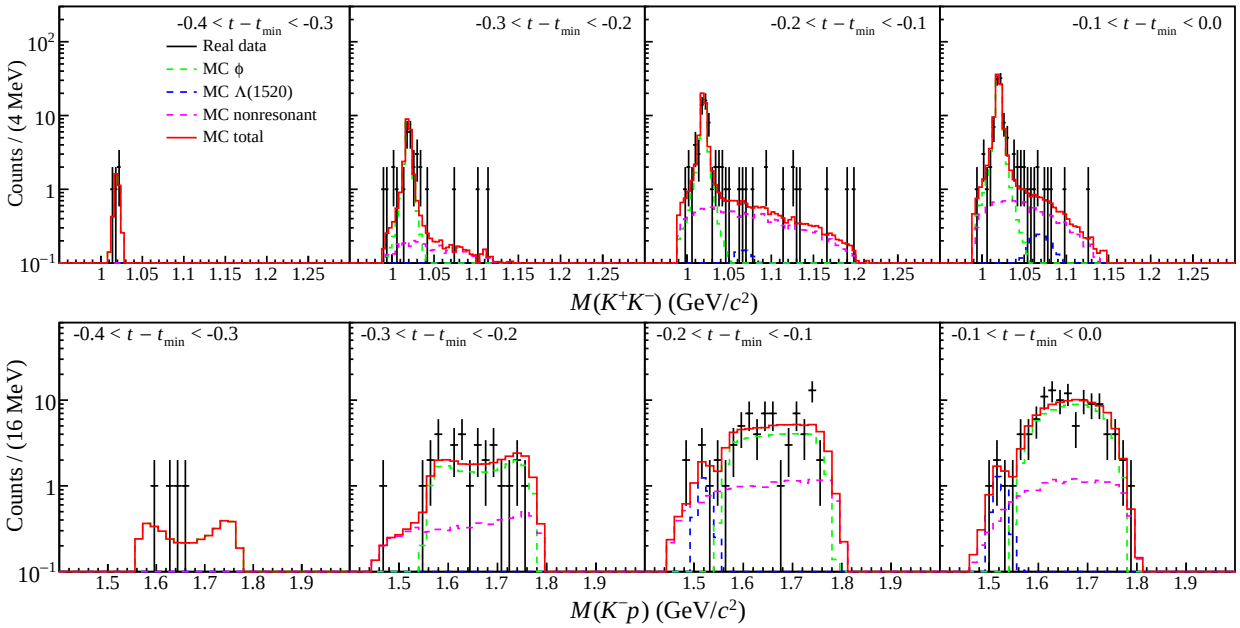

Fig. A.13: $2.27 < E_\gamma < 2.37$ GeV (2007)

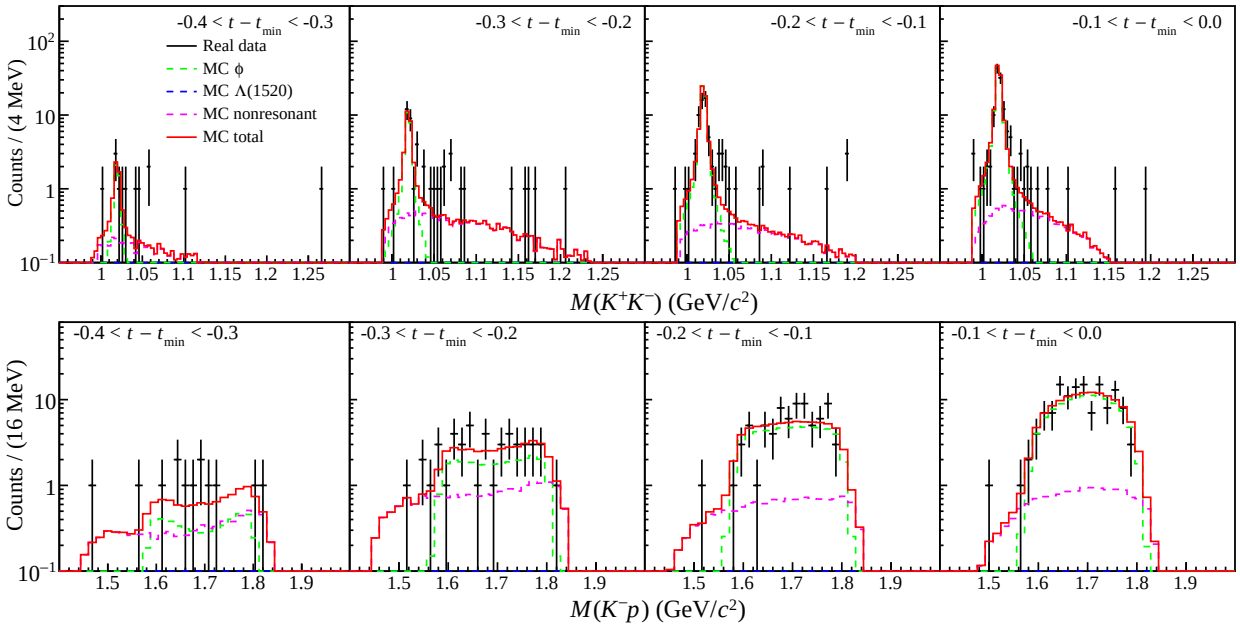

Fig. A.14: $2.37 < E_\gamma < 2.47$ GeV (2007)

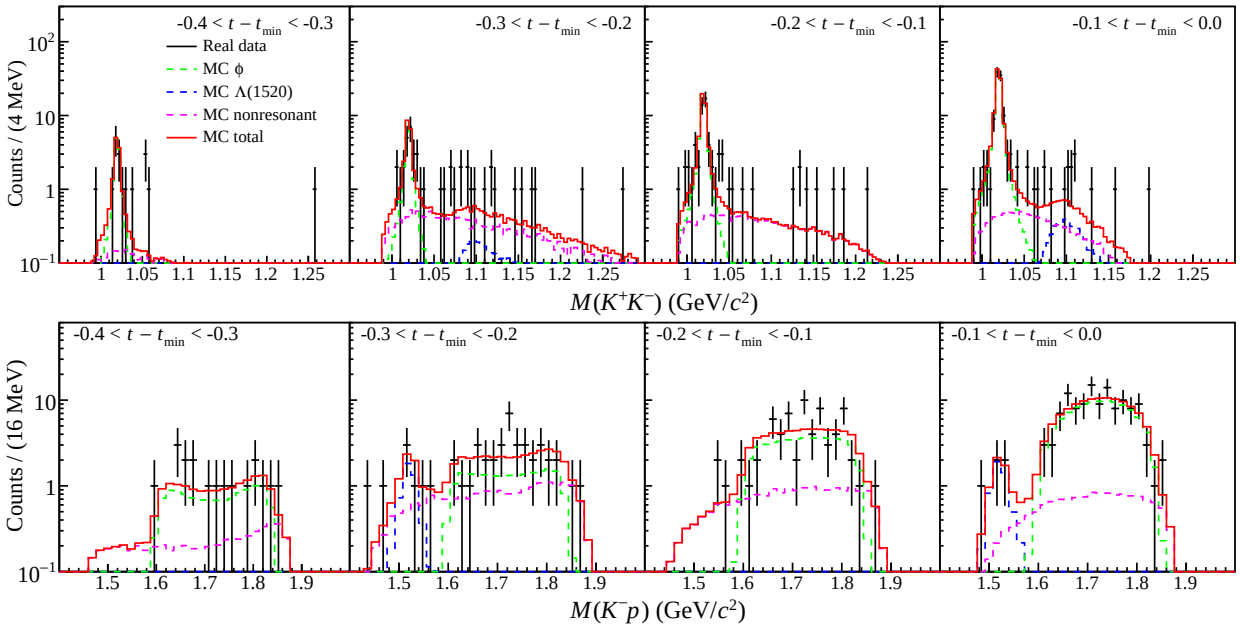

Fig. A.15: $2.47 < E_\gamma < 2.57$ GeV (2007)

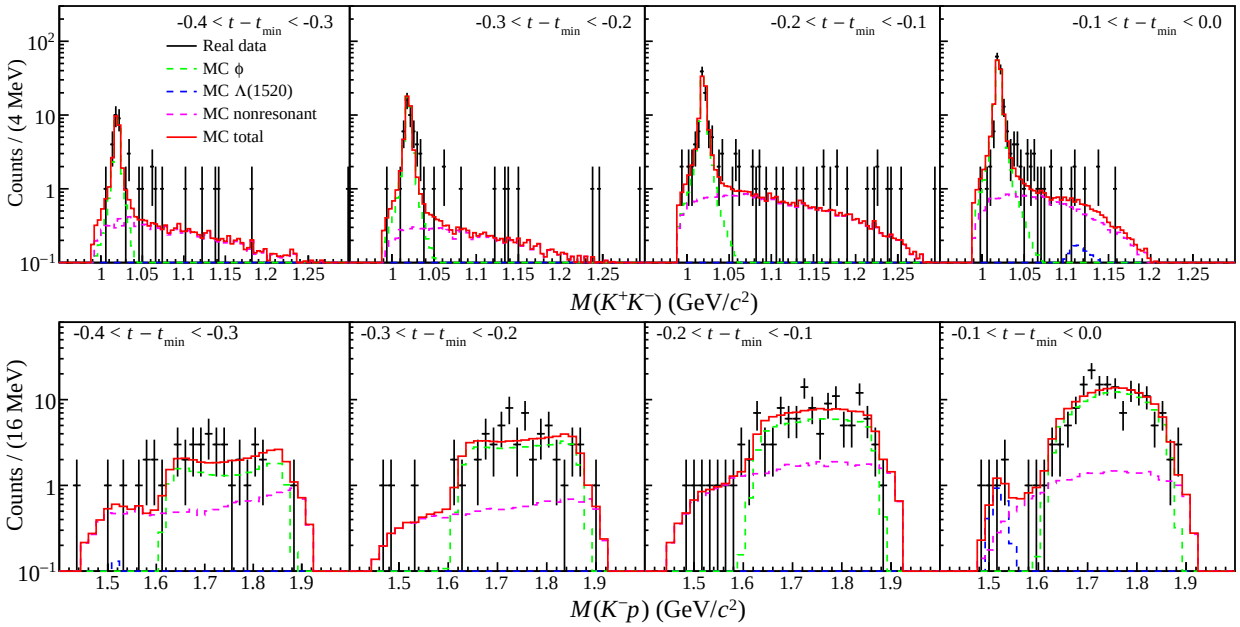

Fig. A.16: $2.57 < E_\gamma < 2.67$ GeV (2007)

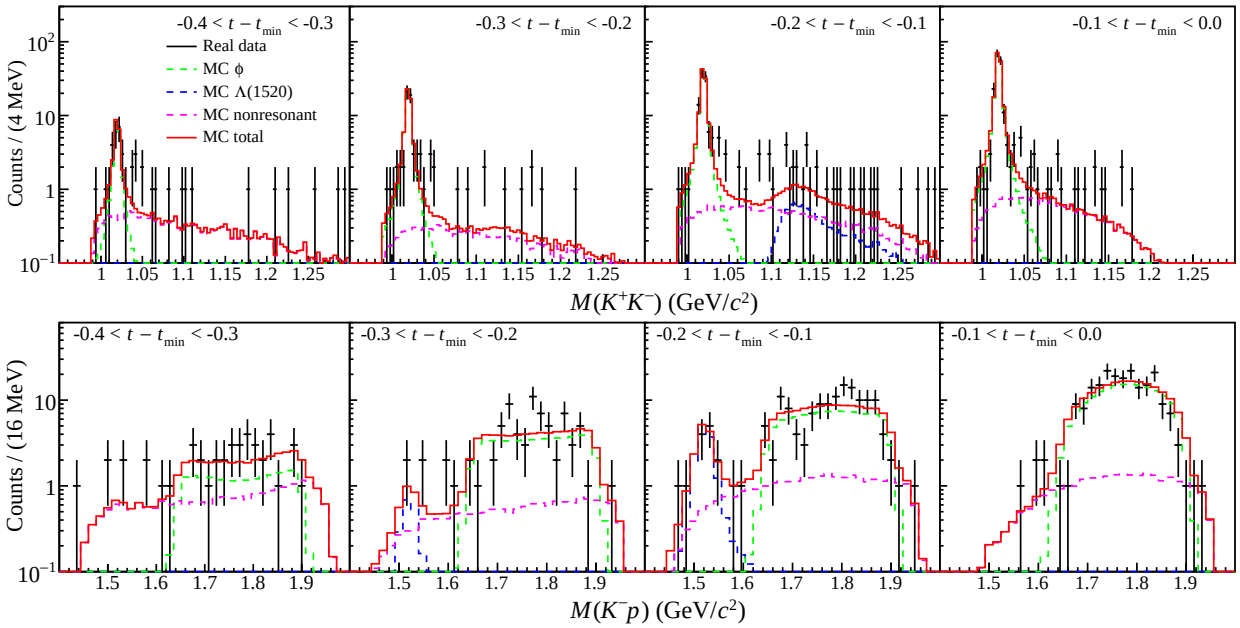

Fig. A.17: $2.67 < E_\gamma < 2.77$ GeV (2007)

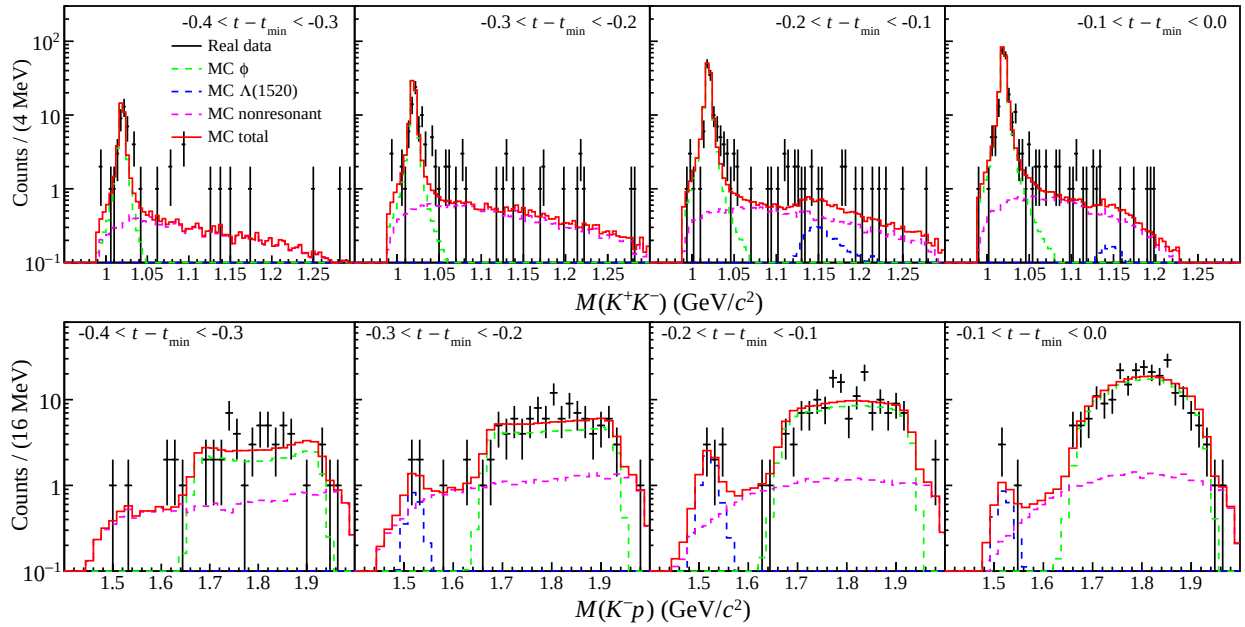

Fig. A.18: $2.77 < E_\gamma < 2.87$ GeV (2007)

[1] T. H. Bauer, R. D. Spital, D. R. Yennie, and F. M. Pipkin, Rev. Mod. Phys., **50**, 261 (1978).

[2] J. J. Sakurai, Annals Phys. **11**, 1 (1960).

[3] S. Donnachie, G. Dosch, P. Landshoff, and O. Nachtmann, *Pomeron Physics and QCD* (Cambridge University Press, 2002).

[4] S. Okubo, Phys. Lett. **5**, 165 (1963).

[5] J. Iizuka, Prog. Theor. Phys. Suppl. **37**, 21 (1966).

[6] P. D. B. Collins, *An introduction to Regge theory and high energy physics* (Cambridge University Press, 1977).

[7] V. Barone and E. Predazzi, *High-Energy Particle Diffraction* (Springer, 2002).

[8] V. N. Gribov, *Strong Interactions of Hadrons at High Energies* (Cambridge University Press, 2008).

[9] A. Bunyatyan, Nucl. Phys. Proc. Suppl. **179**-**180**, 69 (2008).

[10] T. Mibe *et al.* (LEPS Collaboration), Phys. Rev. Lett. **95**, 182001 (2005).

[11] J. Ballam *et al.* (SLAC Collaboration), Phys. Rev. D **7**, 3150 (1973).

[12] H. J. Besch *et al.*, Nucl. Phys. **B70**, 257 (1974).

[13] H. J. Behrend *et al.* (DESY Collaboration), Nucl. Phys. **B144**, 22 (1978).

[14] D. P. Barber *et al.*, Z. Phys. C **12**, 1 (1982).

[15] E. Anciant *et al.* (CLAS Collaboration), Phys. Rev. Lett. **85**, 4682 (2000).

[16] J. Barth *et al.*, Eur. Phys. J. A **17**, 269 (2003).

[17] B. Dey *et al.* (CLAS Collaboration), Phys. Rev. C **89**, 055208 (2014).

[18] A. I. Titov and T.-S. H. Lee, Phys. Rev. C **67**, 065205 (2003).

[19] H. Seraydaryan *et al.* (CLAS Collaboration), Phys. Rev. C **89**, 055206 (2014).

[20] J. R. Forshaw and D. A. Ross, *Quantum Chromodynamics and the Pomeron* (Cambridge University Press, 1997).

[21] S. Mandelstam, Phys. Rev. **112**, 1344 (1958).

[22] L. D. Landau, Nucl. Phys. **13**, 181 (1959).

[23] R. E. Cutkosky, J. Math. Phys. **1**, 429 (1960).

[24] J. Mathews, R. L. Walker, *Mathematical Methods of Physics* (W. A. Benjamin, 1970).

[25] A. Sommerfeld, *Partial Differential Equations in Physics* (Academic Press, 1949).

[26] G. N. Watson, Proc. Roy. Soc. **95**, 83 (1918).

[27] G. F. Chew and S. C. Frautschi, Phys. Rev. Lett. **7**, 394 (1961).

[28] G. F. Chew and S. C. Frautschi, Phys. Rev. Lett. **8**, 41 (1962).

[29] L. L. Foldy and R. F. Peierls, Phys. Rev. **130**, 1585 (1963).

[30] A. Donnachie and P. V. Landshoff, Phys. Lett. B **296**, 227 (1992).

[31] P. V. Landshoff and J. C. Polkinghorne, Nucl. Phys. **B32**, 541 (1971).

[32] C. Augier *et al.* (UA4/2 Collaboration), Phys. Lett. B **315**, 503 (1993).

[33] C. Augier *et al.* (UA4/2 Collaboration), Phys. Lett. B **316**, 448 (1993).

[34] S. M. Troshin and N. E. Tyurin, *Spin Phenomena in Particle Interactions* (World Scientific, 1994).

[35] M. E. Rose, *Elementary Theory of Angular Momentum* (Dover Publications, 1957).

[36] K. Schilling, P. Seyboth, and G. Wolf, Nucl. Phys. **B15**, 397 (1970).

[37] A. I. Titov, T.-S. H. Lee, H. Toki, and O. Streltsova, Phys. Rev. C **60**, 035205 (1999).

[38] W. C. Chang *et al.* (LEPS Collaboration), Phys. Rev. C **82**, 015205 (2010).

[39] A. I. Titov and B. Kämpfer, Phys. Rev. C **76**, 035202 (2007).

[40] W. C. Chang *et al.* (LEPS Collaboration), Phys. Lett. B **658**, 209 (2008).

[41] W. C. Chang *et al.* (LEPS Collaboration), Phys. Lett. B **658**, 209 (2010).

[42] T. Hiraiwa *et al.* (LEPS Collaboration), arXiv:1711.01095v2 [nucl-ex].

[43] A. Kiswandhi, J.-J. Xie, and S. N. Yang, Phys. Lett. B **691**, 214 (2010).

[44] A. Kiswandhi and S. N. Yang, Phys. Rev. C **86**, 015203 (2012).

[45] S. Y. Ryu *et al.* (LEPS Collaboration), Phys. Rev. Lett. **116**, 232001 (2016).

[46] S. Ozaki, A. Hosaka, H. Nagahiro, and O. Sholten, Phys. Rev. C **80**, 035201 (2009).

[47] H.-Y. Ryu, A. I. Titov, A. Hosaka, and H.-C. Kim, Prog. Theor. Exp. Phys. **2014**, 023D03 (2014).

[48] T. Nakano and H. Toki, eds., *Proceedings of the International Workshop on Exciting Physics with New Accelerators Facilities* (World Scientific, 1997).

[49] L. S. Kisslinger and W.-H. Ma, Phys. Lett. B **485**, 367 (2000).

[50] H. Kohri *et al.* (LEPS Collaboration), Phys. Rev. Lett. **104**, 172001 (2010).

[51] S.-I. Nam, A. Hosaka, and H.-C. Kim, Phys. Rev. D. **71**, 114012 (2005).

[52] J. Beringer *et al.* (Particle Data Group), Phys. Rev. D. **86**, 010001 (2012).

[53] H. Kamitsubo, Nucl. Instrum. Methods Phys. Res. A **303**, 421 (1991).

[54] T. Nakano *et al.*, Nucl. Phys. **A684**, 71 (2001).

[55] S. H. Hwang *et al.*, Phys. Rev. Lett. **108**, 092001 (2012).

[56] N. Muramatsu *et al.*, Nucl. Instrum. Methods Phys. Res. A **737**, 184 (2014).

[57] A. D'Angelo *et al.*, Nucl. Instrum. Methods Phys. Res. A **455**, 1 (2000).

[58] P. A. Franken, A. E. Hill, C. W. Peters, and G. Weinreich, Phys. Rev. Lett. **7**, 118 (1961).

[59] D. A. Kleinman, Phys. Rev. **128**, 1761 (1962).

[60] T. Nakano *et al.* (LEPS Collaboration), Phys. Rev. C **79**, 025210 (2009).

[61] O. Toker, S. Masciocchi, E. Nygård, A. Rudge, and P. Weilhammer, Nucl. Instrum. Methods Phys. Res. A **340**, 572 (1994).

[62] Y. Sugaya and M. Nomachi, Nucl. Instrum. Methods Phys. Res. A **437**, 68 (1999).

[63] Y. Sugaya *et al.*, IEEE Trans. Nucl. Sci. **48**, 1282 (2001).

[64] R. Frühwirth, Nucl. Instrum. Methods Phys. Res. A **262**, 444 (1987).

[65] R. Brun *et al.* (Application Software Group), CERN Program Library Long Writeup W5013.

[66] M. Sumihama *et al.* (LEPS Collaboration), Phys. Rev. C **73**, 035214 (2006).

[67] A. Donnachie and P. V. Landshoff, Nucl. Phys. **B244**, 322 (1984).

[68] A. Donnachie and P. V. Landshoff, Nucl. Phys. **B267**, 690 (1986).

[69] A. Donnachie and P. V. Landshoff, Phys. Lett. B **185**, 403 (1987).

[70] A. I. Titov and T.-S. H. Lee, Phys. Rev. C **66**, 015204 (2002).

[71] Yongseok Oh and T.-S. H. Lee, Phys. Rev. C **69**, 025201 (2004).

[72] R. Koch and E. Pietarinen, Nucl. Phys. **A336**, 331 (1980).

[73] K. Nakayama, Yongseok Oh, and H. Haberzettl, Phys. Rev. C **74**, 035205 (2006).

[74] Yongseok Oh, Che Ming Ko, and K. Nakayama, Phys. Rev. C **77**, 045204 (2008).

[75] Jun He, Phys. Rev. C **89**, 055204 (2014).

[76] Xiao-Yun Wang, Jun He, and Helmut Haberzettl, Phys. Rev. C **93**, 045204 (2016).

[77] K. Nakayama and H. Haberzettl, Phys. Rev. C **69**, 065212 (2004).

[78] Sang-Ho Kim, Seung-il Nam, Yongseok Oh, and Hyun-Chul Kim, Phys. Rev. D **84**, 114023 (2011).

[79] Sang-Ho Kim, Seung-il Nam, Atsushi Hosaka, and Hyun-Chul Kim, Phys. Rev. D **88**, 054012 (2013).

[80] Seung-il Nam, Ki-Seok Choi, Atsushi Hosaka, and Hyun-Chul Kim, Phys. Rev. D **75**, 014027 (2007).

[81] Ulf-G. Meißner, V. Mull, J. Speth, and J. W. Van Orden, Phys. Lett. B **408**, 381 (1997).

[82] K. Moriya *et al.* (CLAS Collaboration), Phys. Rev. C **88**, 045201 (2013).

[83] F. W. Wieland *et al.* (SAPHIR Collaboration), Eur. Phys. J. A **47**, 47 (2011).

[84] D. P. Barber *et al.* (LAMP2 Group), Z. Phys. C **7**, 17 (1980).

[85] N. Muramatsu *et al.* (LEPS Collaboration), Phys. Rev. Lett. **103**, 012001 (2009).

[86] R. B. Wiringa, Phys. Rev. C **43**, 1585 (1981).